Multijets
in Photoproduction
at HERA

Dissertation

zur Erlangung des Doktorgrades
des Fachbereichs Physik
der Universität Hamburg

vorgelegt von
KALOYAN KRASTEV
aus Sliven

Hamburg
2008

Abstract

In the analysis jets in photoproduction are studied with data collected by the **H1** detector in 2006. Events with at least two jets with transverse energy greater than 9 GeV and pseudorapidity in the range of -0.5 to 1.5 in the laboratory frame are selected for the dijet sample. For the trijet and fourjet scenarios, one and two additional jets with transverse energy greater than 6 GeV and pseudorapidity in the range of -0.5 to 2.4 are required.

The aim of the analysis is to study the dynamics of multijet events (events with more than two jets). In the perturbative picture the jet rate increases due to additional parton emissions. The jet rate can also be affected by multiple parton interactions when several pairs of partons within the incoming particles interact.

Differential cross sections as a function of various variables for the dijet, trijet and fourjet scenario are measured. In addition, the applicability of two currently established multiple interaction models is tested. The results show that current models are not correctly describing the properties of multijet events in the analyzed phase space.

Kurzfassung

In dieser Analyse werden Jets in Photoproduktion untersucht, die mit dem **H1** Detektor im Jahr 2006 gemessen wurden. Dabei werden Ereignisse mit mindestens zwei Jets selektiert, deren Transversalenergien mehr als 9 GeV betragen und deren Pseudorapiditäten im Laborsystem zwischen -0.5 und 1.5 liegen. Für die Drei- und Vierjet-Szenarien werden ein beziehungsweise zwei weitere Jets verlangt, deren Transversalenergien mehr als 6 GeV betragen und deren Pseudorapiditäten zwischen -0.5 und 2.4 liegen.

Das Ziel der Analyse ist die Untersuchung der Dynamik von Multijetereignissen, d. h. Ereignissen mit mehr als zwei Jets. Im störungstheoretischen Ansatz sind zusätzliche Partonemissionen für den Anstieg der Jetrate verantwortlich. Desweiteren können auch Mehrfachwechselwirkungen die Anzahl der produzierten Jets beeinflussen, wobei mehr als ein Parton-Paar wechselwirkt.

Es wurden differentielle Wirkungsquerschnitte als Funktionen verschiedener Variablen für die Zwei-, Drei- und Vierjet-Szenarien gemessen. Mithilfe dieser Daten wurden zwei etablierte Modelle für Mehrfachwechselwirkungen geprüft. Die Resultate zeigen, dass die bisherigen Modelle nicht in der Lage sind, die Eigenschaften von Mehrfachjetereignissen im untersuchten Phasenraum zu beschreiben.

Резюме

Дисертацията е посветена на анализа на адронни струи в режим на фотопродукция. Използвани са данните от детектора **H1**, записани през 2006-та година. Изследвани са двуструйни събития с напречна енергия на струите по-голяма от 9 ГеВ и псевдобързина в обхвата от -0.5 до 1.5, измерени в лабораторна отправна система. За три- и четириструйни събития се изискват една или две допълнителни струи с напречна енергия по-голяма от 6 ГеВ и псевдобързина между -0.5 и 2.4.

Целта на анализа е да се изследва динамиката на мултиструйните събития (събития с повече от две струи). От гледна точка на теорията на пертурбациите за силните взаимодействия, броят на струите нараства посредством допълнителни емисии на партони. Този брой би могъл да бъде засегнат и от т.нар. мултипартонни взаимодействия, при които няколко двойки партони от налитащите частици взаимодействат помежду си.

Измерени са диференциалните сечения за дву-, три- и четириструйни събития като функция на различни наблюдаеми. Резултатите са сравнени с предсказанията на два утвърдени модела, включващи мултипартонни взаимодействия. Сравнението показва, че моделите не описват задоволително характера на мултиструйните събития в наличното фазово пространство.

"*If you say that everything, Chaos, darkness, anathema, can be reduced to mathematical formula, that it is possible to anticipate all things and keep them under the sway of reason by means of arithmetical calculation, then man will go insane on purpose so as to have no judgment and behave as he likes. Believe this because it appears that man's whole business is to prove to himself that he is a man and not a cog-wheel.*" F. M. Dostoevsky

Contents

List of Figures

List of Tables

Preface

The fundamental structure of matter is studied at HERA in high energy hadron-lepton collisions. According to our present understanding, all particle interactions are explained by exchange of virtual bosons between the incident particles. In *Deep Inelastic Scattering* (DIS) process the virtuality, Q^2, of the exchange boson is large. Hence, the internal structure of the proton is resolved. In photoproduction regime the incoming leptons scatter at small angles and can be considered as a source of quasi-real photons.

In this work an analysis of jet photoproduction is presented. Cross sections of various dijet, trijet and fourjet observables are determined. The aim of the analysis is to study multijet events (events with more than two jets). Measured data are compared to several Monte Carlo models. In perturbative picture the jet rate increases due to additional parton emissions. In addition, jet rate is affected by *multiple interactions* (MI), when interactions between more than one pair of partons within the incoming particles occur. Multiple interactions are expected to be important in resolved photoproduction when the exchange photon fluctuates to hadronic matter with same quantum numbers.

The measured cross sections are corrected for the trigger efficiency and detector effects and compared with the Monte Carlo event generators PYTHIA, HERWIG and CASCADE. PYTHIA and HERWIG are based on the DGLAP evolution equations in which the emitted partons are ordered in transverse momenta. Both models generate multiple parton-parton interactions by adding additional hard interactions to events. CASCADE is based on the CCFM evolution equation for which the ordering of partons in their transverse momenta is broken. Although there is no explicit implementation of MI in CASCADE, it is interesting to investigate if gluons, radiated according to the CCFM evolution scheme, could result in multijet events with similar configuration as MI events.

Chapter 1 marks off theory concepts, important for the performed analysis. The **H1** detector and trigger components are described in Chapter 2 and Chapter 3. Monte Carlo event generators are discussed in Chapter 4. The data selection proce-

dure can be found in Chapter 5. It contains also the trigger studies as they define the available phase space of the measurement. Chapter 6 describes the data correction procedure and the classification of the experimental uncertainties. Here the corrected data are compared to the model predictions. Conclusions are drawn in Chapter 7.

Chapter 1

Theoretical Overview

The Standard Model[1] is a field theory that explains most of the known phenomena in elementary particle physics. It describes strong, electromagnetic and weak interactions. Gravitational forces are not included in the Standard Model but their impact on fundamental particle processes at accessible energies is negligible. According to the Standard Model, there is a strong, called "color" charge and electroweak charge. The matter fields are the quarks with both color and electroweak charge and the leptons (the *electron* (e), the *muon* (μ), the *tau lepton* (τ) plus three associated neutrinos) with no color but only electroweak charge. As shown in Figure 1.1, the matter fermions come in three generations with identical quantum numbers but different mass. Each family contains a weakly charged doublet of quarks and a colorless weakly charged doublet with a neutrino and an electrically charged lepton. There is no explanation for this triple repetition of fermion families. The force carriers, of spin 1, are the *photon* (γ), the massive gauge bosons W^+, W^- and Z^0 and the *gluon* (g) that mediates the strong interaction.

$$\begin{pmatrix} u \\ d \end{pmatrix} \begin{pmatrix} c \\ s \end{pmatrix} \begin{pmatrix} t \\ b \end{pmatrix}$$
$$\begin{pmatrix} \nu_e \\ e \end{pmatrix} \begin{pmatrix} \nu_\mu \\ \mu \end{pmatrix} \begin{pmatrix} \nu_\tau \\ \tau \end{pmatrix}$$

Figure 1.1: *Three fermion generations, each with weakly charged quark doublet, in three colors and a weakly charged doublet of neutrino and charged lepton.*
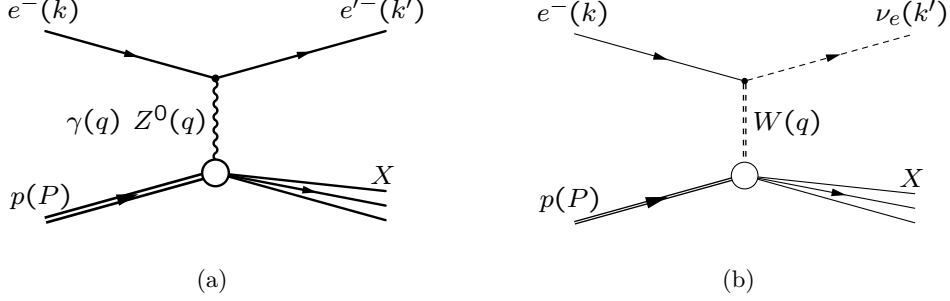
Figure 1.2: *Neutral (a) and charged (b) current DIS process at HERA. The four-momenta of the particles are shown in parentheses.*

1.1 Electron-Proton Scattering

A diagram of the electron-proton scattering is shown in Figure 1.2. The electron e^- interacts with the proton via an exchange of a virtual boson. In the *neutral current* the virtual boson is a photon or a neutral Z^0-boson while in the *charged current* it is a charged weak boson ($W^{\pm}$). P, k and q denote the four-momentum vectors of the proton, the incoming electron and the exchanged virtual boson, respectively. k' is the four-momentum of the outgoing particle (electron in the neutral current and neutrino in the charged current). The total center-of-mass energy is

$$s = (k + P)^2. \tag{1.1}$$

If the masses of the incoming particles are neglected,

$$s = 4E_e E_p, \tag{1.2}$$

where E_e and E_p are the energies of the electron and proton beam, respectively. The invariant mass of the outgoing system denoted by X in Figure 1.2 is:

$$W^2 = (P + q)^2. \tag{1.3}$$

Since the exchanged photon is virtual, the four momentum q does not satisfy $q^2 = 0$. The invariant mass W of the outgoing system can be written as:

$$W^2 = m_p^2 + 2P \cdot q + q^2, \tag{1.4}$$

where m_p is the proton mass. The *negative squared momentum transfer*,

$$Q^2 \equiv -q^2 = -(k - k')^2 \tag{1.5}$$

is the Lorentz invariant mass squared of the exchanged boson [1]. The wavelength of the photon is $\lambda = 1/Q$. For $\lambda \gg R_p$, where R_p is the radius of the proton,

---

[1] Q^2 is often referred to as the *virtuality* of the exchanged boson.
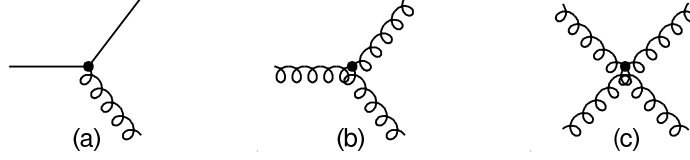
Figure 1.3: *Fundamental vertices of QCD, gluon-quark-antiquark vertex (a), 3-gluon (b) and 4-gluon (c) vertex.*

the exchanged photon interacts with the proton as a whole and the scattering is *elastic*. The proton remains intact and $W = m_p$. The scattering is *inelastic* when $W^2 \gg m_p^2$. If $\lambda \ll R_p$, the photon may probe deep within the proton. The process is called *Deep Inelastic Scattering* (DIS) when $Q^2 \gg 0$. The following relations are valid if the masses of the incoming particles are neglected:

$$x = \frac{Q^2}{2P \cdot q}, \tag{1.6}$$

where x is the *Bjorken scaling variable*[2]. The *fractional energy loss of the electron*,

$$y = \frac{P \cdot q}{P \cdot k}, \tag{1.7}$$

is the fraction of the electron momentum carried by the exchanged boson in the proton rest frame. The following relations are obtained from the previous equations.

$$Q^2 = xys, \tag{1.8}$$

$$W^2 = ys - Q^2. \tag{1.9}$$

At fixed total center-of-mass energy only two of the variables Q^2, x, y and W are independent. The maximum $Q^2 = s$ is obtained for $x = y = 1$.

1.2 Quantum Chromodynamics

Quantum Chromodynamics (QCD) is the theory of the strong interaction between the quarks and the gluons. The physics vertices of QCD include the gluon-quark-antiquark vertex, analogous to the QED photon-fermion-antifermion coupling, but also the 3-gluon and 4-gluon vertices which have no analog in QED. The photon couples to all electrically charged particles but itself is electrically neutral. The colored gluon may self couple. Instead of one entity, *charge*, there are three different *colors*. In Figure 1.3 the fundamental vertices of QCD are displayed. The solid line represents quarks and the helix is for gluons.

The two main characteristics of QCD are confinement and asymptotic freedom. *Asymptotic freedom* means that the *strong coupling constant* (α_s) decreases for
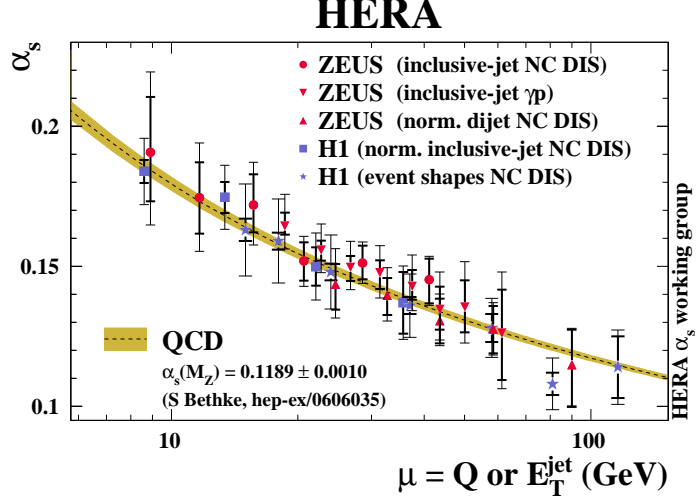
Figure 1.4: *The running of the strong coupling constant α_s as measured at HERA.*

increasing Q^2 and vanishes asymptotically. The strong interaction becomes weak in processes with large Q^2 and the effective coupling decreases very slowly with the inverse logarithm of Q^2:

$$\alpha_s(Q^2) \sim \frac{1}{\ln(Q^2/\Lambda_{QCD}^2)}, \tag{1.10}$$

where Λ_{QCD} is a constant with a dimension of energy and a value of order of few hundred MeV. The running of α_s has been verified experimentally. The results from measurements at HERA are shown in Figure 1.4 [3]. The strong interaction strength becomes large at small transferred momenta of order $Q \leq \Lambda_{QCD}$. The observed hadrons are tightly bound composite states of quarks, with compensating color charges so that they are overall neutral in color. At long distance the interaction potential between color charges increases linearly with the distance. This property of QCD is called *confinement*. It explains the experimental absence of free quarks.

In the *Quark-Parton Model* (QPM) the inelastic scattering of the electron off the proton is described as elastic scattering of the electron off a free point-like object within the proton. The QPM process is shown in Figure 1.5 (a). It does not include any strong interaction (interactions with the rest of the proton are neglected). In this frame the Bjorken scaling variable x represents the fraction of the 4-momentum of the proton, carried by the struck quark, q. However, at first order in α_s, the DIS process receives contributions from the *Boson-gluon fusion* (BGF) and the *QCD-Compton* (QCDC) processes which are shown in Figure 1.5 (b) and (c) respectively. At second order of α_s, more real and virtual processes contribute to the cross section
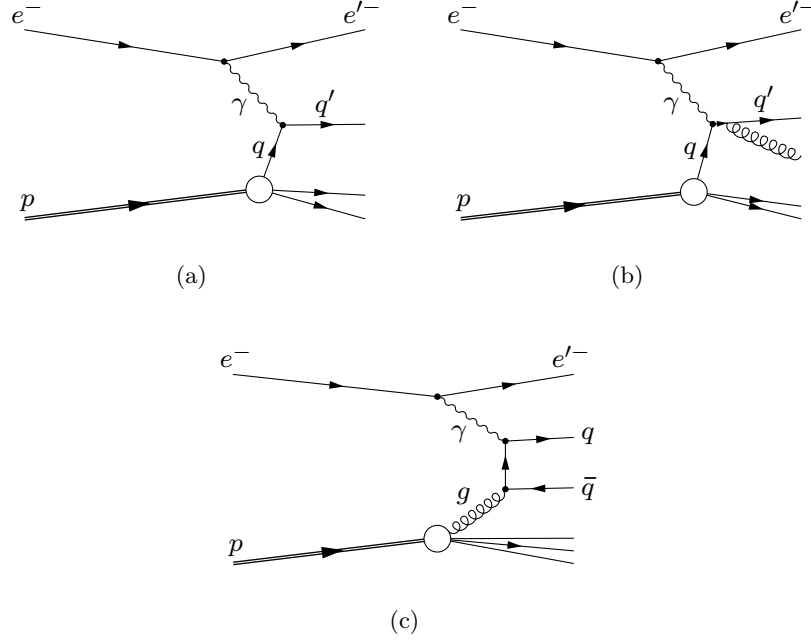
Figure 1.5: *The DIS process at HERA: a) in the QPM approximation, b) the BGF(gluon emission) process and (c) QCDC.*

and this is valid for all higher orders of α_s.

Calculations of production cross sections are performed according to the perturbation theory. In *perturbative* (pQCD), α_s is used as an expansion parameter. At large scales ($Q \gg \Lambda_{QCD}$) or ($\alpha_s \ll 1$) the perturbation series converge fast and the calculations could be truncated to some fixed order of α_s without loss of accuracy. The large value of α_s at low scales marks the **soft** region where pQCD is not applicable. The scattering process factorizes when it can be written as a product of the soft and perturbatively calculable part of the process. The soft elements within the proton structure are parametrized and extracted from data measurements in terms of *Parton Density Functions* (**PDFs**). The universal PDFs for each flavor, including the gluon, are defined as the probability $f_i(x, \mu^2)$ to find a parton of flavor i, carrying a fraction x of the proton momentum at a scale μ^2. They are called universal because they do not depend on the type of collision or on the diagram which is considered. If the process is factorizable, the cross section is calculated as a convolution of the perturbatively calculable hard scattering partonic cross section, $\hat{\sigma}$, and the PDFs, according to the factorization formula:

$$\sigma = \sum_i f_i(x, \mu_F^2) \otimes \hat{\sigma}(x, \mu_F^2), \tag{1.11}$$

where μ_F is the factorization scale. Perturbative QCD is not able to give predictions to the values of PDFs. However, it can be used to determine the PDFs
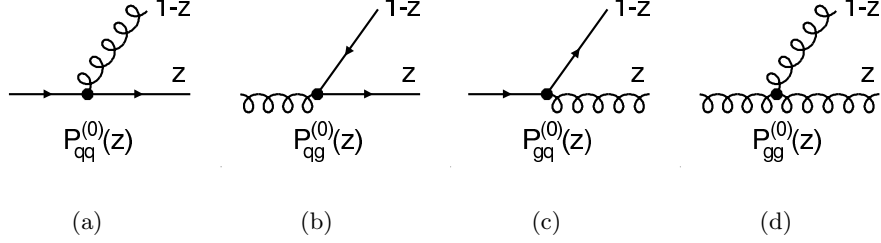
Figure 1.6: *The leading order α_s splitting functions $P_{ij}(z)$ give the probability that parton j radiates parton i carrying momentum fraction z.*

dependence on the energy scale. The evolution of the parton densities is given by the DGLAP equations[4, 5, 6]:

$$\frac{\mathrm{d}f_i(x,\mu^2)}{\mathrm{d}(\ln\mu^2)} = \frac{\alpha_s}{2\pi}\int_x^1 \frac{\mathrm{d}z}{z}\sum_j f_j(z,\mu^2)P_{ij}(z). \tag{1.12}$$

The increasing density when the resolved fraction of the proton decreases is described e.g. by the Altarelli-Parisi splitting functions[4], $P_{ij}(z)$, which give the probability that a parton i carrying a momentum fraction z originates from a parton j. The splitting functions are calculable as power series in α_s. The diagrams corresponding to the leading order contributions are shown in Figure 1.6. The determination of the parton distribution requires integration over the transverse momenta k_T of the emitted partons along the gluon ladder as shown in Figure 1.7. In the DGLAP approach, the parton emissions are required to be strongly ordered, so that:

$$Q^2 \gg k_{t,n}^2 \gg \ldots \gg k_{t,2}^2 \gg k_{t,1}^2. \tag{1.13}$$

Only in this case Equation 1.11 can be solved numerically. However, this requirement restricts the calculation to the phase space where the parton emissions are strongly ordered in k_T. The splitting functions are expressed in perturbative series involving terms of $\frac{1}{x}$ at higher order. The DGLAP equations neglect this terms if they do not come with a large logarithm of Q^2. However, at low x, these terms become large and cannot be neglected any more. In order to include them, a different approach has been developed. It is expressed as a function of the unintegrated gluon density defined as:

$$xg(x,Q^2) = \int_0^{Q^2} \frac{dk_T^2}{k_T^2} f(x,k_T^2) \tag{1.14}$$

The summation of the leading logarithms of $\frac{1}{x}$ is performed by the BFKL[7] equation. As this equation only involves the unintegrated gluon density, it is no longer necessary to require strong ordering on the parton emissions. Instead, because BFKL sums only $\ln\frac{1}{x}$ terms, a strong ordering on x is required:
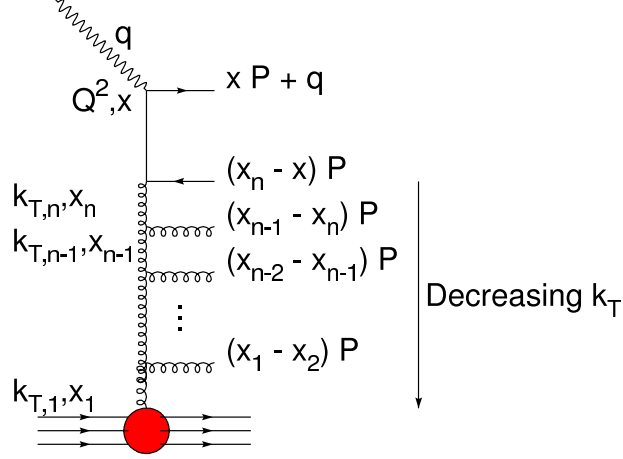
Figure 1.7: *A gluon ladder diagram.*

$$x \ll x_n \ll \ldots \ll x_1. \tag{1.15}$$

The BFKL equation is only valid in the high energy limit when x is low. The CCFM[8, 9, 10] approach attempts to cover both high and low x regions. It deals with the unintegrated gluon density like in the BFKL equation. It is based upon the idea that partons along the gluon ladder shown in Figure 1.7 are emitted with an angular ordering. If θ_i is the angle of the i-th emitted parton with respect to the original direction of the first gluon emitted in the ladder, $\theta_{i+1} > \theta_i$. The maximum allowed angle is defined by the quarks produced by the hard scattering.

1.3 Photoproduction

In photoproduction regime the incoming leptons scatter under small angles and may be treated as a source of quasi-real photons that interact with the proton. The γp center-of-mass energy,

$$s_{\gamma p} = (q + P)^2. \tag{1.16}$$

Consider Q^2 is small and neglecting the mass of the proton:

$$s_{\gamma p} = 4y E_e E_p. \tag{1.17}$$

As long as the ep cross section decreases as Q^{-4} the photoproduction process dominate. The photoproduction cross section,

$$\sigma_{ep} = \int \mathrm{d}y \sigma_{\gamma p}(y) f_{\gamma \to e}(y), \tag{1.18}$$

is calculated from the γp scattering cross section and the photon flux $f_{\gamma \to e}(y)$, that gives the probability for the electron to radiate a quasi real photon carrying fraction of the electron longitudinal momentum, y. The integral boundary conditions are defined from the experimental kinematic cuts. $f_{\gamma \to e}(y)$, integrated to the maximum virtuality, Q^2_{max}, is given in the Weizsäcker-Williams approximation[11] by

$$f_{\gamma \to e}(y) = \frac{\alpha}{2\pi} \frac{1 + (1-y)^2}{y} \ln \frac{Q^2_{max}(1-y)}{m_e^2 y^2}, \qquad (1.19)$$

where m_e is the electron mass.

1.3.1   Structure of the Photon

In the QPM approximation, the photon interacts directly with a parton from the proton as shown in Figure 1.8 (a). However, the uncertainty principle allows the photon to fluctuate into hadronic matter with same quantum numbers[12]. A real photon with energy E_γ fluctuates into $q\bar{q}$-pair with lifetime

$$\tau \approx \frac{E_\gamma}{\sqrt{m_q^2 + p_T^2}}, \qquad (1.20)$$

where m_q and p_T are the mass and the transverse momentum of the quarks. At low p_T, they have time to interact and form bound states, dominated by the light vector meson states ρ^0, ω and ϕ. This picture is described by the *vector dominance model* (VDM) [13]. The *anomalous* or *point-like* component corresponds to the high-p_T (short lifetime) part in Equation 1.20, when the photon fluctuates to a perturbative $q\bar{q}$ state.

The photon structure function $F_2^\gamma(x, Q^2)$ has been measured in e^+e^- experiments, e.g.[14]. The measurements are reasonably described by adding the VDM structure function to the point-like part:

$$F_2^\gamma(x, Q^2) = F_2^{QPM}(x, Q^2) + F_2^{VDM}(x, Q^2) \qquad (1.21)$$

Examples of VDM photoproduction are shown in Figure 1.8 (b,c). Here x_γ is the fraction of the photon momentum, carried by the interacting parton. Taking into account the hadronic structure of the photon, the photoproduction events are divided in two classes:

- **Direct photoproduction** - the photon has no structure

- **Resolved photoproduction** - the photon carries hadronic structure and is considered as a source of partons

The resolved class includes the VDM and the anomalous components. This classification is very convenient in leading order of α_s description but with higher-order contributions to the process, this components appear mixed.
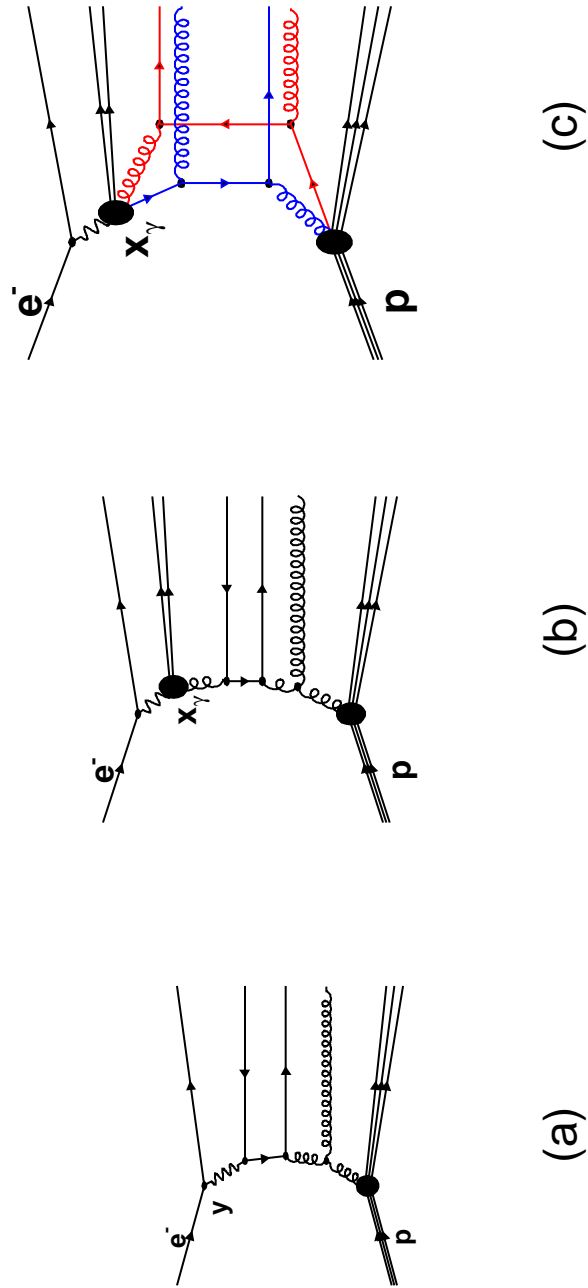
Figure 1.8: *Photoproduction examples: a) direct photoproduction, b) vector dominance model, c) multi-parton interactions*

1.4 Jet Production

In perturbative QCD the cross sections for short distance processes are explained as interactions of colored partons. Due to the confinement of the color charge they cannot be directly observed. According to our understanding, the partons form hadrons in a process called *hadronization*. In a naive picture a final state parton transforms in a collimated spray of hadrons called "jet". Therefore clustering the experimentally accessible hadronic final state could be used to determine the underlying parton structure of the event. The need to associate energy and momentum of hadrons in the final state to four-momenta of unobservable partons is realized by the jet finding algorithms. Jets are an important tool for accessing information about the partonic hard-scattering structure and kinematics. The study of events with three or more high transverse energy jets (multijet production) provides a mean of testing perturbative QCD where the leading order process is of order $\alpha\alpha_s^2$. The multiplicity of additional soft jets, which rises via the emission of the soft gluons in the hard scattering process, could be studied from measurements of events with three or more jets. In jet measurements, the cross sections are measured as a function of two observables, x_γ and x_p. They are defined as follows:

$$x_\gamma = \frac{1}{2yE_e} \sum_{j=1}^{n_{jets}} E_{T,j} e^{-\eta_j}, \tag{1.22}$$

$$x_p = \frac{1}{2E_p} \sum_{j=1}^{n_{jets}} E_{T,j} e^{\eta_j}. \tag{1.23}$$

$E_{T,j}$ and η_j are the transverse energy and the pseudorapidity of the j-th jet, respectively, as explained in Appendix A. In the leading order picture x_γ and x_p represent, respectively, the longitudinal photon and proton momentum fractions entering the hard interaction.

1.4.1 Jet Reconstruction

There are various jet algorithms implemented in the so called jet finders. The requirements for the jet algorithms are:

- **Technically calculable for all levels**.
  At reconstructed level, particles are reconstructed from signals in the detector and then used as an input for the jet algorithm. At hadron level the input for the jet algorithm are the stable particles generated by the Monte Carlo event generator. Jets are measured on reconstructed and hadron level in order to correct the data for detector effects.

- **Infrared safety**
  A jet algorithm is infrared safe if it is insensitive to the emission of low energy particles.

- **Collinear safety**
  Replacing a pair of collinear particles with a single particle carrying the summed momentum should not change the result of the algorithm.

- **Invariance under longitudinal boosts**
  A jet algorithm is invariant under longitudinal boost if the variables used during the jet reconstruction procedure are longitudinally invariant. Examples of such variables are the transverse energy, pseudorapidity and invariant mass.

There are two families of jet definitions. In *cone algorithms*, the direction that maximizes the energy through a cone with fixed radius around it defines the jet axis. *Clustering algorithms* find pairs of particles that are "nearby" in phase-space and merge them together. A jet algorithm must answer two questions:

- When are two particles merged together?

- How are the two particles merged into one?

The answer of the first question is given by the jet resolution variables. The particle merging is done according to the recombination scheme.

1.4.1.1 The longitudinally invariant Kt clustering algorithm

The longitudinally invariant Kt clustering algorithm[15, 16] satisfies the requirements listed above. It has become the **H1** standard jet algorithm and was used as a jet definition for this analysis. It is implemented in a software finder which starts with a list of input particles and an empty list of jets. The default resolution variable is the invariant distance between two particles i and j,

$$R_{ij}^2 = (\eta_i - \eta_j)^2 + (\phi_i - \phi_j)^2. \tag{1.24}$$

All distances between the input particles,

$$r_{ij} = min(p_{T,i}^2, p_{T,j}^2)R_{ij}^2, \tag{1.25}$$

and the distances from each input particle to the beam,

$$r_k = p_{T,k}^2, \tag{1.26}$$

are calculated. Here $p_T^2 = p_x^2 + p_y^2$. If the minimum distance is a distance between two particles, the particles are merged into a new particle according to the recombination scheme. If the smallest distance is a distance to the beam, this particle is moved to the list of jets. In both cases all distances are recalculated. When there are no more particles in the input list the algorithm stops. All input particles are associated with a jet after this procedure.

From the various recombination schemes three will be described:

- **E-scheme**
  Particles are merged by adding their four-vectors. The resulting jets are massive.

- **E_T-scheme**
  The input particles are made massless before the distance calculation by modifying the four momentum components as:

$$(p_x, p_y, p_z, E) \rightarrow (p'_x, p'_y, p'_z, E') \tag{1.27}$$

$$p^2 = p_x^2 + p_y^2 + p_z^2 \tag{1.28}$$

$$p'_{x,y,z} = \frac{p_{x,y,z} E}{p} \tag{1.29}$$

$$E' = E \tag{1.30}$$

The resulting jets are massless and the particle merging is done according to:

$$E_{T,ij} = E_{T,i} + E_{T,j} \tag{1.31}$$

$$\eta_{ij} = \frac{E_{T,i}\eta_i + E_{T,j}\eta_j}{E_{T,i} + E_{T,j}} \tag{1.32}$$

$$\phi_{ij} = \frac{E_{T,i}\phi_i + E_{T,j}\phi_j}{E_{T,i} + E_{T,j}} \tag{1.33}$$

- **p_T-scheme**
  This is the default merging scheme and it was used in the analysis. The resulting jets are massless because the input particles are made massless before the distances are calculated from

$$p'_{x,y,z} = p_{x,y,z} \tag{1.34}$$

$$E' = p \tag{1.35}$$

The particle merging is done according to:

$$p_{t,ij} = p_{t,i} + p_{t,j} \tag{1.36}$$

$$\eta_{ij} = \frac{p_{t,i}\eta_i + p_{t,j}\eta_j}{p_{t,i} + p_{t,j}} \tag{1.37}$$

$$\phi_{ij} = \frac{p_{t,i}\phi_i + p_{t,j}\phi_j}{p_{t,i} + p_{t,j}} \tag{1.38}$$

1.5 Multiparton Interactions

In the VDM model, γp scattering is similar to the *hadron − hadron* collisions. The incoming proton scatters off the hadron-like photon. In this case a parton from the proton interacts with a parton from the photon. However, if the hadron is considered as a composed state of partons, when two hadrons collide it is possible that several distinct pair of partons collide with each other[17]. This is a direct consequence of the composite nature of hadrons. The process is shown in Figure 1.8 (c). This phenomena is expected to affect jet rates. The average number of jets per event is expected to increase when partons from the secondary scattering have significantly high p_T to produce jets. Multiple scattering can influence the jet cross section even when no parton from the secondary interaction is itself of a high enough p_T to produce jet in the observable phase space. The secondary scattering produces extra energy in the event.

The theory that describes the multiple scattering is the theory of *Multiparton interactions* (MI). MI are still not well understood[18]. In order to study these effects different models have been implemented within the hard process generation of several Monte Carlo programs.

A basic discussion of the multiparton interaction is done at a fixed γp center-of-mass energy, $s_{\gamma p}$. The mean number of parton-parton interactions when the proton and the resolved photon collide at some impact parameter, b, is

$$\langle n(b, s_{\gamma p}) \rangle = \mathcal{L}_{partons} \otimes \hat{\sigma}_H, \tag{1.39}$$

where $\mathcal{L}_{partons}$ is the parton luminosity and $\hat{\sigma}_H$ is the cross section for a pair of partons to produce a pair of jets. A small b value corresponds to a large overlap between the two colliding hadrons. At large b the probability that no parton interaction takes place at all becomes large. The relation between the parton luminosity and the number density of partons in the incoming particles is

$$d\mathcal{L}_{partons} = A(b)n_\gamma(x_\gamma)n_p(x_p)dx_\gamma dx_p, \tag{1.40}$$

where $n_i(x_i)$ is the number density of partons in hadron i and $A(b)$ is a function which specifies the distribution of partons in impact parameter. It must satisfy

$$\int \pi db^2 A(b) = 1 \tag{1.41}$$

in order that the parton density integrated over all space is simply the product of the parton number densities. Now Equation 1.39 can be written as

$$\langle n(b, s_{\gamma p}) \rangle = A(b)\sigma_H^{inc}(s_{\gamma p}), \tag{1.42}$$

where σ_H^{inc} is the inclusive jet pair cross section in photoproduction. The main assumption is that the separate scatters are uncorrelated. This means that they obey Poissonian statistics. Then the probability distribution for m (and only m) parton interactions in a given event is
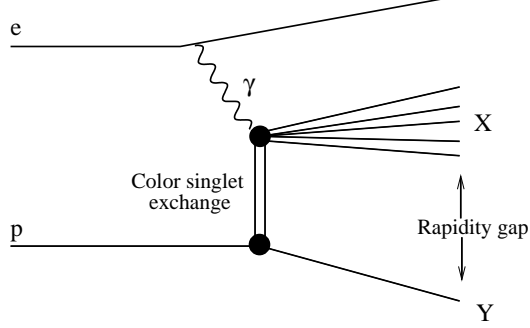
Figure 1.9: *Schematic diagram of diffractive scattering. The upper black dot which illustrates the fragmentation into the system X includes higher order QCD reactions.*

$$P_m = \frac{(\langle n(b, s_{\gamma p})\rangle)^m}{m!} \exp(-\langle n(b, s_{\gamma p})\rangle). \tag{1.43}$$

And the total cross section for $\gamma p \rightarrow$ partons is

$$\sigma_H(s_{\gamma p}) = \pi \int db^2 \sum_{m=1}^{\infty} P_m = \pi \int db^2 [1 - \exp(-\langle n(b, s_{\gamma p})\rangle)]. \tag{1.44}$$

The inclusive jet cross section, σ_H^{inc}, counts all pairs of jets even if they occur in the same event. It is expected to be larger than σ_H by a factor equal to the mean number of multiple interaction per event:

$$\langle n(s_{\gamma p})\rangle = \frac{\sigma_H^{inc}(s_{\gamma p})}{\sigma_H(s_{\gamma p})} \tag{1.45}$$

While σ_H must always be smaller than the total γp cross section, σ_H^{inc} needs not to be.

1.6   Diffraction

Experimentally, diffractive events are characterized by the lack of activity in the detector close to the proton direction (rapidity gap). The diffractive ep scattering is explained by the absence of color flow close to the proton. This is in contrast with the non-diffractive process where the exchanged parton forms a color string between the interacting particles which breaks up and fragments into hadrons. The color singlet exchange can be described by introducing a pseudo-particle called **pomeron**. A schematic diagram of such an event is shown in Figure 1.9.

Chapter 2

The Experiment

The **H1** experiment is based at *Deutsches Elektronen-Synchrotron* (DESY) in Hamburg, Germany. It observes high-energy collisions of electrons and protons. The main objective of **H1** is the study of the internal structure of the proton.

The *Hadron Electron Ring Accelerator* (HERA) [19] is a is the only one in the world in which different types of particles are accelerated. The 6.3 km double-ring collider accelerates 100 mA protons to an energy of 920 GeV for interactions with 27.5 GeV electrons or positrons with a current of about 50 mA using 174 colliding bunches. The bunch crossing interval is 96 ns, corresponding to a bunch crossing rate of 10.4 MHz. In the two *interaction regions* in the north and south, the experiments **H1** and ZEUS are installed. In addition the HERMES beam-target experiment investigates the polarized quark-gluon structure of nucleons using collisions between the polarized lepton beam and a polarized gas target. HERA-B uses the proton beam to investigate the properties of heavy quarks. HERA was approved in the year 1984 and commissioned in 1991. Luminosity operations started in 1992. During the first HERA operation phase (years 1992-2000), **H1** and ZEUS together collected an integrated luminosity of about 200 pb^{-1} of data. In 2000/2001 the interaction regions of **H1** and ZEUS were modified to provide a factor of 2.7 more specific luminosity by optimizing the beam optics[20]. In the end of June 2007 HERA concluded operation after 16 successful years. Figure 2.1 shows the very last HERA run. In total HERA delivered to **H1** and ZEUS 500 pb^{-1} each. The total integrated luminosity delivered to **H1** is shown in Figure 2.2.

H1 began operating together with HERA in 1992. The international collaboration operating the experiment consist of more than 400 physicists from 42 institutes in 15 countries. The detector is about 12 x 15 x 10 m big and weighs 2800 tons. A three stories high electronics trailer is attached. In the design of the **H1** detector[21] prime attention has been given to the identification and energy measurement of electrons. The superconducting coil is located outside the electromagnetic and the hadronic calorimeters to minimize the amount of dead material in front
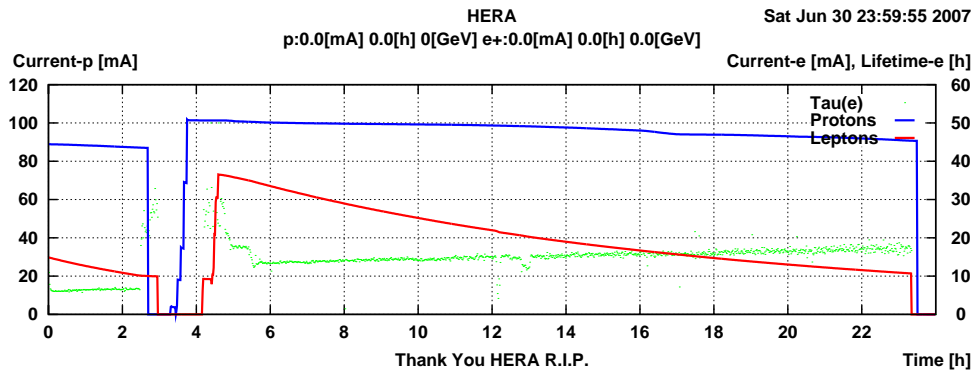
Figure 2.1: *The very last HERA luminosity run with the proton current in blue and positron current and lifetime in red and green, respectively.*
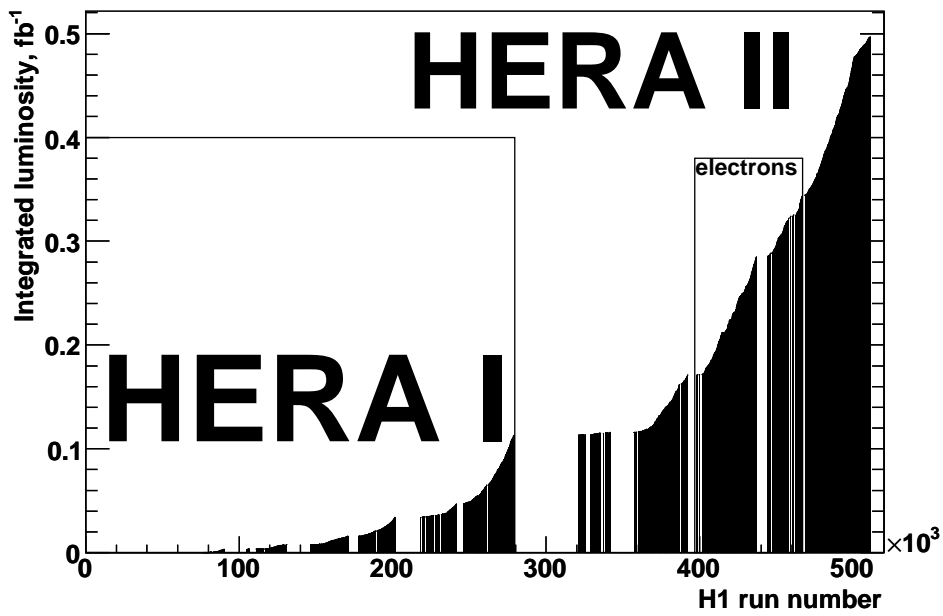
Figure 2.2: *Delivered luminosity of HERA I and II as a function of H1 run number. Shown is also the electron period for HERA II.*

of the calorimeter. The calorimeter system is designed to measure the energy of scattered and newly produced particles. It is supplemented by the central and forward tracking devices on the inside and an instrumental iron yoke on the outside for muons detection. The tracking devices are used to reconstruct tracks from charged particles, their transverse momentum and direction Θ and ϕ with respect to the vertex (see 2.1). A detailed longitudinal view of the central part of **H1** is shown in Figure 2.3. Since the center of mass for e-p collisions at HERA is boosted along the proton direction the **H1** detector is designed asymmetric. The three major components of the detector, the tracking, calorimeter and muon detectors are described in [22]. Here only a short overview of the most important detector components for the performed analysis is presented.

2.1 Laboratory frame

The **H1** laboratory frame is defined by a right-handed Cartesian coordinate system with the positive z-axis points along the proton beam direction. The proton direction is called *forward*. Correspondingly the direction of electron is called backward with negative z and $\Theta = \pi$ (polar angles Θ are defined with respect to the positive z-direction). The x-axis and y-axis point to the center of the HERA ring and upwards respectively. Azimuthal angles ϕ are defined such that $\phi = 0$ points to the positive x-direction.

In this frame, if the masses of the proton and the electron are neglected, the four-momenta components of the incoming proton, the incoming electron and the scattered electron are:

$$P = (E_p, 0, 0, E_p), \tag{2.1}$$

$$k = (E_e, 0, 0, -E_e), \tag{2.2}$$

$$k' = (E_{e'}, \sin\theta_{e'}\cos\varphi_{e'}E_{e'}, \sin\theta_{e'}\sin\varphi_{e'}E_{e'}, -E'_e\cos\theta_{e'}), \tag{2.3}$$

where E_p, E_e and $E_{e'}$ are the energies of the incoming proton, incoming and scattered electron respectively. The electron scattering angle is denoted as $\theta_{e'}$.

2.2 Calorimetry

A schematic view of **H1** calorimeter devises is shown in Figure 2.4. Several sub-detectors, each with nearly full azimuthal acceptance form the calorimeter system.

- The main **H1** calorimeter, *liquid argon* (LAr) calorimeter, covers a polar range of $4° < \Theta < 154°$ and is divided in *electromagnetic* and *hadronic* calorimeter.

- In the backward region ($153° < \Theta < 177°$) energy is detected by a lead/scintillating fibre *Spaghetti-type calorimeter* (SPACAL).
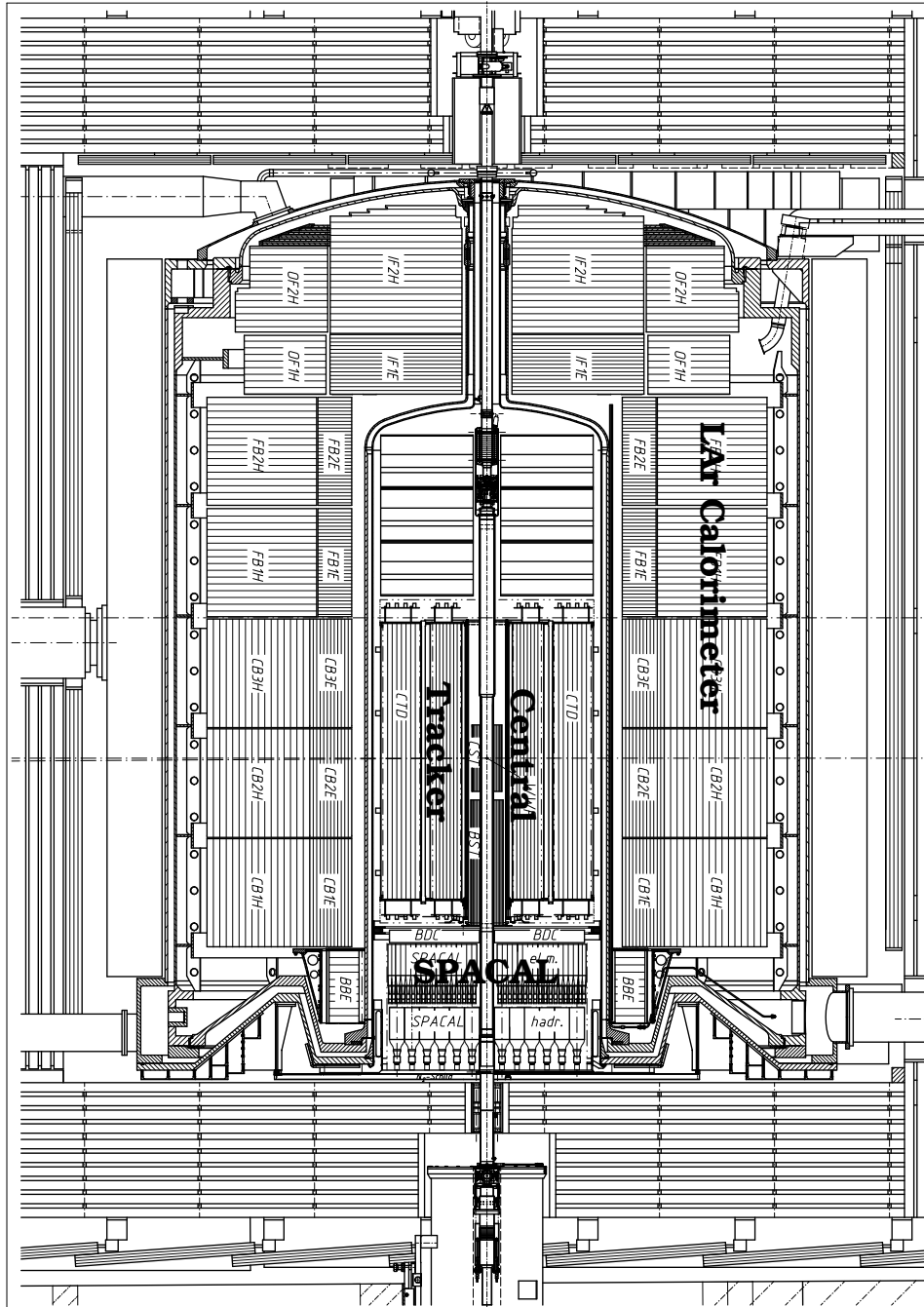
Figure 2.3: *Detailed longitudinal view of the H1 detector at HERA.*
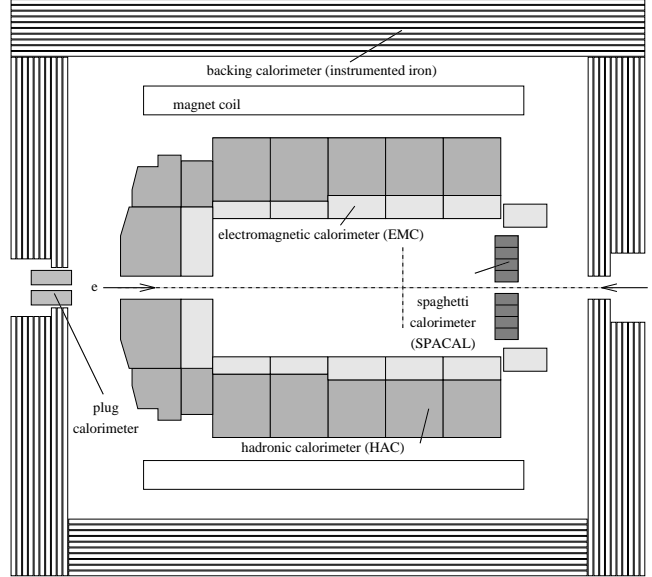
Figure 2.4: *A schematic longitudinal view of the H1 calorimetric devices.*

- The *plug calorimeter* closes the gap in acceptance between LAr and the beam pipe in the forward region $0.7\,^\circ < \Theta < 3.3\,^\circ$.

- The *instrumented iron* is used both for muon identification and calorimetric measurement of hadronic particles leaking out of the LAr calorimeter.

2.2.1 Spaghetti Calorimeter

The spaghetti calorimeter is a *sampling* calorimeter, i.e. different materials are employed for the absorption and detection of particles. For the SPACAL lead is used as absorber material while the active material are scintillating fibres. The incident particles produce a shower of secondary particles in the lead which cause the fibres to scintillate. The amount of light registered by photomultiplier tubes is a measure for the energy of the primary particle.

The SPACAL consists of an electromagnetic and a hadronic section. The electromagnetic part consists of 1192 cells with a total depth of 28 radiation lengths and energy resolution of 7 %. The hadronic section consists of 136 cells and adds around 1 hadronic radiation length. Therefore it can provide only rough hadronic energy measurement, but allows to distinguish between electromagnetic and hadronic showers.

2.2.2 Liquid Argon Calorimeter

The liquid argon calorimeter[23] is situated inside the solenoid to reduce the amount of dead material, particles have to traverse before they are absorbed in the calorime-
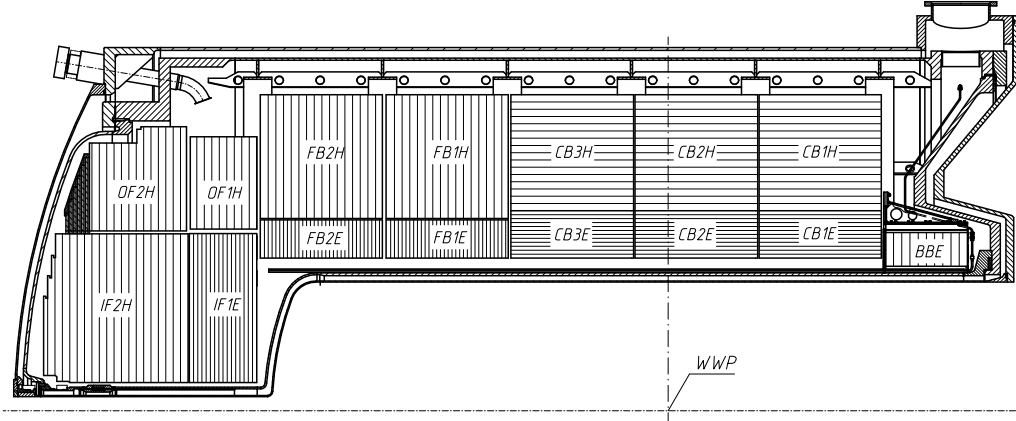
Figure 2.5: *Detailed longitudinal view of the main H1 calorimeter - LAr with eight support-ing wheels.*

ter. It is a sampling calorimeter using liquid argon as active material. The electro-magnetic and hadronic parts share a single liquid argon cryostat. The only difference between them apart from the geometry is the absorber plates material which is lead and steel respectively. The geometrical segmentation along the beam axis includes eight self supporting wheels. Every wheel is divided into an inner, electromagnetic section and an outer, hadronic section except the most backward wheel, (see Fig-ure 2.5) with an electromagnetic section only and the most forward wheel with two hadronic sections. In order to obtain an uniform energy resolution the absorber plates orientation is chosen such that particle originating from the interaction region cross them with an angle larger than $45\,^\circ$.

The fine granularity of the LAr calorimeter reflects in a total number of about 44000 cells. The readout system provides calibrated charges for each cell. Then the charges are converted to energy in several steps including corrections for dead material effects. These reconstruction steps provide the correct energy for electrons and photons. Since the LAr calorimeter is non-compensating the charge output for hadrons is about $30\,\%$ smaller than for electrons of the same energy. A weighting technique is employed offline to correct for this effect.

The systematic uncertainty of the electromagnetic energy scale varies between $0.7\,\%$ and $3\,\%$ depending on the wheel. The uncertainty of the hadronic energy scale is between $1.5\,\%$ and $4\,\%$.

2.3   Tracking

The tracking system is divided between the central, forward and backward regions (see Figure 2.6).

- The *central tracking detector* covers the polar angles in the range of $25\,^\circ < \Theta < 155\,^\circ$.
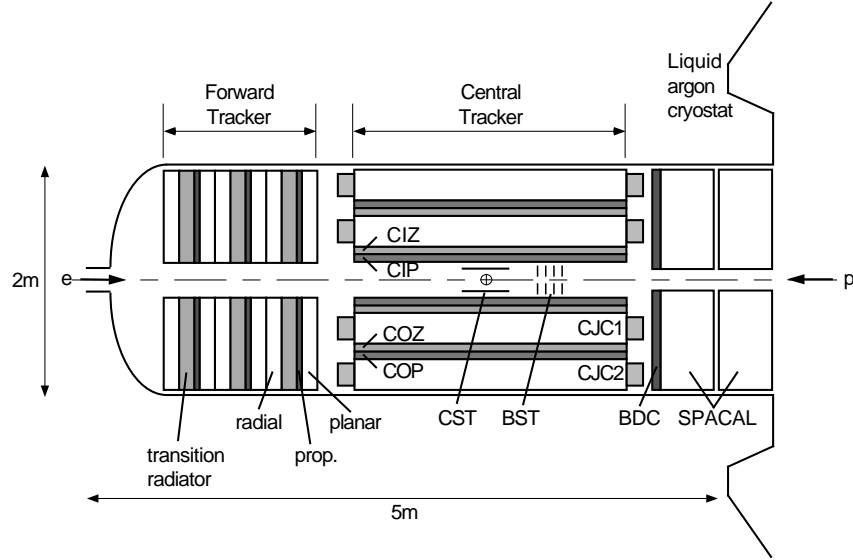
Figure 2.6: *A schematic longitudinal view of the H1 tracking system. The SPACAL calorimeter is also shown.*

- The forward region is covered by the *forward tracking detector* (FTD) used to identify tracks with $5\,^\circ < \Theta < 25\,^\circ$.

- The *backward drift chamber* (BDC) is located in front of SPACAL. It is designed to measure tracks in the range of $155\,^\circ < \Theta < 175\,^\circ$. At HERA II BDC was replaced with *backward proportional chamber* (BPC).

A superconducting solenoid which surrounds both the tracking system and the LAr(see 2.2) provides a uniform magnetic field of 1.15 T.

2.3.1 Central Tracking Detector

All tracking devices which are part of the central tracker are shown in Figure 2.7.

The main components of the central tracking detector are the two *central jet chambers*, CJC1 and CJC2. These are two concentric drift chambers with active length of 220 cm along the beam pipe and radial extension of 20.3< r <45.1 cm (CJC1) and 53.0< r <84.4 cm (CJC2).

The track reconstruction is based on the ionization of a gas mixture ($Ar - CO_2 - CH_4$) by the charged particles. The free electrons produced are detected on 2640 signal wires strung parallel to the z-axis and organized in 30/90 drift cells for CJC1/2. The drift cells are inclined by about $30\,^\circ$ with respect to the radial direction. This way the ionization electrons in the presence of the magnetic field drift approximately perpendicular to high momentum tracks originating from the beam axis which guarantees an optimal track resolution. The spatial reconstruction in $r\phi$-plane is based on the measurement of the drift time of the ionization electrons. A charge division
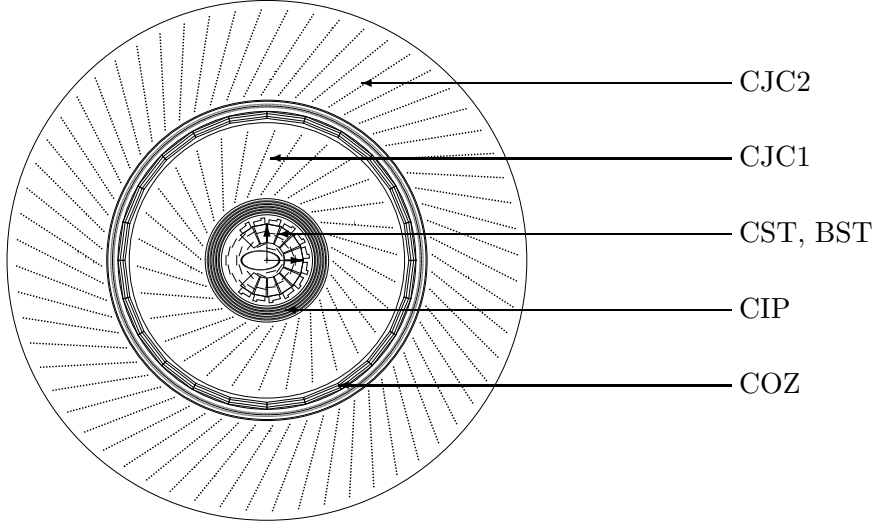
Figure 2.7: *Radial view of the central tracker. The silicon detectors CST, BST and FST are closest to the beam pipe, followed by CIP, CJC1, COZ and CJC2.*

technique is used to determine the z-coordinate. The achieved spatial resolution is $\sigma_{r\phi} = 170\,\mu\mathrm{m}$ and $\sigma_z = 22\,\mathrm{mm}$.

In addition to the track reconstruction CJC1/2 provide information for the particle identification by measuring the specific energy loss of charged particles dE/dx with a resolution of $\sigma_{dE/dx}/(dE/dx) \approx 8\,\%$.

The *central inner proportional* (CIP) chamber is a multiwire proportional chamber. It is the wire chamber sitting closest to the beam line and delivers a fast timing signal with a resolution better than the time interval of $96\,\mathrm{ns}$ between two HERA bunch crossings. This signals are used by the central trigger for on-line selection of events with charged particles originating from the nominal interaction vertex.

The *central outer z-chamber* (COZ) is attached outside of the CJC1. The wires of COZ are oriented perpendicularly to the beam axis. This device is designed for reconstruction of the z-coordinate. The spatial resolution of $\sigma_z = 350\,\mu\mathrm{m}$ is significantly better than the one for the central jet chambers. The azimuthal resolution of COZ, $\sigma_{r\phi} = 25\,\mathrm{mm}$.

In addition to the wire chambers, **H1** is equipped with a silicon vertex tracking detector. It is comprising a barrel part and two endcaps with disks[24]. The *central* (CST), *backward* (BST) and *forward silicon detector* (FST) are closest to the beam pipe and the interaction point. The silicon detectors measure hits produced of charged particles with a very high resolution via ionization in semiconductors and cover the polar angles:

- FST $8\,° < \theta < 16\,°$

- BST $162\,° < \theta < 176\,°$

- CST $30° < \theta < 150°$

2.4 Luminosity System

The relation between the cross section of a given process $\sigma_{process}$ and the observed number of events $N_{process}$ is:

$$\sigma_{process} = \frac{N_{process}}{\mathcal{L}_{int}};$$

(2.4)

Here $\mathcal{L}_{int}$ is for the integrated luminosity represented by the data sample. The measurement of any cross section requires a precise knowledge of $\mathcal{L}_{int}$. It can be determined by measuring the event rate of a process with well known cross section. In the **H1** detector the elastic bremsstrahlung $ep \to e\gamma p$ (Bethe-Heitler process) is used for this purpose. The scattered electron and the emitted photon are measured by the *electron tagger* and the *photon detector* located at z-position of - 6 m and - 102.8 m respectively. The uncertainty of the luminosity measurement is 2.5 % for the data taking period covered in this analysis.

2.5 Time of Flight System

The *time of flight* (TOF) system is designed to veto on background events induced by collision of proton beam particles with the wall of the beam pipe or residual gas molecules. For this purpose several scintillation detectors with a small time resolution of 2-4 ns are mounted around the beam pipe at various distances from the interaction point. Based on the precise timing knowledge for the bunch crossing in the detector provided by the HERA machine (HERA clock), this time resolution allows to distinguish the actual collision events.

Chapter 3

H1 Trigger

The event rate of ep interactions in the **H1** detector is small in comparison to the rates of background processes. Some typical sources of background are:

- Collisions of beam protons with the rest gas in the vacuum pipe, (proton-gas) or the pipe itself, (proton-wall) interactions. In both cases, the interaction takes place on a nucleus (C, N, O or even Cu and W if the interaction occurs with a collimator material).

- Collisions of particles between bunches(satellites)

- Synchrotron radiation from the electron beam

The trigger is designed to select the ep interaction events for permanent recording. The **H1** subdetector systems store the detector information into dedicated front-end pipelines and generate in parallel fast information for the general properties of every event. The latter is sent to the *Central Trigger* (CT) where the decision on acceptance for readout of the event is taken.

3.1 Trigger Overview

The **H1** trigger works in four trigger levels designated as L1,L2,L3 and L4[25]. An overview of the trigger levels is given in Table 3.1.

Every subdetector system which delivers trigger information has a subdetector trigger system. The CT communicates with the subdetector trigger systems via signals synchronized to the HERA clock. For every bunch crossing the trigger systems calculate dedicated bits and send them to the CT. These bits are called *trigger elements* (TE's).

L1 provides a trigger decision for every bunch crossing with a delay of $2.5\,\mu s$ [26, 27]. To avoid L1 deadtime the subsystems store their data in dedicated

Table 3.1: *The four trigger levels of the detector*

	description	decision time, μs	output rate, Hz
L1	Deadtime free pipelined hardware	2.5	1000
L2	Hardware	22	150
L3	Software	100	50
L4	Software event reconstruction running in a processor farm	500000	20

pipelines with minimum length determined by this delay. In case of positive decision the L1Keep signal is broadcast by the CT. The subsystem front-end pipelines are frozen and the generation of deadtime begins.

L2 operates in more detail on the information from the subsystems during the primary deadtime with a fixed decision time. If the event is validated on L2 CT broadcasts L2Keep signal and the readout of the event from pipelines in the multi-event buffer begins. In case of L2Reject the pipelines are cleared and open again.

L3 is a software system designed to reconstruct the event properties and particle decay resonances using a fast tracks reconstruction based on the information from CJC1 and CJC2. The deadtime generation ends after L3Reject or after the end of the readout.

L4 farm performs partial event reconstruction and assigns a physics class to each event based on software finders. Only a small fraction of non-classified events is kept. This reduces the event rate to the final value of 20 Hz, consistent with the data storage capacity.

3.2   Trigger Basics

The first three trigger levels are controlled by the central trigger by means of the *subtriggers* (ST's), logical or numerical expressions with trigger elements as argument. For each event, ST decision bits are assigned at every level. In general these bits are divided in *raw* and *actual* (ac) bits. The *raw* decision bit shows if the defined ST condition is satisfied. The *actual* bit is a result of verification. Following this concept, raw and actual rates are distinguished.

3.2.1   Trigger Level 1

In total 256 L1 TE's are received and combined by the central trigger logic to 128 L1 ST's. The raw ($L1^{raw}$) and the actual ($L1^{ac}$) ST decision bits at L1 are:
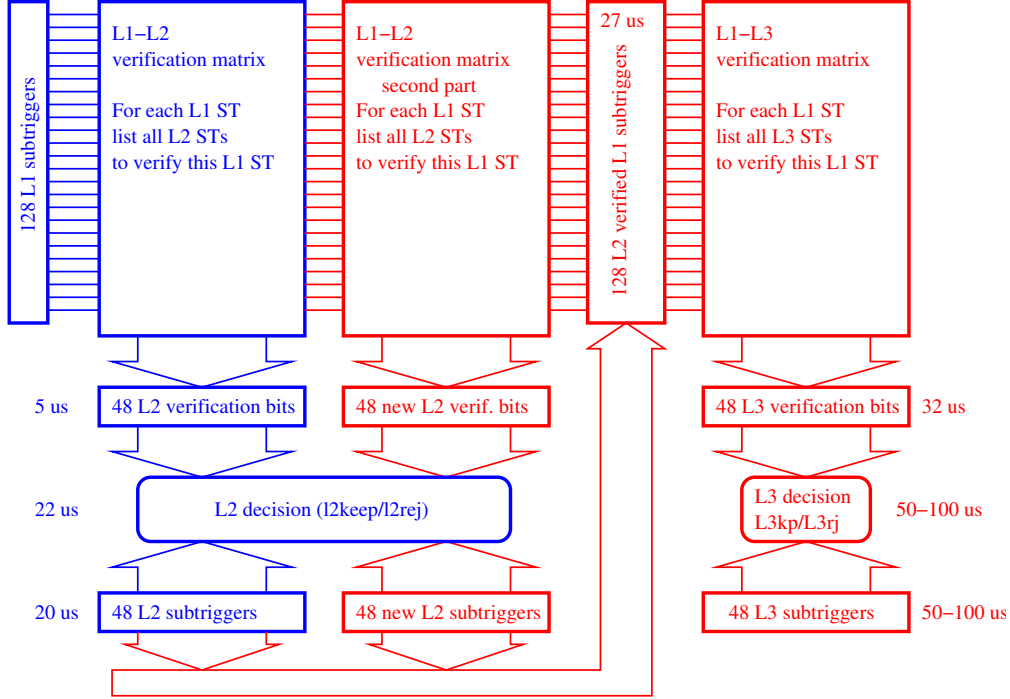
Figure 3.1: *The CT before (in blue) and after the hardware upgrade in May 2005 when FTT L2 and L3 were activated.*

$$L1_i^{raw}, \quad L1_i^{ac} \quad (i = 0, 127). \tag{3.1}$$

On L1, every actual ST bit depends on a positive number called *prescale factor* (PF). For PF= n, the actual bit is active every n events with enabled raw bit. An event is kept on L1 if at least one L1 ST actual bit is enabled:

$$\text{L1Keep} = \sum_{j=0}^{127} L1_j^{ac} \tag{3.2}$$

3.2.2 Trigger Level 2

After L1Keep, additional trigger information is sent to three independent L2 systems[27]. The L2 neural network system[28] calculates up to 16 L2 TE's. The neural networks are trained with previously recorded or simulated data samples with events from physics processes of interest and background so they are able to separate both contributions. The L2 topological trigger[29] calculates 16 TE's. In May 2005 the CT hardware was upgraded. The main purpose was to open new physics channels. Added were 24 new TE's, calculated by L2 *fast track trigger* (FTT) [30]. The upgrade is shown in Figure 3.1 [31]. FTT is a trigger subsystem that provides trigger elements on L1, L2 and L3 using a fast track information from CJC.

The L2 TE's are combined in 96 L2 ST's. The actual bits, $L2^{ac}$, are calculated after the raw decision bits, $L2^{ac}$, from L2NN, L2TT and L2FTT have been delivered to the CT.

$$L2_i^{ac} = V2_i L2_i^{raw} \quad (i = 0, 95), \tag{3.3}$$

$$V2_i = \sum_{j=0}^{127} M_{ij}^{12} L1_j^{ac} \tag{3.4}$$

The L2 validation vector, $V2$, is calculated from the L1-L2 verification matrix M_{ij}^{12} and the $L1^{ac}$ bits. Actually, $V2$ verifies the $L2^{raw}$ decision bits. It is done this way because the calculation of the vector is the main time consuming procedure in the CT. The summation over all ST's takes around $18\,\mu$s. However, performed this way, the calculation of $V2$ does not rely on L2 information and is done during the $22\,\mu$s needed by the L2 trigger subsystems to deliver the $L2^{raw}$ bits. In result, no extra time for this calculation is needed.

The L2 decision is based on the L2 ST actual bits:

$$\text{L2Keep} = \sum_{i=0}^{95} L2_i^{ac}. \tag{3.5}$$

3.2.3   Trigger Level 3

The L3 verification level started to work after the upgrade in 2005. Up to 48 L3 TE's are calculated by the L3 FTT. Within the L1, FTT works with the two dimensional and within L2, with the three dimensional track information. The FTT TE's are based on the track momenta, multiplicity and topology. On L3, the FTT performs invariant mass calculations to identify exclusive final states like D^* and J/ψ. Dedicated selection algorithms are executed on a software computer farm. In addition, L3 FTT identifies electrons with energies down to $1.2\,$GeV. For this purpose, the FTT matches tracks geometrically using the L1 trigger information about the energy measurement delivered by the calorimeter based jet trigger subsystem[32]. The L3FTT muon finder combines track information with information from the muon trigger subsystem.

The combination of L3 TE's in subtriggers is not necessary because they already have a clear physics channel assigned. Hence, on L3, TE's and ST's have one to one correspondence. The L3FTT dispose of about $100\,\mu$s to deliver the L3 raw ST decision bits, $L3^{raw}$, to the central trigger. As the calculation of the validation vector, $V3$, takes 60-$70\,\mu$s, this time is used to calculate the L2 verified L1 ST bits ($L1L2^{ac}$) and $V3$.

$$L1L2_j^{ac} = L1_j^{ac} \sum_{i=0}^{95} M_{ij}^{12} L2_i^{ac}, \tag{3.6}$$

$$V3_i = \sum_{j=0}^{127} M_{ij}^{13} L1L2_j^{ac}, \tag{3.7}$$

where M^{13} is the L1-L3 verification matrix. The actual L3 bits ($L3_i^{ac}$), the L3 verified ($L1L3^{ac}$) and L2/3 verified L1 ST bits ($L1L2L3^{ac}$) are calculated after the $L3^{raw}$ decision bits have been delivered to the CT as

$$L3_i^{ac} = V3_i L3_i^{raw} \quad (i = 0, 47), \tag{3.8}$$

$$L1L3_j^{ac} = L1_j^{ac} \sum_{i=0}^{47} M_{ij}^{13} L3_i^{ac}, \tag{3.9}$$

$$L1L2L3_j^{ac} = L1_j^{ac} (\sum_{i=0}^{95} M_{ij}^{12} L2_i^{ac})(\sum_{i=0}^{47} M_{ij}^{13} L3_i^{ac}) \tag{3.10}$$

The L3 decision is taken by

$$\text{L3Keep} = \sum_{i=0}^{47} L3_i^{ac}. \tag{3.11}$$

Similarly to the actual validated bits, the raw validated bits are also calculated. Although not used in the trigger decision they are often needed in offline trigger studies. In example, the L2 verified L1 raw bits,

$$L1L2_j^{raw} = L1_j^{raw} \sum_{i=0}^{95} M_{ij}^{12} L2_i^{raw}, \tag{3.12}$$

are used in the trigger efficiency calculation as it will be discussed in Section 3.4. The L2/3 verified L1 raw decision bits,

$$L1L2L3_j^{raw} = L1_j^{raw} (\sum_{i=0}^{95} M_{ij}^{12} L2_i^{raw})(\sum_{i=0}^{47} M_{ij}^{13} L3_i^{raw}), \tag{3.13}$$

are used in the calculation of the prescale factors, discussed in Section 3.3.

3.2.4 Trigger Level 4

The highest level trigger L4 decision is based upon a complete information about the fully reconstructed event. Event rejection at this level means in fact downscaling, i.e. there is no *absolute rejection* of any kind of data. Some fraction is always kept, with the corresponding weight assigned to it. Hence a proper use of the L4 event weight guarantees statistically correct account for any potential L4 bias.

The events are classified using software finders. The list of the event classification bits for HERA2 is shown in Table 3.2. In this table, also the corresponding number of classified events for three different running periods is listed. L4 copies all L2/L3 verified raw subtrigger bits, $L1L2L3^{raw}$, into a L4 verified array. Depending on the

Table 3.2: *The trigger level 4 classes with corresponding number of events.*

Class	Physics content	fall-2003	2004 (+P)	2004 (-P)
0	Not classified junk	1333081	948809	1464555
1	Pilot bunches	1558559	758860	739091
2	Lumi (DIS/BH overl)	89398	579331	652062
3	Soft physics	17810276	7661854	7856173
4	High Q**2	2650505	4635261	6617577
5	High ET_total	503647	686442	851887
6	High ET_miss	2399550	3601257	5063479
7	High_ET_jets	2622346	4287455	6104142
8	High_Pt_central	141939	552419	704593
9	High_Pt_forward	0	1089105	2910604
10	High_Pt_muons	398180	1412947	1563955
11	Multi-jets	1128408	2660026	3535009
12	Multi-particles	357461	1675126	2073489
13	Diffraction	279818	3604753	2818687
14	Leading baryons	62435	462750	1125022
15	HQ open	301207	1371434	1727295
16	HQ closed	281641	1939988	2335755
17	Photons (ISR,QEDC)	747188	978687	1167596
18	High-y DIS (FL)	591668	3018106	4123087
19	Electron in LAr	3268385	5172858	7063485
20	Electron in Spacal	5450190	13015757	15202658
21	Electron in VLQ	0	0	0
22	Electron in E-tags	2186205	2997928	4097950
23	Photon in Lumi_PD	3292312	4912777	6038951
24	Muons	806600	2084396	2321755
25	Hotline	17337	48345	51450
26	(Free quarks)	0	0	0
27	Diffractive flag	11510216	10002102	12155586
28	Jets (Et > 5 GeV)	5855359	8468927	11433060
29	High W2	5264959	12855898	15365058
30	Cosmics	1045593	1518497	1595983
3	Soft (downscaled)	17810276	7661854	7856173
4-10	Hard scale physics	3777118	8312273	12632866
11-18	Excl. Final states	2915629	11489949	14001088
Total		25074759	26253468	32814386

finder results, some bits are reset. The event is marked as class 0 if all L1 trigger bits after L4 resetting are zero. A fraction of 10 % of this events is kept to enable the monitoring of the eventual physics losses at L4.

3.2.5 Operation

During a HERA luminosity fill (a period of time when the beam energies are at their design values and beam optics are set appropriately for collisions) the **H1** experiment tries to collect the maximum number of *ep* interaction events. For this purpose the *shift crew* must ensure the following:

1. All subdetector components are running (their *high voltage* (HV) is on).

2. The detector deadtime is below the 10% level.

An important time unit for the **H1** data taking is the **H1** *run*. This should not be mistaken with the HERA luminosity fill which has a typical time length of 10 hours. There are a number of **H1** runs in one HERA luminosity fill. At HERA the incoming beam currents and the background rates are not constant during one luminosity fill and could differ for different fills. This leads to a non-constant total rate as well as ratio between the different physics ST rates. The rates vary as a consequence of fluctuations in the beam parameters, subdetector thresholds and even e.g. with changes in the atmospheric pressure. The trigger must be able to deal with smooth and unexpected changes in the trigger rates.

3.3 Trigger Strategy

As long as the L4 input rate is below 50 Hz no further deadtime apart from previously mentioned in Section 3.1 is generated. In this region the deadtime is a linear function of the L4 input rate. Above this value, the limited readout capacity adds non-linear effects to the deadtime increase, as shown in Figure 3.2.

Keeping the total L4 input rate below 50 Hz and the same time recording physics channels which greatly differ in rate is a nontrivial task. For this purpose, prescale factors are assigned to every ST. Assigning fixed downscale factors to the ST's is not an ultimate decision. Instead, the priority between the different ST's is fixed. This priority is defined by a set of rules called *autoprescale strategy*. In the strategy, the ST's are combined in groups and subgroups in a tree-like structure according to their physics purpose. Rules can be assigned to the groups and to the individual ST's. The possible rules are:

- relative weight

- fixed PF

- fixed target rate

- optional minimum or maximum rate
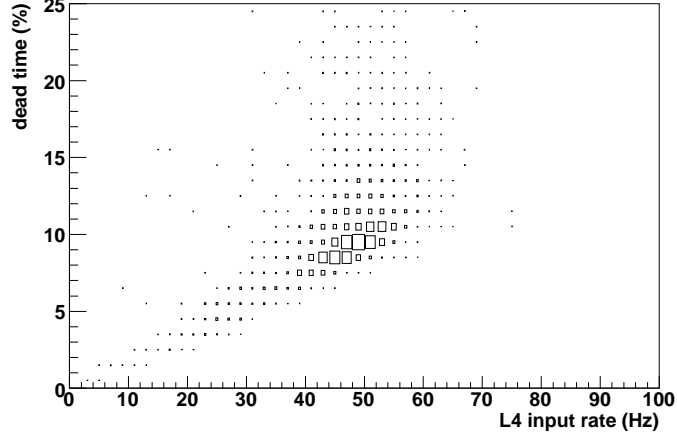
Figure 3.2: *The correlation between the H1 deadtime and the L4 input rate. For rates above 50 Hz the value of the deadtime is non linear function of the L4 input rate.*

The PF's are calculated according to the autoprescale strategy. To account for the changes in the running conditions, an *event sample* is used. It is a record of the trigger statistics from the last 1000 triggered events before the calculation performance. The event sample contains:

- The PF's in use

- The L2/3 validated L1 raw ST decision bits (as in Equation 3.13) for each event

- The HV bits for each event

The individual ST rates could be taken from the event sample by counting the ST bits. However, if the overlap between different ST's is large, the cumulative rate cannot be calculated as a sum of the individual ST rates. A prediction for the cumulative trigger rate can be achieved by *reweight the event sample*[33].

For every event j, the probability P_{jk} to be accepted after downscaling by at least one of N ST's can be calculated as

$$P_{jk} = 1 - \prod_{i=1}^{N} (1 - \frac{L1L2L3_{ij}^{raw}}{PF_{ik}}), \tag{3.14}$$

where PF_{ik} is the prescale factor defined by a given set of prescale factors k. The ratio of the probability $P_{jk'}$ evaluated with a new set of PF's to the probability obtained with the active PF set is assigned as a weight to each event. The new cumulative rate is then calculated as the sum of the weights, divided by the time during which the event sample was collected:

$$\nu_{k'} = \frac{1}{T} \sum_{j=1}^{1000} \frac{P_{jk'}}{P_{jk}}. \tag{3.15}$$

The optimized PF's are calculated by an iterative procedure. The calculation begins with the determination of the *budget* (maximum) rates from the autoprescale strategy. Then for each iterative step the predicted cumulative rates are calculated as described above and the PF's are corrected according to the budget. If correctly implemented, the procedure should converge to a set of PF's and corresponding predicted rates in agreement with the strategy.

The autoprescale calculation could be performed in case of an unexpected change in the data taking conditions to improve the trigger performance immediately or regularly, following the decrease in the beam currents. In addition, the autoprescale calculation could be used in offline trigger performance checks, when tests of a new strategy are necessary.

3.4 Trigger Efficiency

The cross section of a specific physics process is proportional to the event rate of that process. The latter differs from the rate of the events kept by the trigger. Two different contributions to this difference are distinguished:

- The trigger prescale factor

- The trigger efficiency

The efficiency of an analysis ST, A, is defined as the ratio of the number of events triggered by A to the number of event happened. One way to determine how many events happened is to use a *reference* trigger. The analysis and reference subtriggers must not have common trigger elements or trigger elements delivered by the same subdetector system. This ensures that they are independent.

The calculation of the trigger efficiency is possible after the events of interest have been selected. In example, the efficiency of the subtrigger A on L2 is calculated as

$$\epsilon_A = \frac{N(L1L2_A^{raw} \& L1L2L3_R^{ac})}{N(L1L2L3_R^{ac})}, \tag{3.16}$$

where $N(bits)$ denotes the number of selected events with enabled *bits*, the sign & indicates overlap, A is for the analysis and R is for the reference subtrigger. The decision bits used in the formula are defined in Section 3.2.3, Equation 3.10 and Equation 3.12.

The prescale factor correction is applied during the integrated luminosity calculation and ignored in the trigger efficiency calculation. As long as the mean prescale factor of a subtrigger is well-known, it does not add any trigger inefficiency.

Chapter 4

Monte Carlo Event Generators

A simulation of the **H1** detector is needed to obtain universal machine independent results. More important, without a detailed detector simulation, it is not possible to understand the detector acceptance and resolution.

The event simulation steps are shown in Figure 4.1. Particles are generated by Monte Carlo programs and used as input for the **H1** *detector simulation*. During this step the response of the detector is simulated. The *particle reconstruction* is common for the real and simulated detector response. This is done to account for the limited detector acceptance and resolution. The universal measurement results, independent of the detector, are obtained then by the *detector correction* procedure described in Section 6.1.

4.1   Event Generators

> "*It is by understanding how an original physics input is tutored step-by-step in the better-controlled virtual world that an understanding can be gained of what may be going on in the real world*" [34]

The Monte Carlo event generators used in the analysis calculate the partonic cross section to leading order in α_s. The initial state includes the incoming(beam) particles and the final state is defined by the user and depends on the process under investigation. The higher order contributions are generated by the *parton shower* (PS). Different *hadronization* models are used to combine the colored partons at *parton level* to colorless(observable) particles at *hadron level*.

The structure of events in high-energy collisions is complex and not predictable from first principles. Event generators allow the problem to be subdivided into more manageable pieces, some of which can be described from first principles, while others need to be based on appropriate models with parameters tuned to data. The modeling of events relies on the factorization. The cross section and the main

37
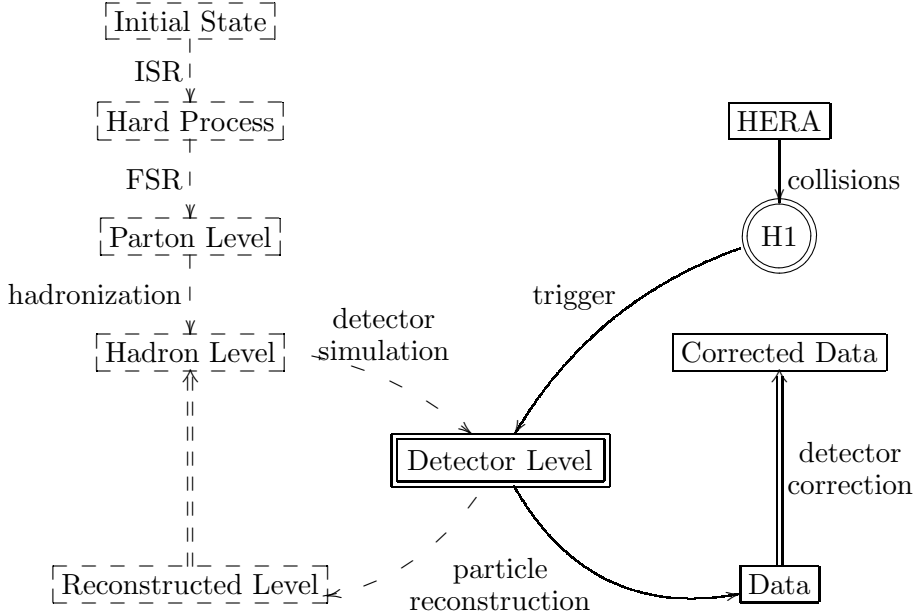
Figure 4.1: *A simplified schematic flow of the H1 event generation and detector simulation (dashed boxes and arrows) and the collected(solid boxes and arrows) H1 data with common particle reconstruction.*

structure of the event is determined by the hard partonic sub-process. The lower scale parton showers and hadronization does not influence the cross section. The **hard process matrix elements** are calculated using the Feynman rules and the parton densities of the incoming hadrons. To correct for the higher orders in α_s, the parton showers are used.

The purpose of **parton showers** is to generate real parton emissions down to a very low, but still perturbative, scales. The tree-level matrix element for n-parton state is approximated by a product of splitting functions corresponding to a sequence of one-parton emissions. At a given scale, the probability for a parton emission is the splitting function multiplied by the probability that there has been no emission above that scale. In this way, a resummation of all orders of α_s is achieved. The *initial-state radiation* (ISR) represents parton emissions before the hard scattering. It corresponds to the evolution of the parton density functions. In the backward evolution approach the generation starts with the hard sub-process. The *final-state radiation* (FSR) is simulated by time-like showers, all virtualities are positive. The maximum allowed virtuality is set by the hard-scattering process and the virtuality decreases in each subsequent branching, down to the cutoff scale which is used to regulate soft and collinear divergences. The conversion of partons to colorless particles is done according to the hadronization model.

The **hadronization** is not understood from first principles. It is a non-perturbative process and relies on different phenomenological models. The **cluster**

fragmentation[35] is the hadronization model used in the HERWIG Monte Carlo event generator. After the shower all gluons are forced to split in $q\bar{q}$ pairs. Close enough quarks form colorless *clusters* which fragment into hadrons. If a cluster is too light to decay into two hadrons, it is taken to represent the lightest single hadron of its flavour. Its mass is shifted to the appropriate value by an exchange of 4-momentum with a neighbouring cluster in the jet. Similarly, any diquark-antidiquark clusters with masses below threshold for decay into a baryon-antibaryon pair are shifted to the threshold via a transfer of 4-momentum to a neighbouring cluster. The **Lund string fragmentation**[36] is applied in the PYTHIA MC event generator. As a $q\bar{q}$ pair moves apart, the potential energy is stored in a *string*. When the energy increases, the string may break by the production of a new $q'\bar{q}'$ pair. The system splits in two color-singlet systems, $q\bar{q}'$ and $q'\bar{q}$. If the invariant mass of some of the new systems is large enough, further breaks may occur. The process repeats until there is no energy in the strings to produce new quarks. The resulting $q\bar{q}$ pairs are interpret as mesons. If unstable, they decay according to their measured branching ratios. A good representation of existing data is achieved by tuning the parameters of the models.

4.2 Pythia

PYTHIA [37] is a very popular high energy event generator. Parton showers are based on DGLAP in the collinear factorization approach. In version 6.2, used in the analysis, the initial- and final-state emissions are ordered by virtuality. It includes $q \rightarrow qg$, $g \rightarrow gg$, $g \rightarrow q\bar{q}$, $f \rightarrow f\gamma$ and $\gamma \rightarrow f\bar{f}$ processes (f stands for fermion). The initial state radiation is generated using backward evolution. The string fragmentation model is used for hadronization.

4.3 Herwig

HERWIG [38] is a general-purpose event generator for high-energy processes, with particular emphasis on the detailed simulation of QCD parton showers. The DGLAP parton showers are performed in the soft (collinear) approximation. Initial- and final-state parton showers obey angular ordering. At each branching, the angle between the two emitted partons is smaller than that of the previous branching as shown in Figure 4.2. In this way coherence effects are taken in account but emitted partons do not populate the whole phase-space. The hadronization is performed according to the cluster fragmentation model. Multiparton interactions are simulated with an external package, called JIMMY [39, 40].

4.4 Cascade

CASCADE [41] is a hadron level Monte Carlo event generator for QCD type processes with emphasis on the initial state parton evolution. The CCFM evolution equation
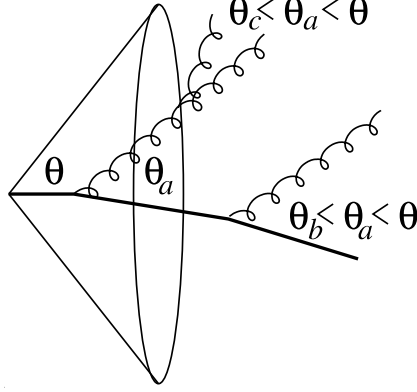
Figure 4.2: *Angular ordered parton emissions.*

is used for the initial state cascade in a backward evolution approach. According to CCFM, the emission of partons is only allowed in an angular-ordered region of phase space. The maximum allowed angle is defined by the hard scattering. The angular ordering is used also for the final state radiation. The $\gamma g \rightarrow q\bar{q}$ and $gg \rightarrow q\bar{q}$ hard sub-processes are included. The hadronization is performed using the Lund string fragmentation implemented in PYTHIA.

4.5 Monte Carlo Samples

Dedicated MC samples were generated and passed through detector simulation and reconstruction for the performed analysis. 8160002 direct and 14659999 resolved photoproduction events were generated separately with PYTHIA 6.2. Both samples have integrated luminosity of $399.94\,pb^{-1}$. The CTEQ6L[42] proton density functions and SAS-G 1D[43] photon density functions for the resolved photoproduction sample were used.

The parameter $\hat{p}_\perp$ is the transverse momentum of the hard $2 \rightarrow 2$ process, defined in the rest frame of the hard interaction. The minimum value of $\hat{p}_\perp$ is a fixed parameter in PYTHIA. In order to determine the optimal value of $\hat{p}_\perp^{min}$, an additional study has been performed. Five million resolved photoproduction MC events with a value of $\hat{p}_\perp^{min} = 1\,\text{GeV}$ were generated. $\hat{p}_\perp^{min}$ was measured for events with at least three reconstructed jets. The results are shown in Figure 4.3. The fraction of events with three reconstructed jets with $E_T > 8\,\text{GeV}$, originating from a hard process with $\hat{p}_\perp < 6\,\text{GeV}$ is below 1.5 %. Therefore $\hat{p}_\perp^{min} = 6\,\text{GeV}$ was set to gain a statistically efficient event generation.

The MC events are weighted as a function of $\hat{p}_\perp$. The weight:

$$W = \begin{cases} 1 & \hat{p}_\perp \geq \hat{p}_\perp^w \\ \frac{\hat{p}_\perp^w}{\hat{p}_\perp} & \hat{p}_\perp < \hat{p}_\perp^w \end{cases}, \tag{4.1}$$

where $\hat{p}_\perp^w = 7.75\,\text{GeV}$ is the value of $\hat{p}_\perp$, below which the events are weighted.
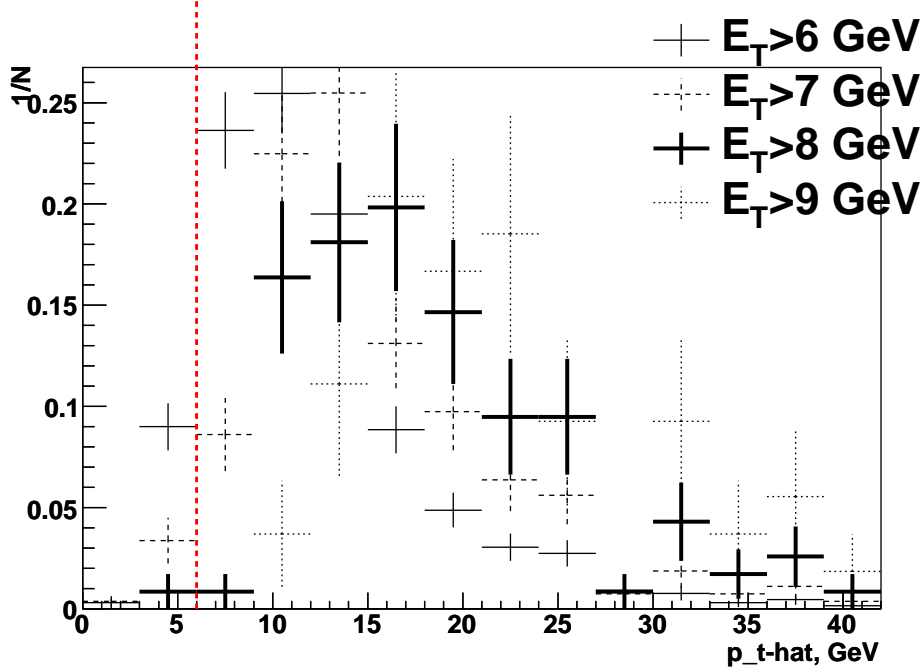
Figure 4.3: *The transverse momentum of the hard $2 \rightarrow 2$ process, $\hat{p}_{\perp}$, for events with at least three reconstructed jets. The normalized $\hat{p}_{\perp}$ distribution is shown for different values of the minimum transverse energy of the jets.*

By this weighting more events in the range of the measured data are generated. The minimum transverse momentum for multiple interactions is set to 1.4 GeV.

Several Monte Carlo samples are generated for comparison to the corrected data. The CTEQ6L[44] proton density functions are used with PYTHIA and HERWIG. For the resolved photon, SAS-G 1D[45] and GRV-G LO[46] photon density functions are used. Two CASCADE samples with different gluon density are generated in addition. A summary of the generated Monte Carlo samples with the corresponding number of events and the calculated cross section is given in Table 4.1. For the DGLAP based Monte Carlo samples, the direct and resolved photoproduction are generated separately. In order to compare to the measured data, the direct and resolved samples are added by luminosity.

Table 4.1: *Generator level Monte Carlo samples*

Generator	Mode	MI	photon pdf	proton pdf	Events	σ,nb
Cascade	direct			Gluon setA	2000000	24.255
1.2	direct			Gluon setB	2000000	20.789
Herwig	direct			CTEQ6L	2000000	20.121
6.5	resolved	no	SAS-G 1D	CTEQ6L	4614899	40.461
(Jimmy 4.1)	resolved	yes	SAS-G 1D	CTEQ6L	4000000	40.470
Pythia	direct			CTEQ6L	8160000	20.401
6.2	resolved	no	SAS-G 1D	CTEQ6L	3000000	36.662
	resolved	yes	SAS-G 1D	CTEQ6L	14660000	36.655
	resolved	yes	SAS-G 1D	CTEQ6L	1000000	36.145
	resolved	no	GRV-G LO	CTEQ6L	3000000	44.877
	resolved	yes	GRV-G LO	CTEQ6L	3000000	44.894

Chapter 5

Event Selection

This chapter is dedicated to the selection of the data. The analysis is based on the data collected during the first part of 2006. In this running period electrons were accelerated. For each event it is required that the detector was in appropriate conditions to measure all event properties important for the analysis. This includes the status of the subdetector systems. Table 5.1 contains a list of the detector components with high voltage required to be on with the main purpose of each detector subsystem. The detector components are described in Chapter 2.

With this requirement the data integrated luminosity is estimated to be $50813 \, \text{nb}^{-1}$. In Figure 5.1 the integrated luminosity is shown as a function on the **H1** run number.

In this chapter the selection of photoproduction events is discussed separately from the jet selection. Three independent data samples are analyzed, namely dijet, trijet and fourjet samples. In addition the trigger efficiency and non-ep background studies are presented.

For comparison with the Monte Carlo the data must be corrected for the trigger efficiency. The correction of the Monte Carlo for the z-vertex is done because this distribution is not simulated. Furthermore, the MC samples are reweighted to

Table 5.1: *Detector components required for the analysis*

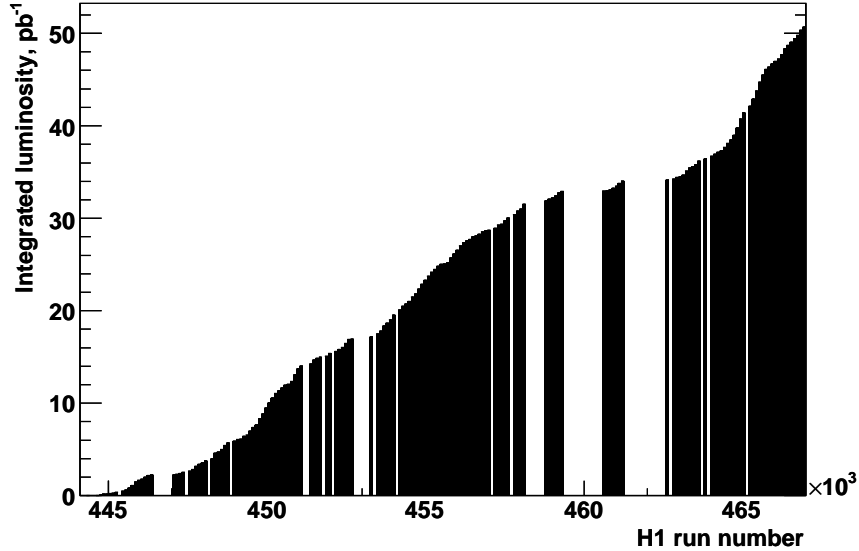|	
CIP	vetoes on non-ep interactions by z-vertex requirement
COZ	provides better z-coordinate resolution
CJC	charged particle tracks reconstruction
LAr	particle energy reconstruction, electron veto
SPACAL	electron veto
TOF	non-ep veto
LUMI	measures luminosity

Figure 5.1: *H1 delivered luminosity for 2006 e$^-$ period. The analysis is based on the data with integrated luminosity of more than 50 pb^{-1}.*

describe the angular distributions of the jets.

5.1   Photoproduction Selection

The photoproduction event class covers events with small virtuality, Q^2, in which the scattered electron escapes undetected under small scattering angle. Therefore, for the photoproduction selection, it is required that there was no electron identified in the LAr calorimeter or SPACAL. The equivalent condition on particle level depends on the maximum polar angle acceptance of the SPACAL and corresponds to $Q^2 < 4\,\mathrm{GeV}$.

5.2   Background Rejection

The photoproduction selection does not ensure that the selected events originate from ep collisions. Several **H1** topological background finder algorithms are used to remove the non-ep background. A detailed documentation of available non-ep background finders is available from[47]. The results are shown in Figure 5.2. Bin -1 corresponds to events not classified as background by any of the finders. Only a small fraction of events are recognized as background. The conclusion is that the finders are not able to identify the background events in the data sample.

Instead, the fraction of the non-ep events is measured using the proton pilot bunches. A proton pilot bunch is a bunch with no associated electron bunch. Hence,
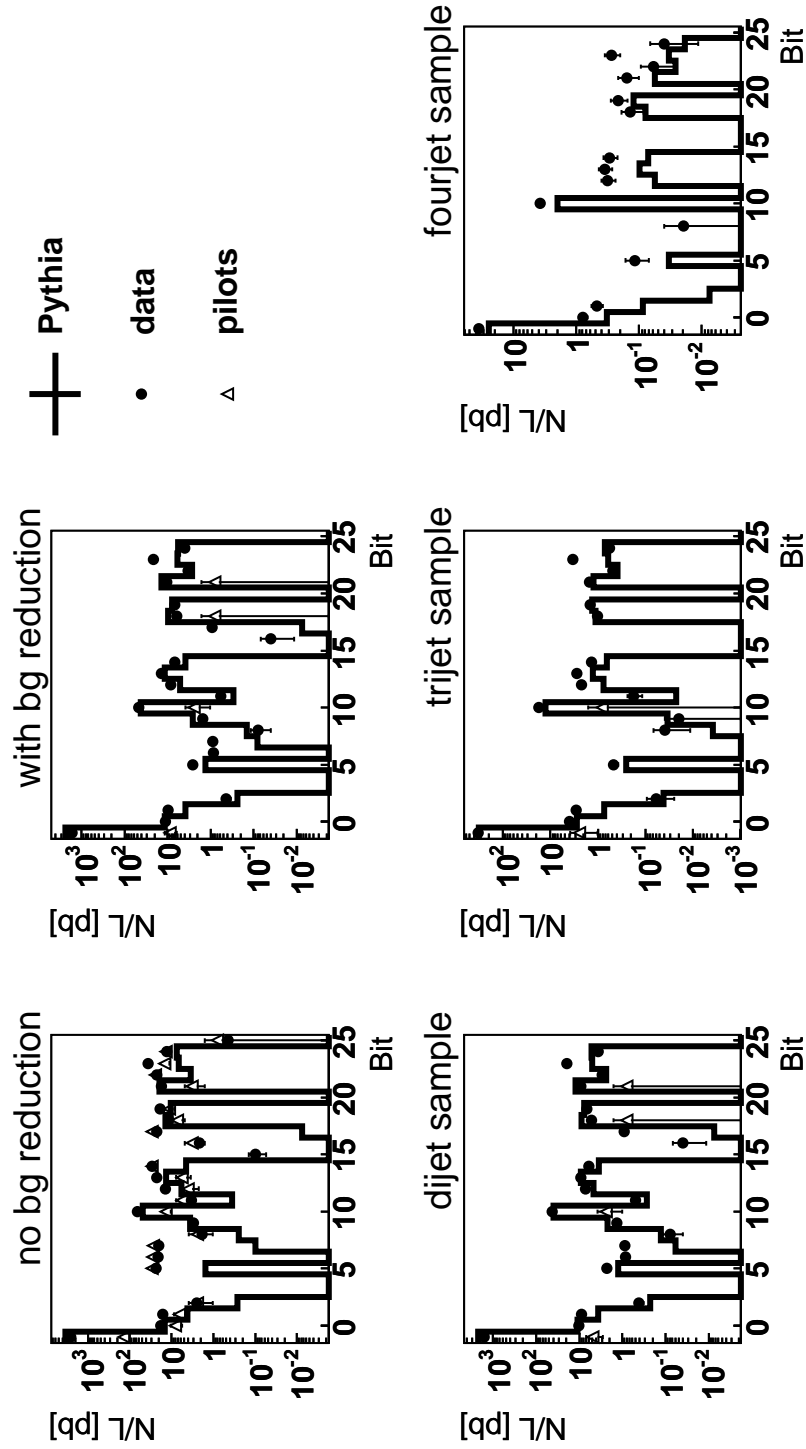
Figure 5.2: *The background finder bits. "no bg reduction" stands for events with at least two jets of transverse energy greater than 9 GeV. For the plot labeled "with bg reduction", the cuts from Table 5.2 are applied. The plots for the dijet, trijet and fourjet samples include the corresponding cut on the invariant mass of the jet system.*

only interactions between the proton and the beam pipe or gas molecules in the beam pipe could occur. It is assumed that this type of events will also occur for colliding bunches, i.e. for paired proton and electron bunches. HERA has a maximum of 220 bunches. The bunch type could be:

0. no bunches

1. proton pilot bunch

2. electron pilot bunch

3. colliding bunch

Around 10 % of the events originating from non-colliding bunches are not rejected by the trigger for background studies. The number of data events as a function of the bunch type is shown in Figure 5.3 (a). For the correct estimation of the background fraction, it is necessary to normalize the proton plot bunch distributions to the ratio of the colliding bunch current to the proton pilot bunch current. The proton current in the colliding and proton pilot bunches is shown in Figure 5.3 (b) and (c). There are two possibilities if this fraction is not below the accepted level (around 1%). One option is to subtract statistically this events from the measured cross section. In the analysis, this method is not preferred because it measures the properties of selected events which would be lost after a statistical subtraction. Another approach is to find an appropriate observable which isolates the non-ep events in some part of the observable distribution. A dedicated cut on this observable excludes the background events from the analysis. Often, the t_0 time from the CJC or the LAr calorimeter is appropriate observable. Unfortunately, as shown in Figure 5.3, the signal and the background have the same structure as a function of t_0.

The background is reduced to less than 1 % of the selected events during the event and jet selection. There is a lists of the event selection variables and cut values in Table 5.2.

- The z-vertex is the position of the interaction point along the beam axis as estimated from the event tracks. The measured and simulated z-vertex distributions with the estimated background are shown in Figure 5.4. The spectrum of the non-ep background is flat because there is no privileged position for the proton-beam gas interactions. The regions where the signal/background ratio is close to 1 are cut away. This corresponds to -25 < z-vertex < 25 cm.

- The missing transverse momentum, $p_{T,miss}$, is calculated as

$$p_{T,miss} = \sqrt{(\sum_i p_{x,i})^2 + (\sum_i p_{y,i})^2}. \tag{5.1}$$

  The summation is performed over all *hadronic final state* (HFS) particles. The HFS includes all reconstructed particles except the scattered electron. The
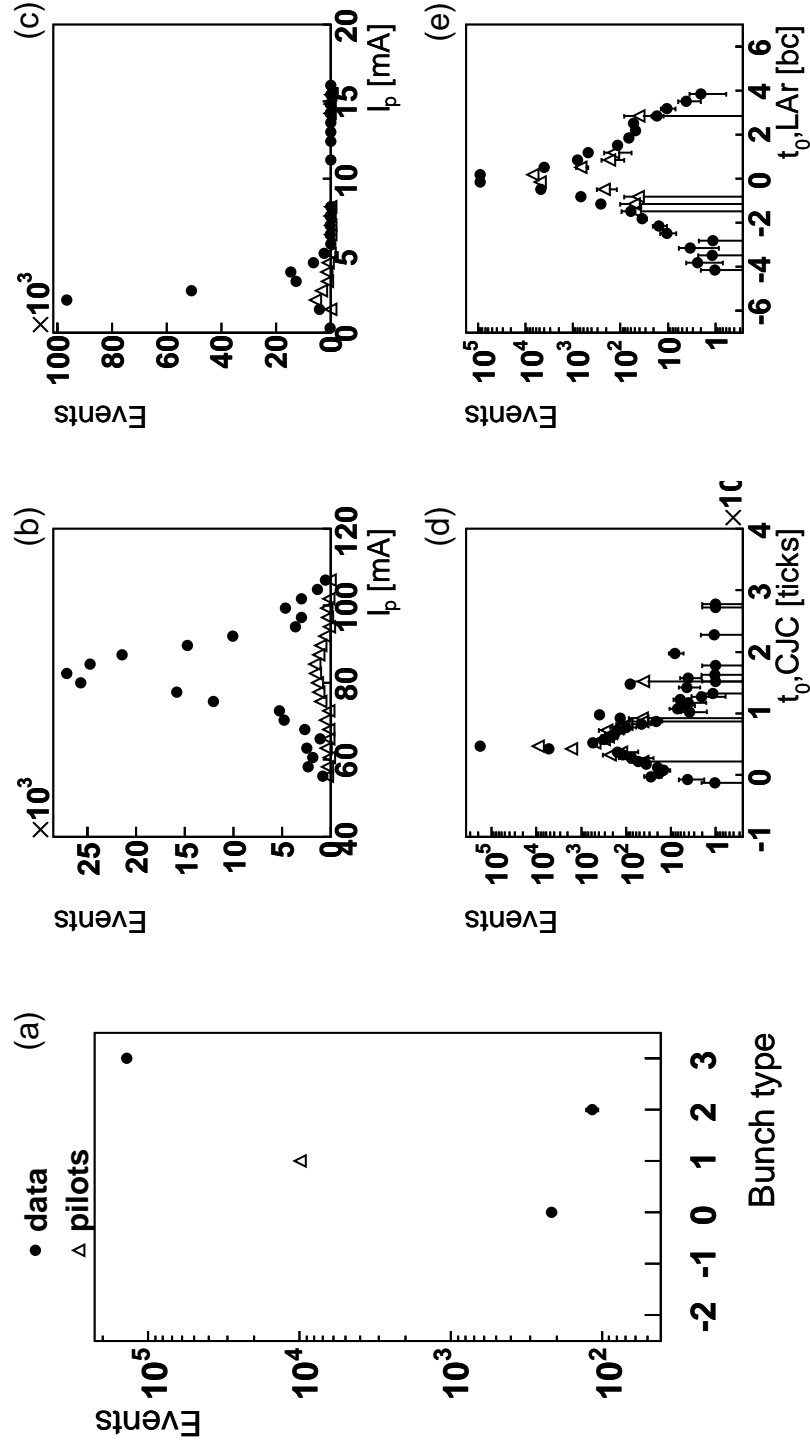
Figure 5.3: The bunch type (a), the proton current for (b) colliding and (c) proton pilot bunches and the t_0 time from (d) CJC and (e) LAr. The full circles represent the data while the open triangles show the number of events originating from the proton pilot bunches, normalized to the ratio of the pilot to the colliding bunches.

Table 5.2: *Event selection cuts*

-25 $< z$-vertex $< 25\,$cm

$0.3 < y_{JB} < 0.9$

$p_{T,miss} < 2\sqrt{E_{T,sum}}$

word hadronic is misleading. Leptons and photons could also be a HFS particles. The cut,

$$p_{T,miss} < 2\sqrt{E_{T,sum}}, \tag{5.2}$$

where $E_{T,sum}$ is the scalar sum of the transverse energy of the accepted jets in the event, removes charge current, cosmic and halo-muon events, as shown in Figure 5.5.

- The scattered electron is not detected in tagged photoproduction. In this case, y is reconstructed from the HFS, using the Jacquet-Blondel[48] method:

$$y_{JB} = \frac{1}{2E_e} \sum_i (E_i - p_{z,i}), \tag{5.3}$$

where the sum is over all particles in the HFS and E_e is the electron beam energy. The measured distribution of y_{JB} is shown in Figure 5.6. The non-ep background, as estimated from the proton pilot events, increases at low values of y_{JB}. In these events, the activity is concentrated in the forward part of the detector. A minimum value requirement for the y_{JB} value rejects the big fraction of the background. The maximum value requirement reduces the background from DIS events in which the scattered electron was not reconstructed. The rest of the non-ep background is rejected by the invariant mass of the jet system as it will be discussed in Section 5.4.

5.3   Trigger Studies

5.3.1   Analysis Subtriggers

There are no subtriggers designed to identify multijet events in the **H1** trigger setup. Therefore the identification of the subtriggers sensitive to photoproduction events with jets is necessary. For this study, the event selection for the dijet, trijet and fourjet scenario is done without trigger requirements and the subtrigger rates are measured. The significance of a subtrigger is proportional to its L2/3 actual verified rate (trigger rates are described in detail in Section 3.2). The results are shown in Figure 5.7. According to the rates, the subtriggers s76 and s74 were identified as appropriate for the analysis. Both subtriggers are not prescaled at L1. The exact definitions of the trigger elements of the subtriggers used in the analysis are shown in Table 5.3.
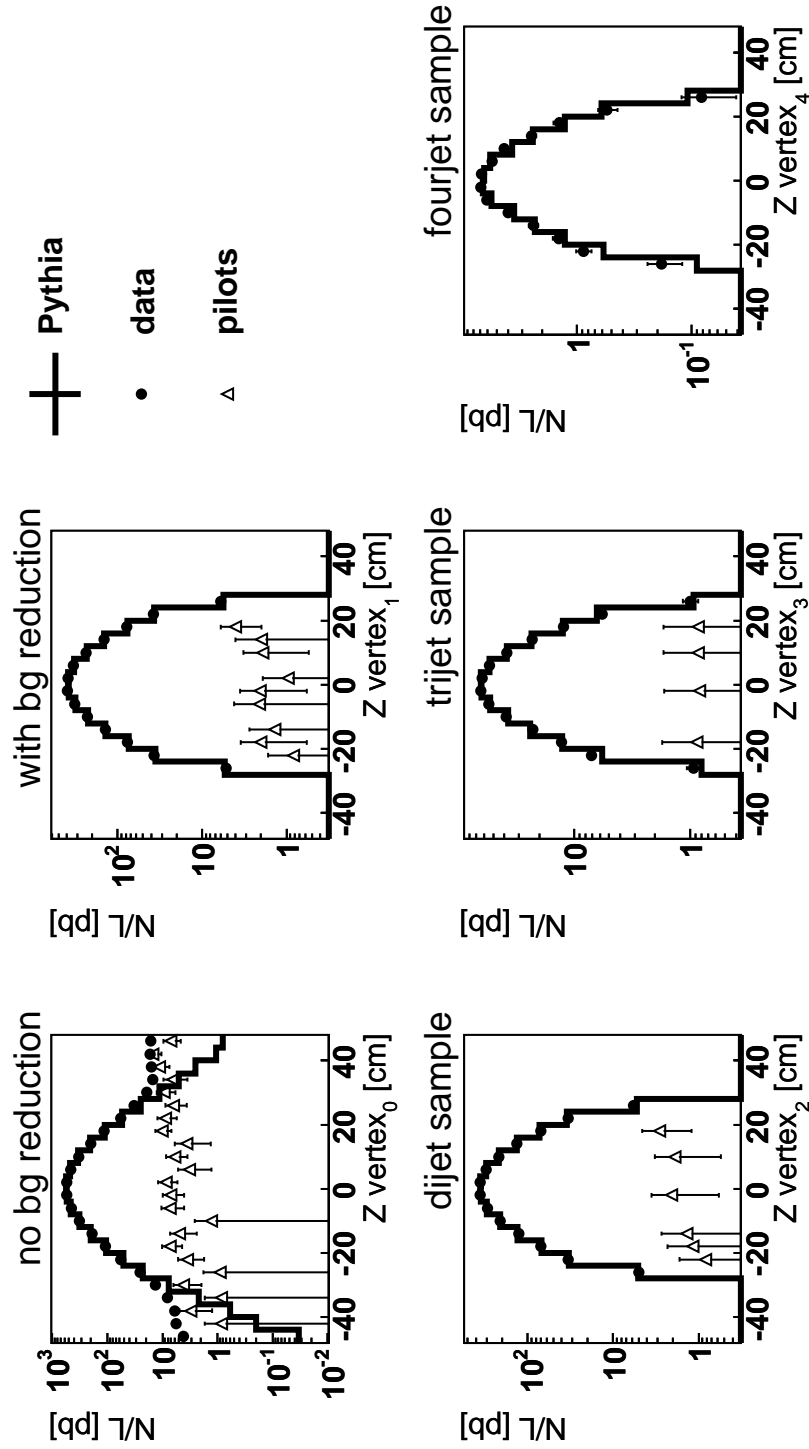
Figure 5.4: *The z-vertex reconstructed level distributions. "no bg reduction" stands for events with at least two jets of transverse energy greater than 9 GeV. For the plot labeled "with bg reduction", the cuts from Table 5.2 are applied. The plots for the dijet, trijet and fourjet samples include the corresponding cut on the invariant mass of the jet system.*
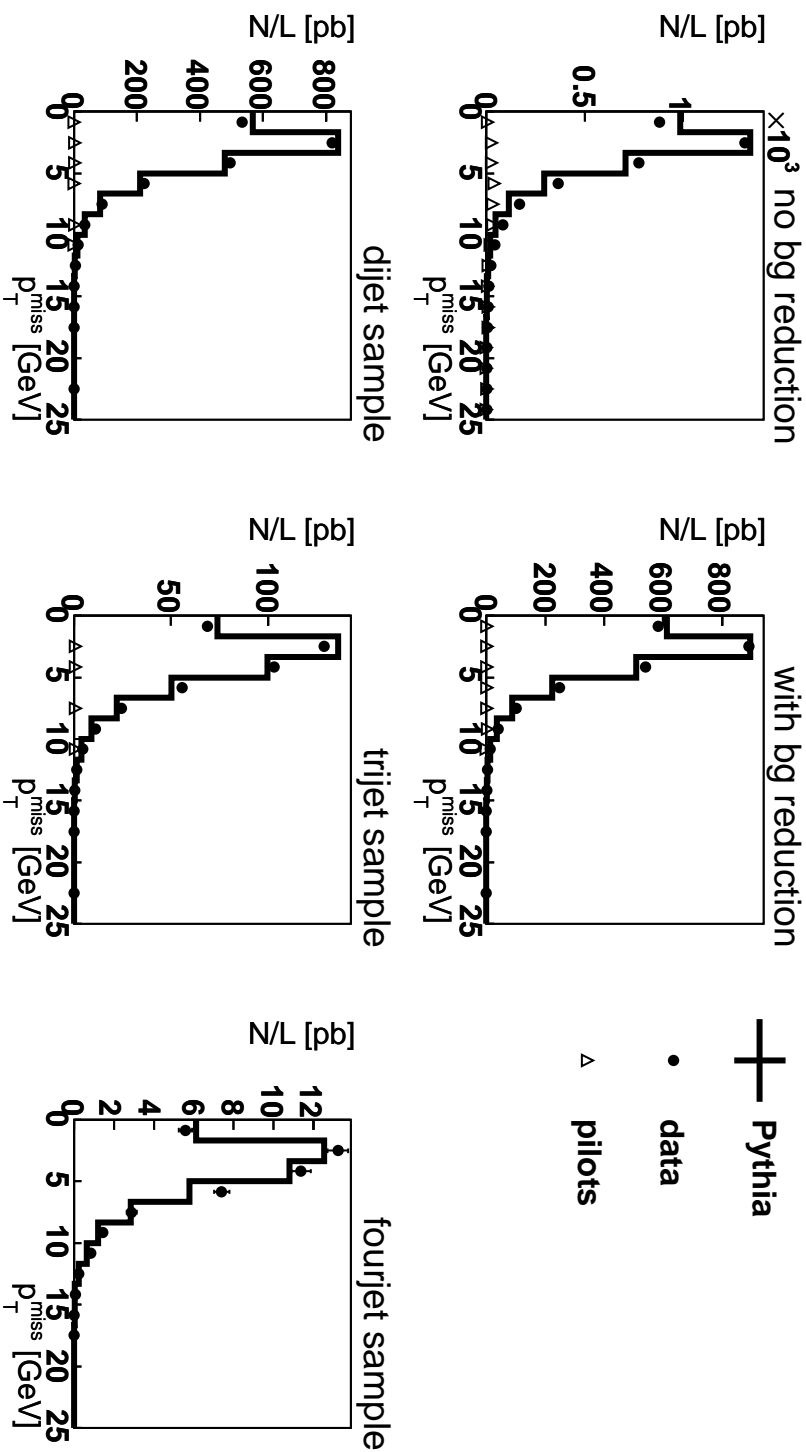
Figure 5.5: *The* $E_{T, miss}$ *reconstructed level distributions. "no bg reduction" stands for events with at least two jets of transverse energy greater than 9 GeV. For the plot labeled "with bg reduction", the cuts from Table 5.2 are applied. The plots for the dijet, trijet and fourjet samples include the corresponding cut on the invariant mass of the jet system.*

Figure 5.6: *The y_{JB} reconstructed level distributions. "no bg reduction" stands for events with at least two jets of transverse energy greater than 9 GeV. For the plot labeled "with bg reduction", the cuts from Table 5.2 are applied. The plots for the dijet, trijet and fourjet samples include the corresponding cut on the invariant mass of the jet system.*

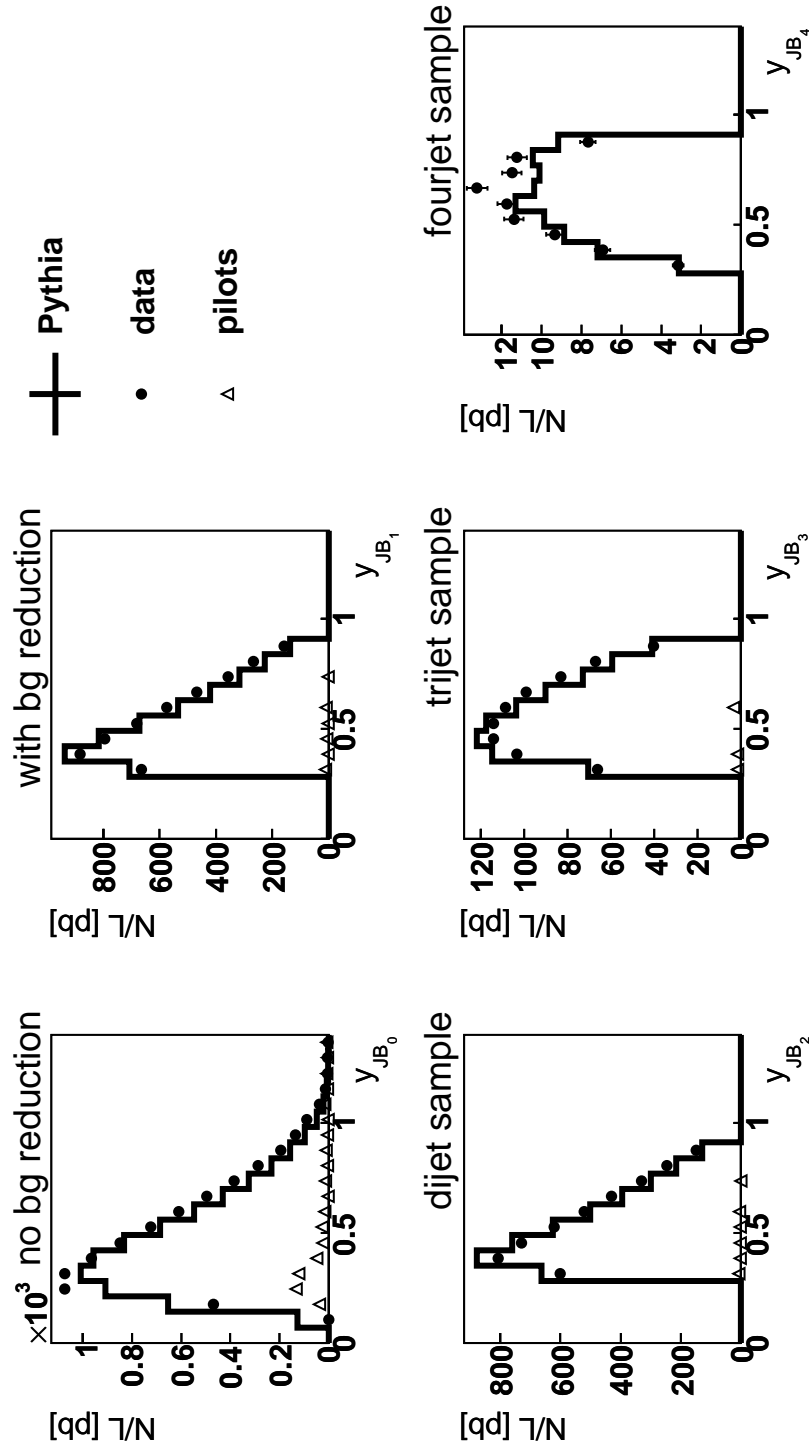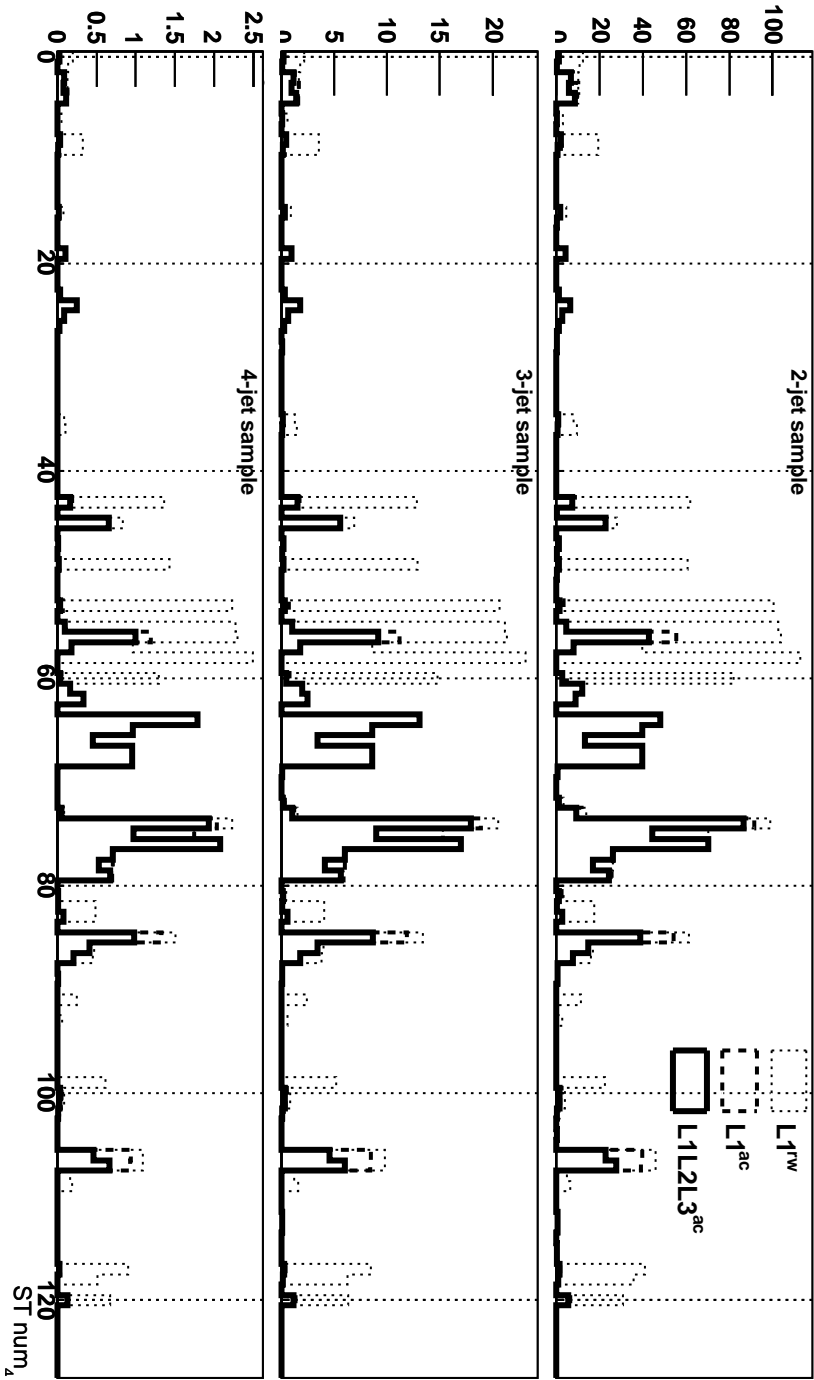Figure 5.7: *The subtrigger rates for different jet scenarios. The L1 raw rates are represented by dots, the actual L1 rates by dashed line and the L2/L3 verified subtrigger rates by solid line. The solid line peaks correspond to subtriggers sensitive to the analyzed events.*

Table 5.3: *Trigger definitions*

ST	TE	Definition	Comment
s2	L1[043]	SPCLe_IET > 2	Electron in SPACAL
	L2TT[022]	SPCL_R20	SPACAL radius > 20 cm
s74	L1[096]	LAr_EW > 1	Sum over all BT weighted by profile
	L1[110]	FTT_mul_Tc > 1	At least two tracks with momentum greater than 400 MeV
	L2NN[010]	DiJets_untagged	Neural network with inputs from CIP, FTT, LAr
s76	L1[100]	LAr_Etrans > 1	Sum over all BT weighted by $\sin\theta$

Table 5.4: *Number of triggered events by the analysis subtriggers, their overlap and events, not triggered by any of them.*

sample	s76	s74	overlap	not triggered
dijet	80525	80461	65164	10538
trijet	23077	21450	18334	2480
fourjet	3721	3180	2768	420

To fully understand the trigger, the overlap between the subtriggers has to be considered. The number of events triggered by s76, s74, their overlap and not triggered events are shown in Table 5.4. The non triggered events are events which pass the event selection but are not triggered by the analysis subtriggers.

To make sure that the selected events are not downscaled on level 4, the L4 event class is measured as shown in Figure 5.8. It shows that there are not downscaled events in the selection. The next step is to calculate the trigger efficiency.

5.3.2 Trigger Efficiency

The trigger efficiency is extracted from the data, according to

$$\epsilon = \frac{N((L1L2_{74}^{raw} \vee L1_{76}^{raw}) \wedge L1L2L3_2^{ac})}{N(L1L2L3_2^{ac})}. \tag{5.4}$$

The reference subtrigger, s2, is based on energy deposit in SPACAL and has no common TE's with the analysis subtriggers. The trigger efficiency calculation basics are discussed in Section 3.4. For this calculation the photoproduction selection, described in Section 5.1, is not applied to keep the events with electron in the SPACAL for the reference subtrigger. The efficiency is measured as a function of the transverse energy, E_T, and pseudorapidity, η, of the jets with the highest and the second E_T, indexed as 1 and 2, and as a function of y_{JB}.

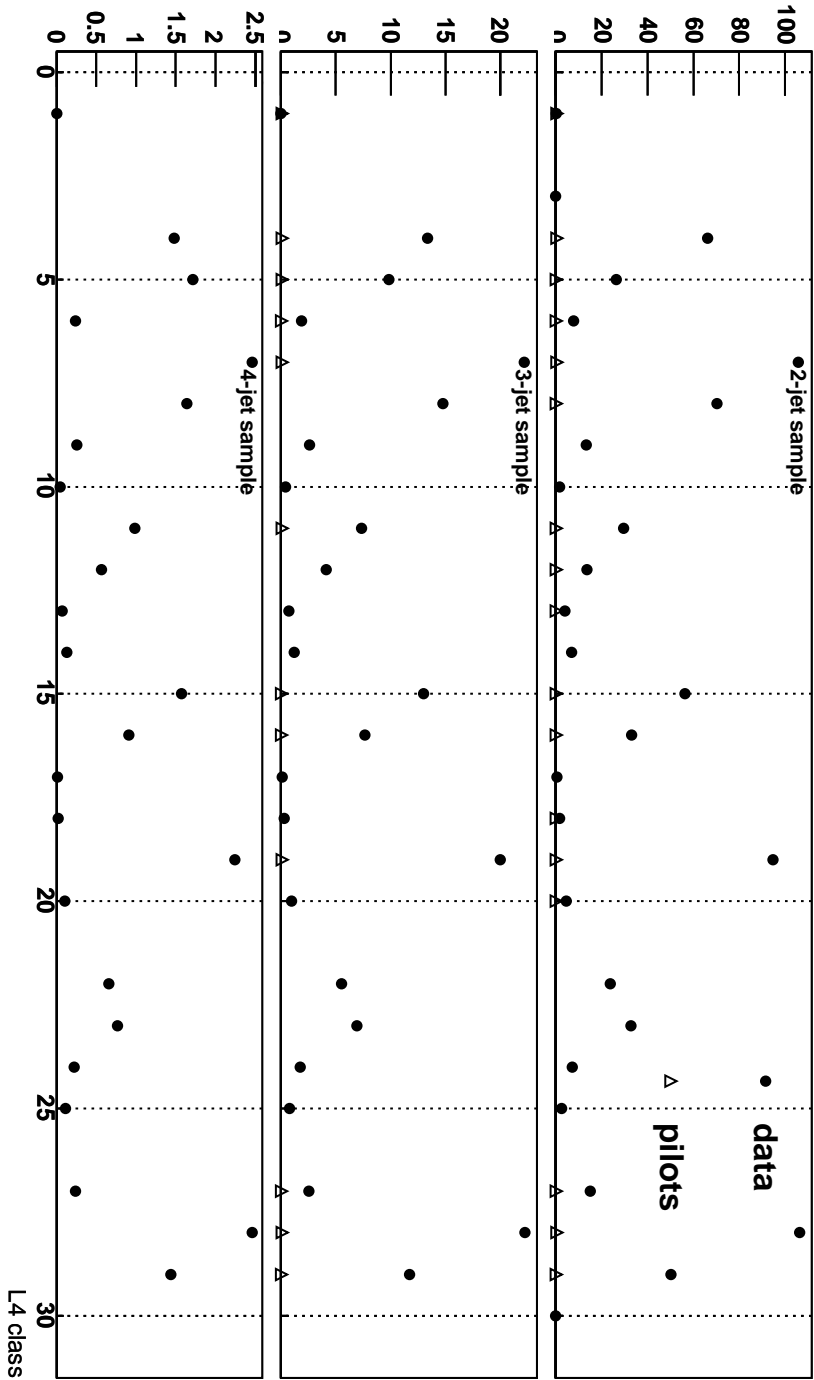Figure 5.8: *Trigger level 4 rates (arbitrary units) of the selected events for the dijet, trijet and fourjet scenario. The definitions of the trigger level 4 classes are given in Table 3.2.*
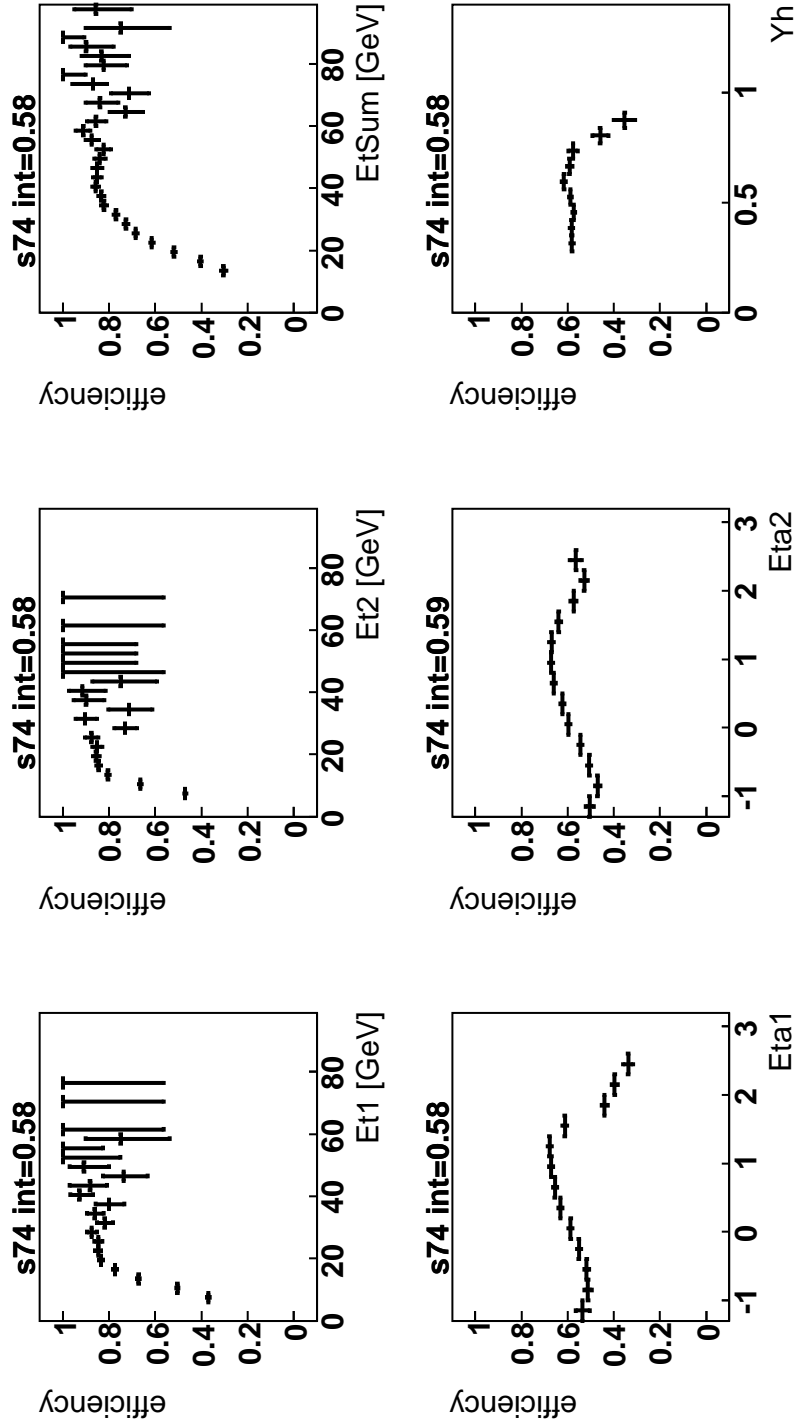
Figure 5.9: *The L1 efficiency of s74 as a function of various observables. The integrated efficiency is shown above the plots. It should not depend on the observable. Differences are caused by numerical inaccuracies.*

Table 5.5: *Trigger efficiency fit*

parameter	meaning	value	error
ϵ_{max}	the maximum efficiency	9.73746e-01	7.16162e-03
k	exponential factor	-1.55165e-01	2.28650e-02
E_{min}	energy threshold	1.53057e+01	1.62752e+00

The efficiency of s74 is shown in Figure 5.9. The drop in the efficiency as a function of the leading and second jet rapidity at 1.5 is explained by the geometry of the CJC. This determines the maximum rapidity of the two highest E_T jets. The s74 L2 efficiency after this requirement is shown in Figure 5.10 and Figure 5.11 shows the efficiency of s76. The total efficiency of s76 is 58 %, the efficiency of s74 is 72 % and the combined total efficiency is 78 %.

5.3.3   Trigger Efficiency Correction

The combined efficiency of s76 and s74 is shown in Figure 5.12. Details about the error of the efficiency calculation method are available in[49].

The efficiency does not depend on any of the measured jet observables but the energy of jets. This follows by the analysis subtrigger definitions(Table 5.3). Both s74 and s76 trigger on energy deposits in the LAr. The track requirement in the definition of s74 should be angle independent as long as the measured jets are in the CJC acceptance. The jet observable that corresponds best to the energy sum measured in the detector is the sum of the transverse energies of the accepted jets. The combined s74 and s76 efficiency as a function of that sum is fit to the function:

$$\epsilon(E) = \epsilon_{max} - e^{k(E-E_{min})}, \tag{5.5}$$

The fit and the parameter values are shown in Figure 5.12 and Table 5.5. Technically, the correction is done by assigning a weight factor $\frac{1}{\epsilon(E_{T,1})}$ to the data events. A reliable method to test the applicability of the correction is the measurement of the trigger efficiency for the weighted events. This is shown in Figure 5.12 where the corrected efficiency is marked with open triangles. The effect of the correction as a function of the $\sum E_T$ on the efficiency as a function of the other jet variables is visible. The efficiency as a function of the jet pseudorapidity is flat after the correction.

5.4   Jet Selection

The jet selection requirements are summarized in Table 5.6. For all jets, the minimum pseudorapidity of -0.5 guarantees that the jet is fully in the acceptance of the LAr calorimeter. The maximum $\eta_{1,2} = 1.5$ ensures that the two highest transverse energy jets are in the acceptance of CJC(FTT). For the dijet sample at least two jets with $E_T > 9\,\text{GeV}$ are required. For the trijet and fourjet samples, at least one and two
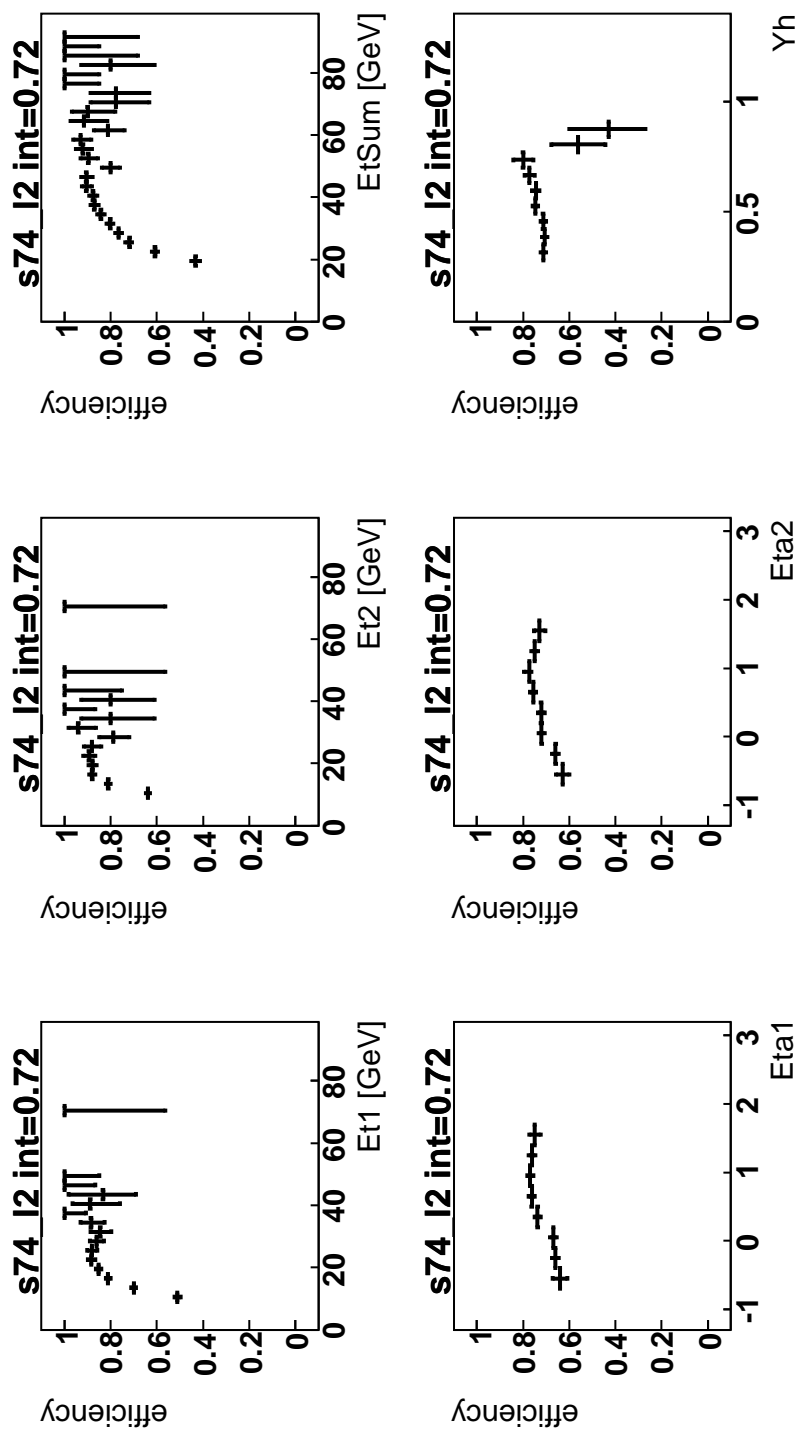
Figure 5.10: *The L2 efficiency of s74 as a function of various observables.*

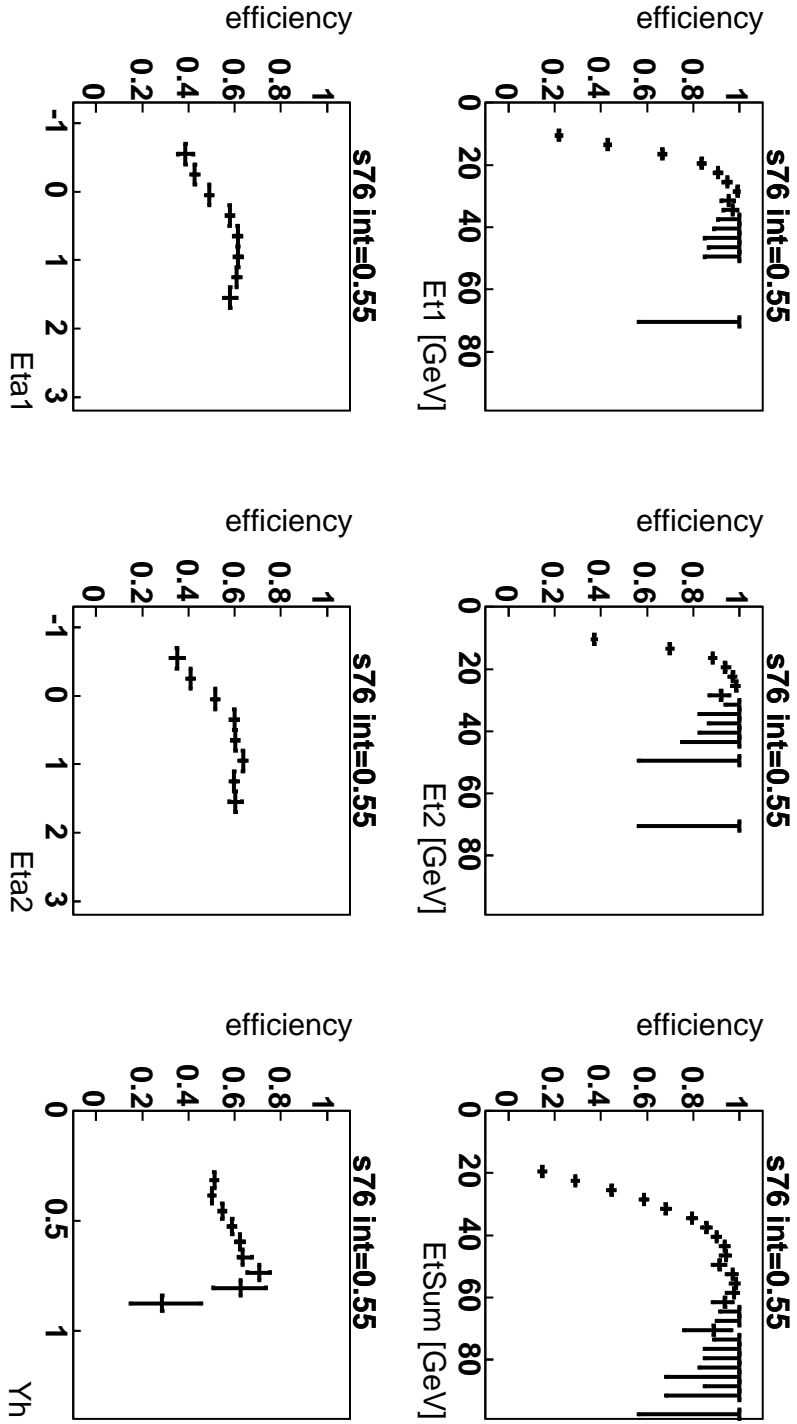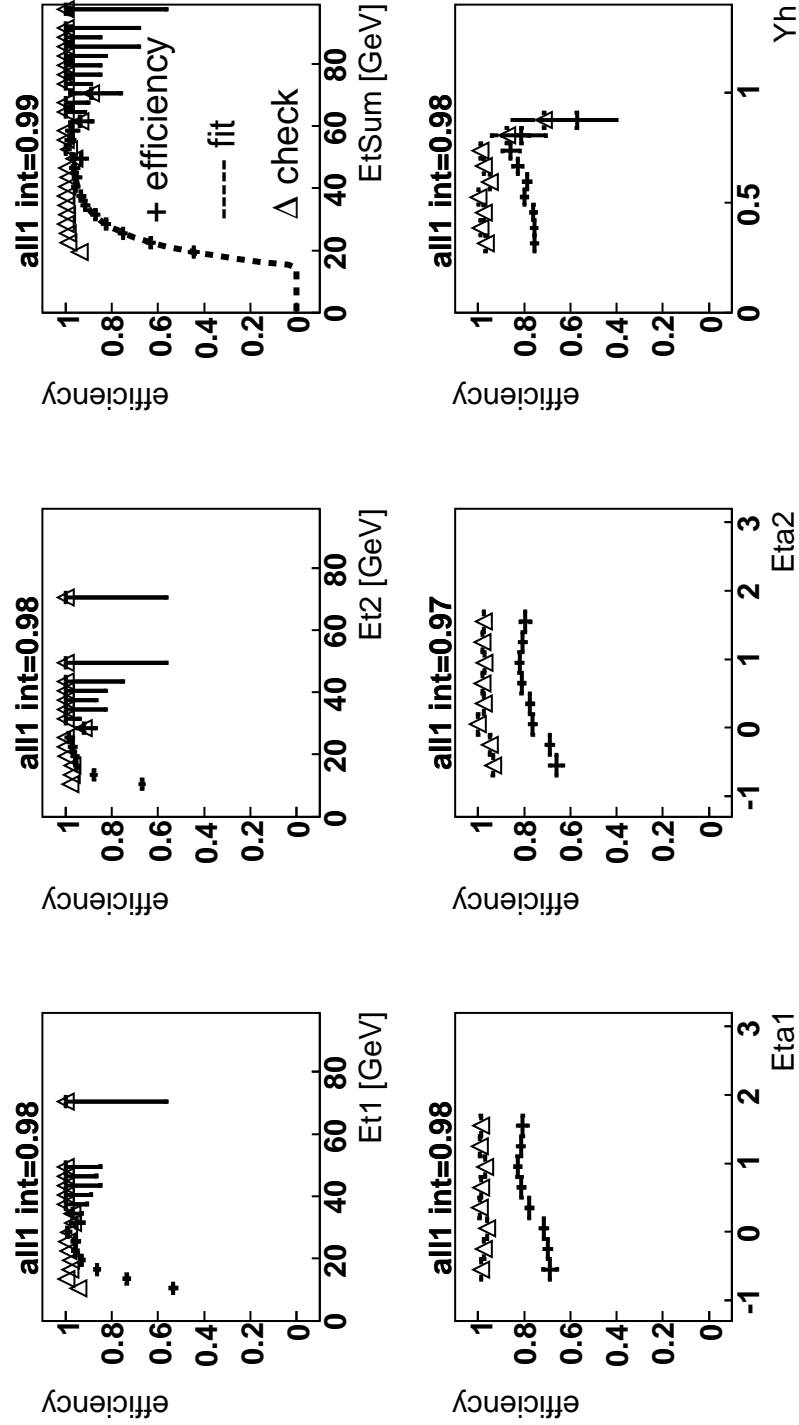Figure 5.11: *The L1 efficiency of s76 as a function of various observables.*

Figure 5.12: *The combined trigger efficiency as a function of various observables. The check of the correction for the trigger efficiency is shown with open triangles. The integrated efficiency after the trigger correction is shown above the plots. It should not depend on the observable. Differences are caused by numerical inaccuracies.*

Table 5.6: *Jet selection*

$$-0.5 < \eta_{1,2} < 1.5$$
$$E_{T,1,2} > 9 \,\text{GeV}$$
$$-0.5 < \eta_{3,4} < 2.5$$
$$E_{T,3,4} > 6 \,\text{GeV}$$
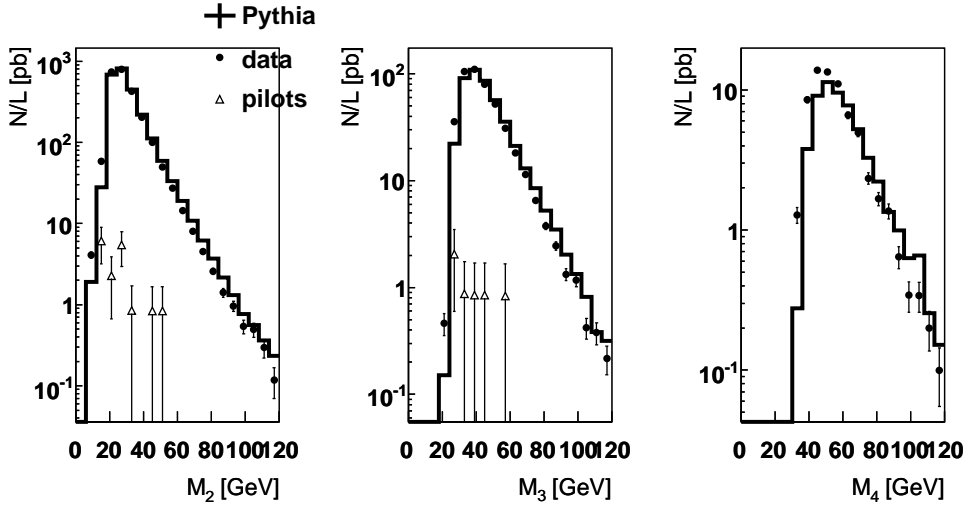
Figure 5.13: *The jet system invariant mass, from left to right, for the dijet, trijet and fourjet sample.*

additional jets with $E_T > 6\,\text{GeV}$ and $\eta_{3,4} < 2.5$ are required. The pseudorapidity of the third and fourth jets is allowed to be outside CJC acceptance because the trigger efficiency is already defined by the two hardest jets.

The invariant mass of the n-jet system is calculated from the sum of their four-momenta, p_i, as

$$M_{nj} = \sqrt{\left(\sum_{i=1}^{n_{jets}} p_i\right)^2}. \tag{5.6}$$

The fraction of background events is controlled with the help of the events originating from proton pilot bunches. The non-ep event fraction is significant for low values of the jet system invariant mass. To reduce the non-ep background below $1\,\%$, a minimum invariant mass of the jet system is required as shown in Figure 5.13. The minimum values are summarized in Table 5.7.

Table 5.7: *Invariant mass cuts*

$$M_{2j} > 20\,\text{GeV}$$
$$M_{3j} > 30\,\text{GeV}$$
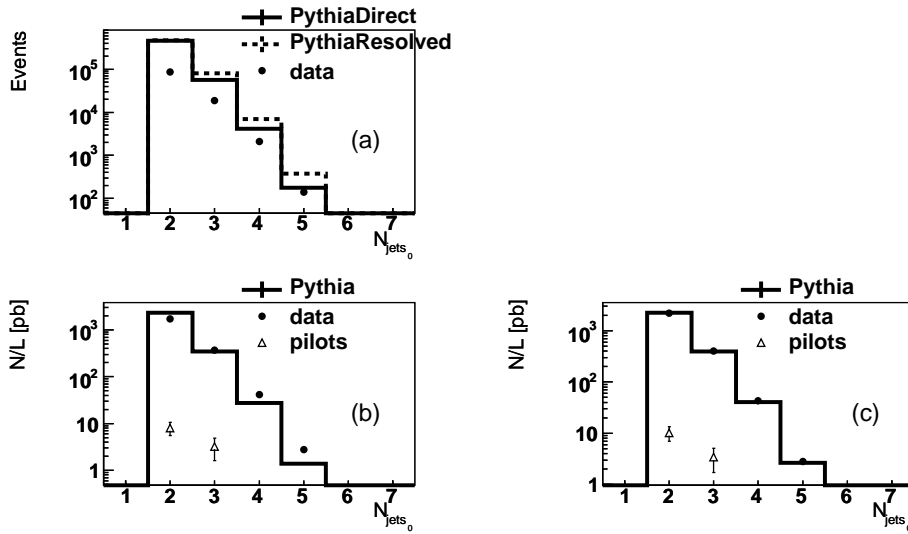$$M_{4j} > 45\,\text{GeV}$$

Figure 5.14: *The jet multiplicity; (a) the number of data events compared to the number of events generated with PYTHIA direct and PYTHIA resolved, (b) the data compared to the combined PYTHIA and (c) the same plot after scaling (see text). The events from the non-ep background are shown with open triangles. They are well under 1 % of the data.*

Table 5.8: *Number of selected events*

sample	data	PYTHIA (direct)	PYTHIA (resolved)
dijet	83945	232697	294168
trijet	23399	37291	64498
fourjet	3848	2830	6569

5.5 Control Plots

Data and MC distributions in reconstructed level are compared for the dijet, trijet and fourjet samples. On the following plots, the data is corrected for trigger efficiency.

Compared to the data events, four times more statistics were generated with both direct and resolved PYTHIA as shown in Figure 5.14 (a). The histogram shows the jet

Table 5.9: *Monte Carlo scaling factors*

generator	PYTHIA	HERWIG	CASCADE
integrated	1.4	1.9	1.9
dijet	0.962	0.942	1.07
trijet	1.61	2.54	0.61
fourjet	3.44	4.3	0.524
fivejet	9.74	3.39	0.515

multiplicity. The exact number of selected data and MC events is shown in Table 5.8. The direct and resolved samples are added by their luminosity and compared to the data in Figure 5.14 (b) where the distributions are normalized to the luminosity. PYTHIA underestimates the magnitude of the measured cross sections for the tri- and fourjet samples. To compare with the shape of the measured distributions, the MC predictions are scaled by a factor required to describe the magnitude of the data cross sections. The scaling factors are extracted after the MC direct and resolved samples were added by luminosity. The correction does not affect the ratio between the direct and resolved contribution. The scaling factors are shown in Table 5.9. For each MC generator, a *global* factor is extracted to account for the overall cross section as well as additional factors for each jet multiplicity. The effect of the scaling is shown in Figure 5.14 (c) for the combined PYTHIA sample, normalized to luminosity. The non-ep background, as estimated from the proton pilot bunches, is also shown in the luminosity normalized histograms. It is always below $1\,\%$ of the data.

5.5.1   Reweighting the Z-vertex distribution

The distributions of the event vertex is a HERA property. On hadron(particle) level it is set to zero. During the detector simulation, the events get a vertex location. In general, the vertex distribution differs for reconstructed data and MC. The weight as a function of the z-coordinate of the vertex location is a fit to the ratio of the data to the MC sample at reconstructed level. The effect of the reweighting is shown in Figure 5.15. For all data samples, the fit extracted from the dijet sample is used as the z-vertex distribution should be independent of the number of jets.

5.5.2   Reweighting The Jets

The jets are ordered in E_T and called first, second, third and forth jet such as $E_{T_1} > E_{T_2} > E_{T_3} > E_{T_4}$. After the correction for the trigger efficiency, the E_T of the jets is in a very good agreement with PYTHIA as shown in Figure 5.16. However, the pseudorapidity of the jets is not well described as seen in Figure 5.17. To improve this, the MC sample has been weighted as a function of the sum and the difference of the first and second jet, $\eta_1 + \eta_2$ and $\eta_1 - \eta_2$. The trijet sample is weighted in addition for $\eta_1 + \eta_3$ and $\eta_1 - \eta_3$ and for the fourjet sample also reweighting in $\eta_2 + \eta_4$ and $\eta_2 - \eta_4$ is necessary to achieve good agreement between the data and the MC.
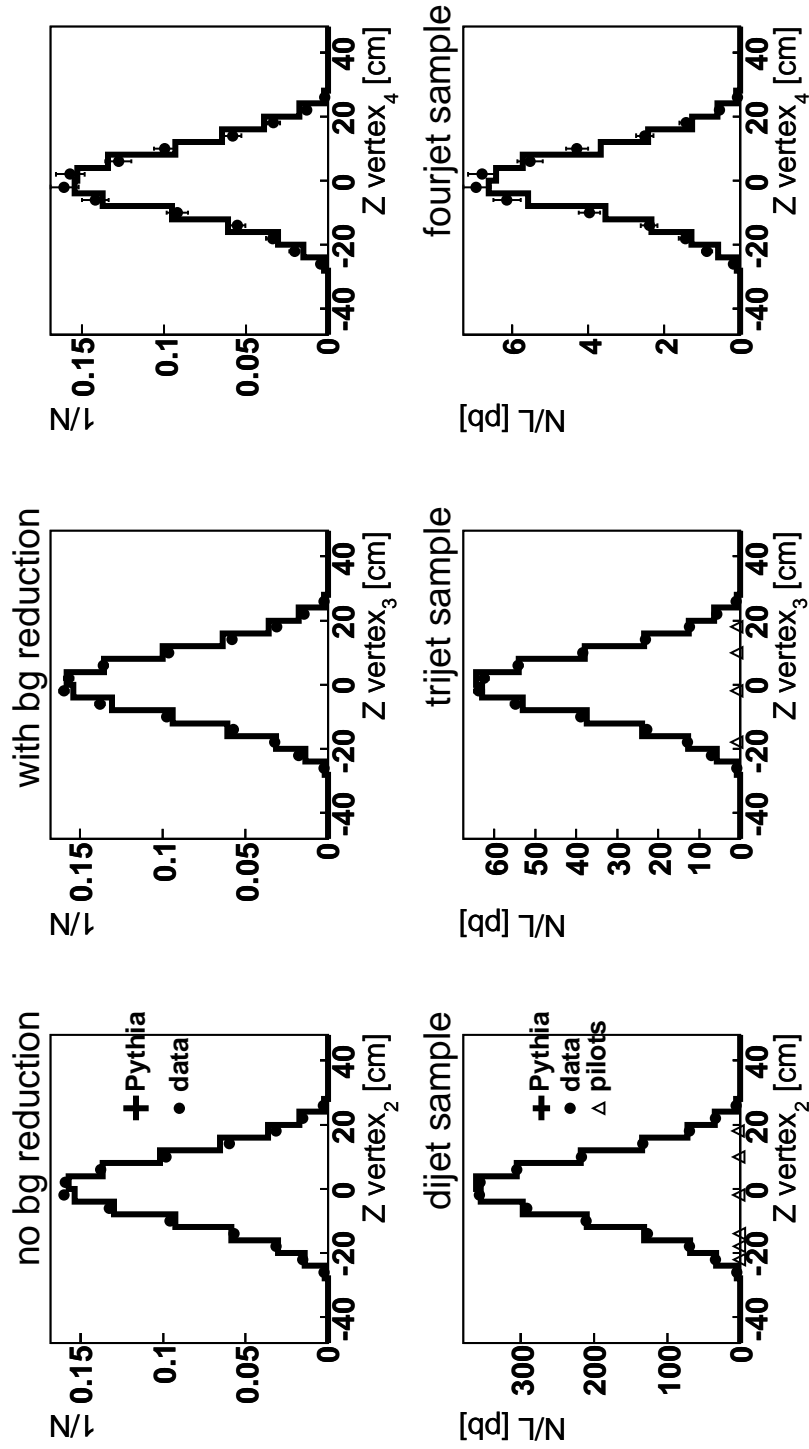
Figure 5.15: *The z-vertex distribution before (top) and after (bottom) reweighting the MC for the dijet, trijet and fourjet sample. The effect of the reweighting on the z-vertex distribution is negligible.*

In contrast to the reweighting for z-vertex, here the theoretical model is a subject to the reweighting procedure. To correct the model, the weighting function is extracted at reconstructed level but the event weight, w, is calculated as a function f of the corresponding observables, η_i, at particle (hadron) level:

$$w = f(\eta_i) \tag{5.7}$$

In an iterative procedure, the weighting function is fit again until the data is described. Actually, the exact reweighting procedure is not of a big importance as long as the resulting distributions describe the measured data as shown in Figure 5.18. Though, a wrong choice of reweighting variables will not give the desired improvement. The distributions of the sums before and after the reweighting procedure are shown in Figure 5.19 and Figure 5.20, respectively. Figure 5.21 and Figure 5.22 show the distributions of the differences before and after the reweighting procedure.
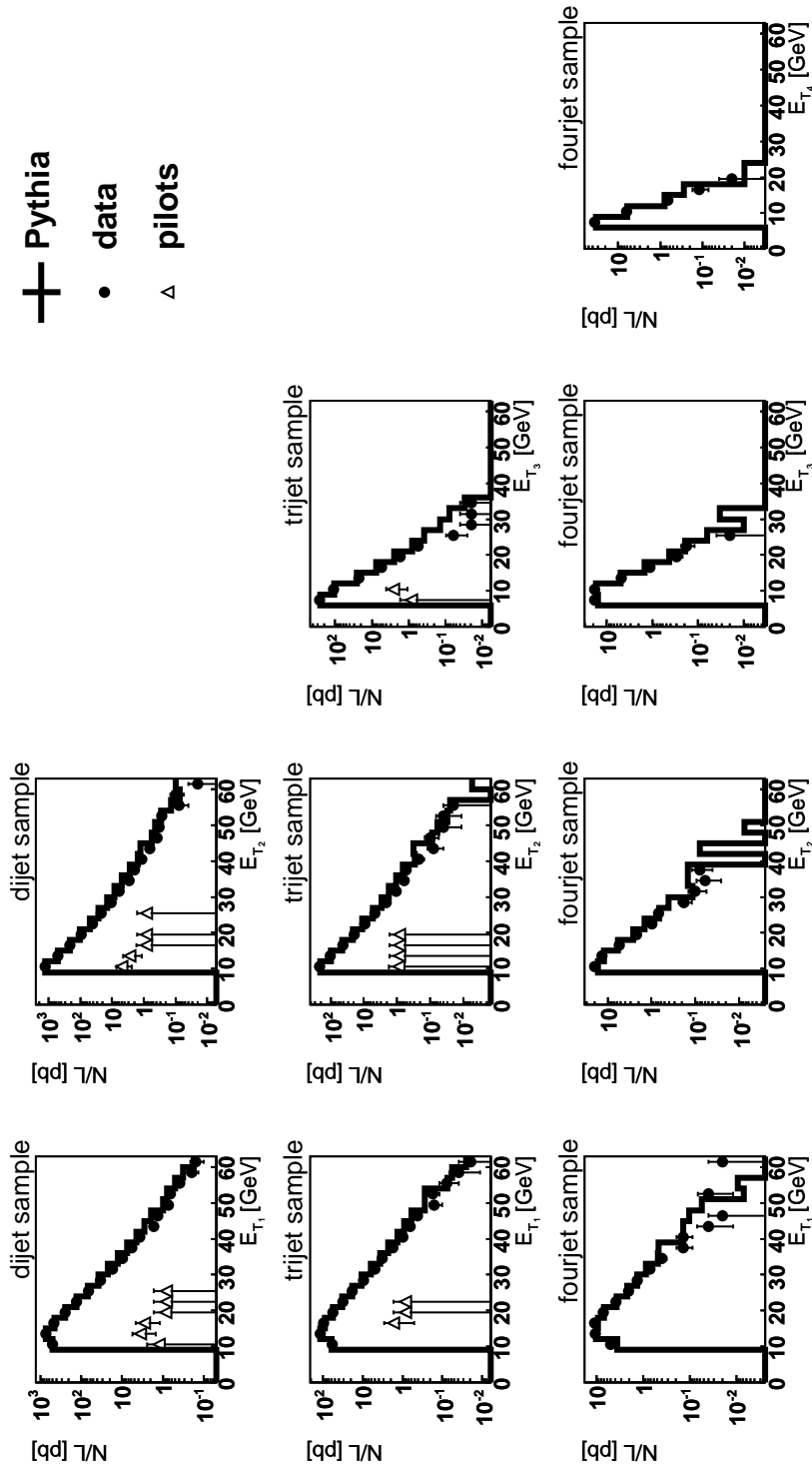
Figure 5.16: *The transverse energy of the jets for the dijet, trijet and fourjet samples.*
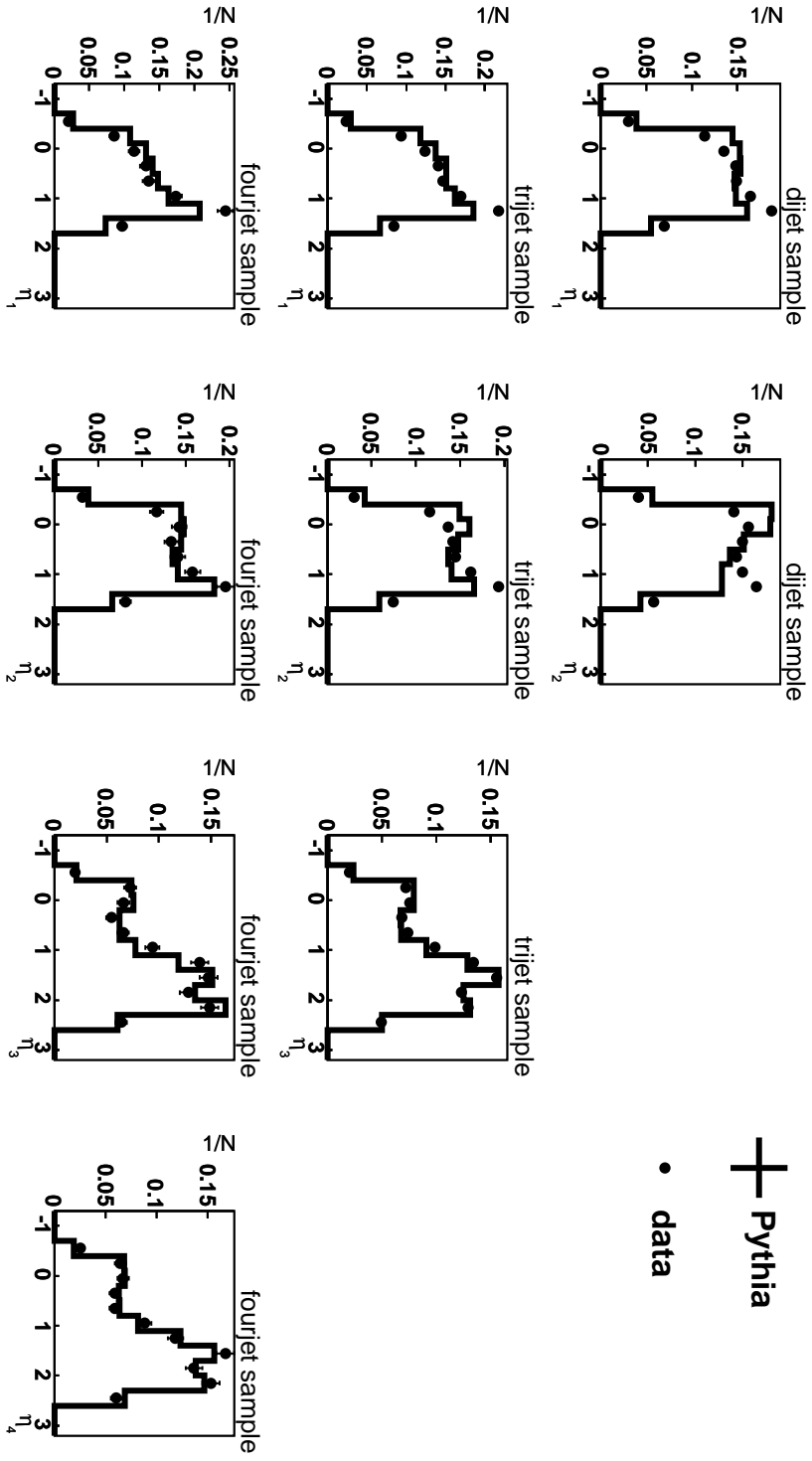
Figure 5.17: *The pseudorapidity of the jets for the dijet, trijet and fourjet samples before the reweighting procedure*
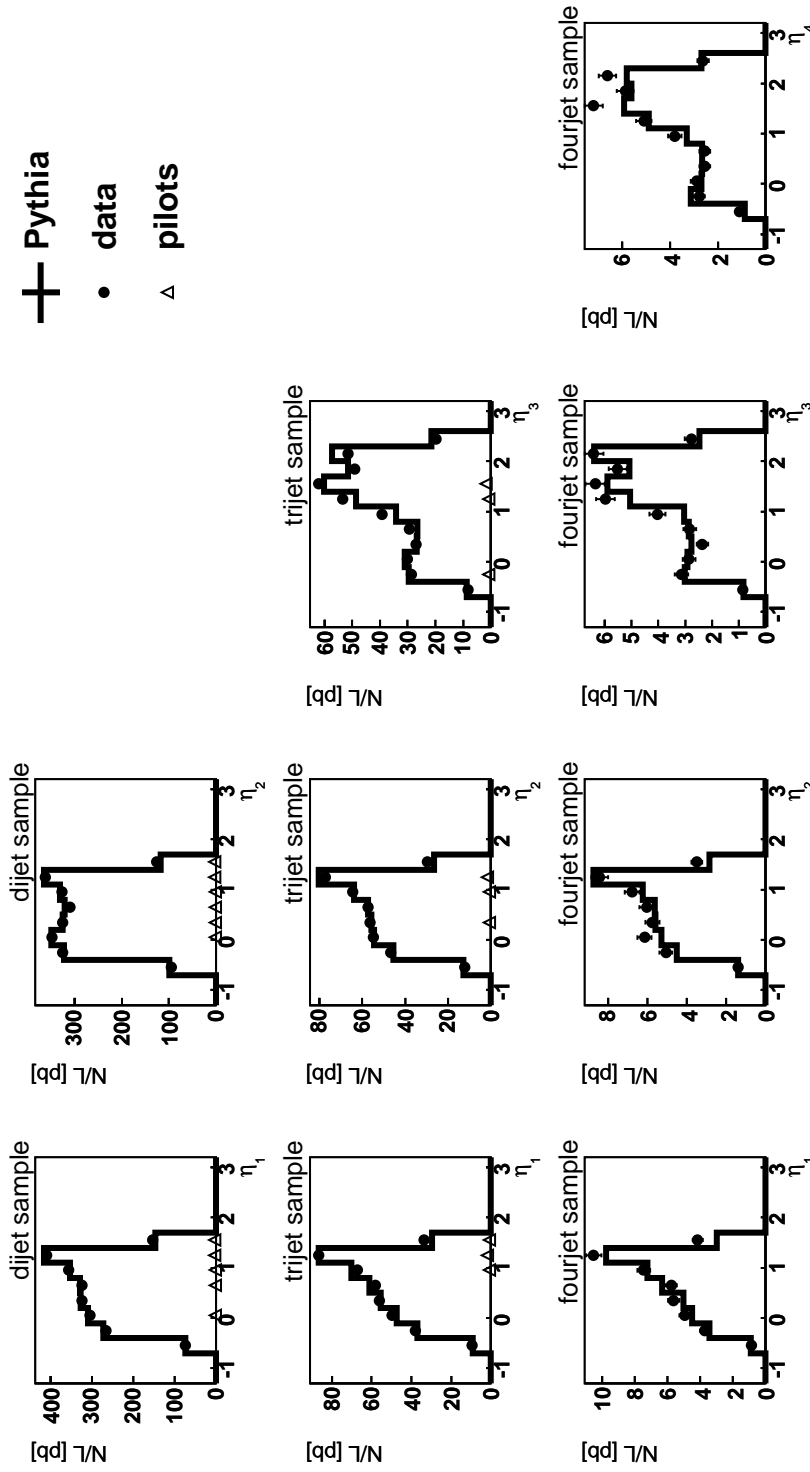
Figure 5.18: *The pseudorapidity of the jets for the dijet, trijet and fourjet samples after the reweighting on $\eta_1 + \eta_2$, $\eta_1 - \eta_2$, $\eta_1 + \eta_3$, $\eta_1 - \eta_3$, $\eta_2 + \eta_4$ and $\eta_2 - \eta_4$.*
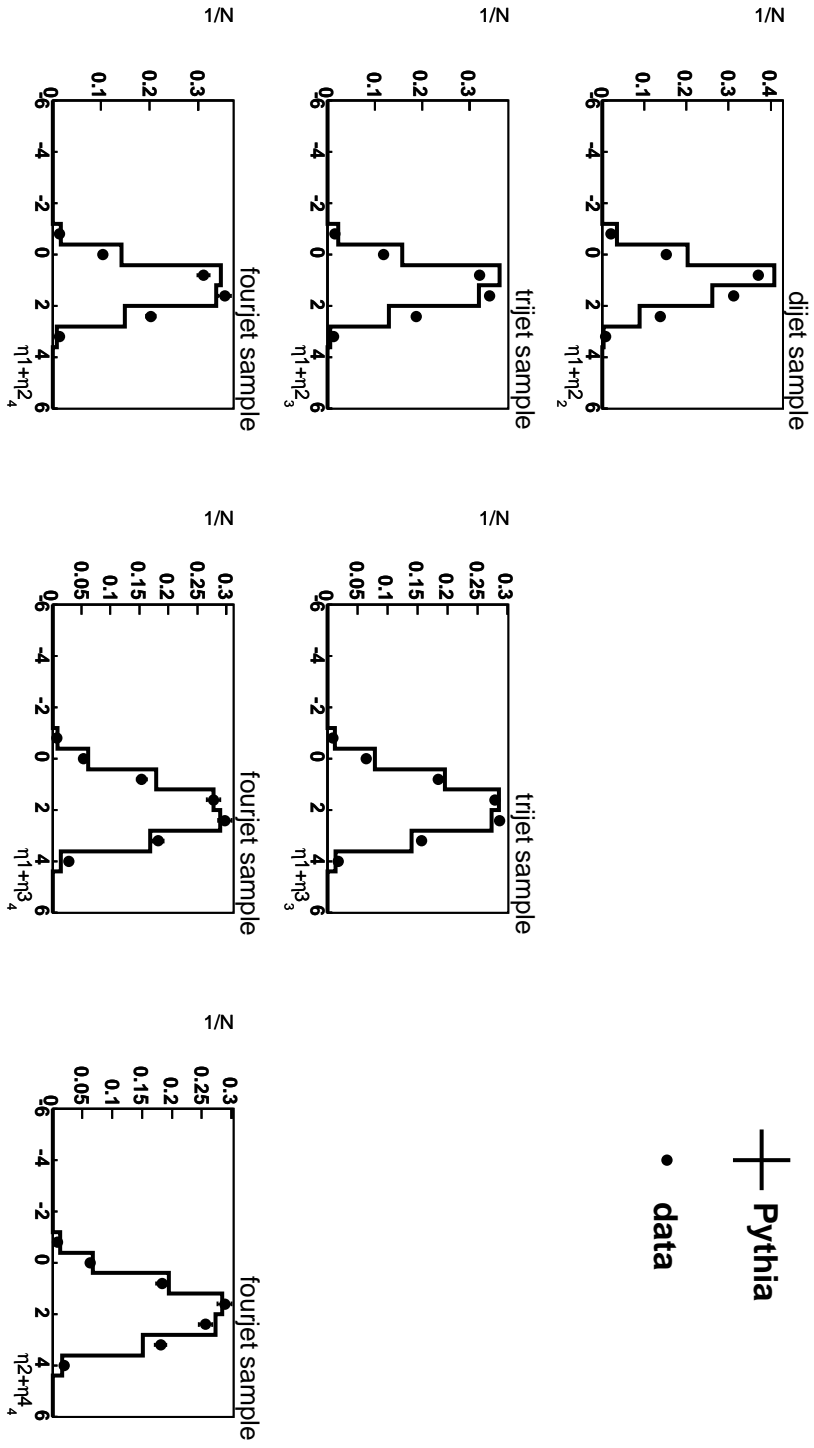
Figure 5.19: *The distributions of jet pseudorapidity sums for the dijet, trijet and fourjet samples before the reweighting of Monte Carlo for this variables.*

Figure 5.20: *The distributions of jet pseudorapidity sums for the dijet, trijet and fourjet samples after the reweighting of Monte Carlo for this variables.*

Figure 5.21: *The distributions of jet pseudorapidity differences for the dijet, trijet and fourjet samples before the reweighting of Monte Carlo for this variables.*
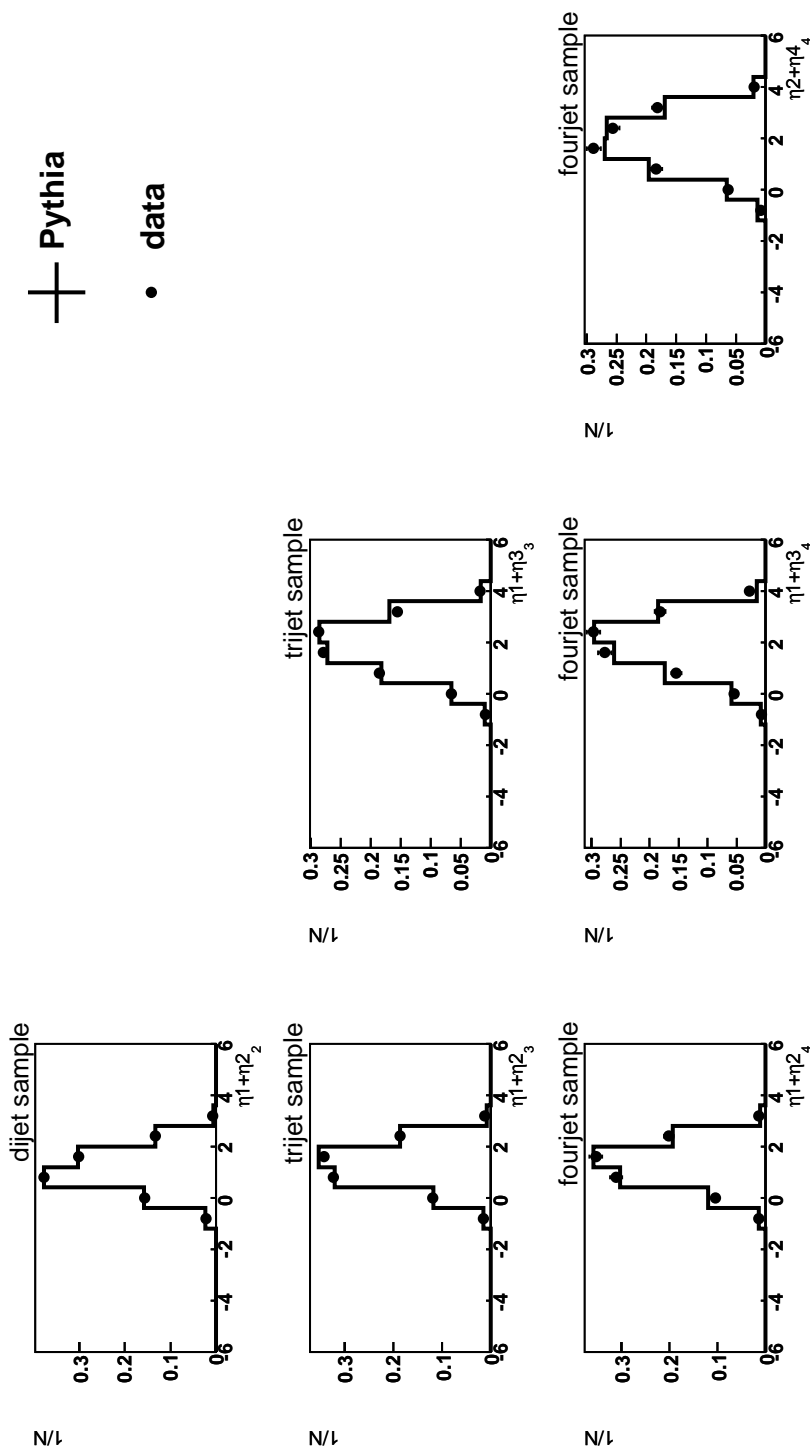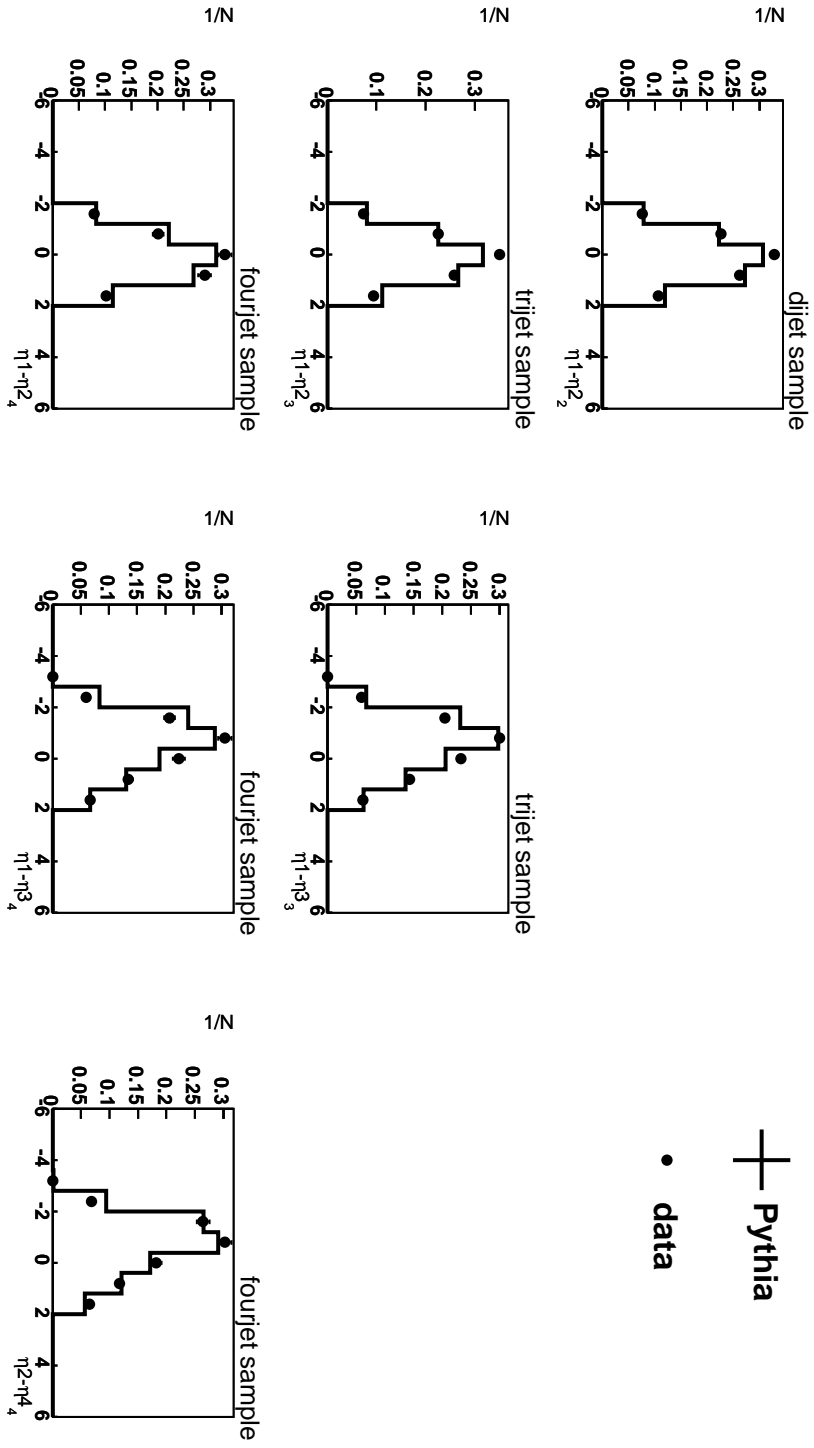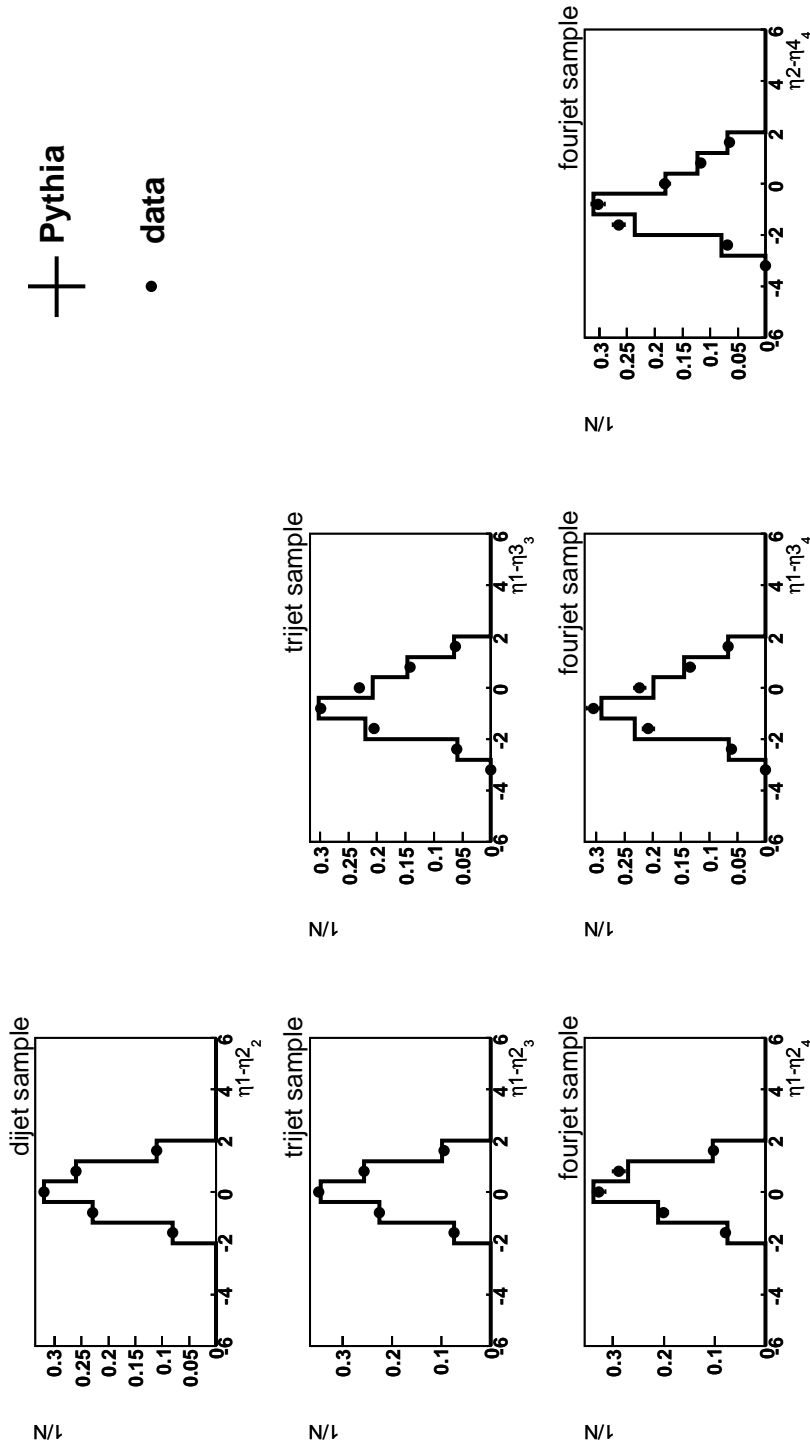
Figure 5.22: *The distributions of jet pseudorapidity sums for the dijet, trijet and fourjet samples after the reweighting of Monte Carlo for this variables.*

Chapter 6

Cross Section Determination and Results

The cross section in bin i is defined as

$$\sigma_i = \frac{N_i}{A_i \int \mathcal{L} \mathrm{d}t},$$ (6.1)

where N_i is the number of events and A_i is the detector acceptance in bin i. $\int \mathcal{L} \mathrm{d}t$ is the luminosity integrated over the time. The acceptance is calculated as the detector correction factor, C_i, and the trigger efficiency, ϵ_i, from

$$A_i = C_i \epsilon_i.$$ (6.2)

If the data is well described by the Monte Carlo sample, it can be used to calculate the corrections for detector effects. Before that, the cross sections are corrected for the trigger efficiency. The trigger efficiency is extracted from the data as described in Section 5.3.2 and Section 5.3.3.

6.1 Data Correction

The true distributions of the measured variables are distorted by fluctuations caused by the limited resolution of the detector. The predictions from theory can be folded with the detector response and compared with the reconstructed data. A disadvantage of this method is that it prevents the comparison to results from different experiments where different detectors are used.

A different approach is to correct the data for detector effects. The corrected distributions are independent from the measuring device and can be directly compared to the theoretical predictions and measurements from other experiments. The correction factors are extracted with the help of the simulated PYTHIA Monte Carlo

samples. For this purpose the distributions of each observable are compared at reconstructed and hadron level. The hadron/reconstructed level correlations for E_T and η of jets are shown in Figure 6.1 and Figure 6.2, respectively. Correlations are measured also for x_γ, as defined in Equation 1.22 and the invariant mass of the jet system, defined in Equation 5.6. The results are shown in Figure 6.3 and Figure 6.4, respectively. The correlation of the sum of the transverse energy of selected jets in shown in Figure 6.5. The good correlation between the variables measured guarantees that the correction procedure is correct.

6.1.1   The Bin-by-Bin Correction Method

In this analysis the method of *correction factors* known also as *bin-by-bin correction method* is used[50]. It is the simplest and most commonly used technique. The correction factors C_i are determined from MC. The model predictions for the observed and true number of events in bin i are rec_i and had_i. The correlation matrix R^{rec}_{had} is defined as the number of entries reconstructed in a given bin rec but created in a bin had. If the resolution effects are not negligible, the correlation matrix is not diagonal i.e. there are migrations between bins. The migrations are studied bu using the *purity* P_i and *stability* S_i of the measurement. For each bin i, P_i and S_i are defined by:

$$P_i = R_i^i / \sum_j R_j^i, \tag{6.3}$$

$$S_i = R_i^i / \sum_j R_i^j. \tag{6.4}$$

The purity gives the fraction of events reconstructed in the same bin as the are generated. The stability is the fraction of events generated in the same bin as they are reconstructed. The detector correction factor for bin i is calculated as

$$C_i = \sum_j R_j^i / \sum_j R_i^j. \tag{6.5}$$

The applicability of the bin-by-bin method is not restricted to problems where migrations between bins are small. However this procedure may bias the result if the distribution of the observable in the simulated events differs from the data[50]. To apply this method at least one of two conditions should be fulfilled.

- Migrations between bins are small.

- The reconstructed data sample is described in details by the Monte Carlo simulation.

The phase space of the measurement for the dijet, trijet and fourjet is summarized in Table 6.1. For more details see Chapter 5. The purity and stability of the measurement are shown in Figure 6.6 - Figure 6.10. The width of the bins is adjusted to keep the purity and stability higher than 0.3. The stability is always higher than
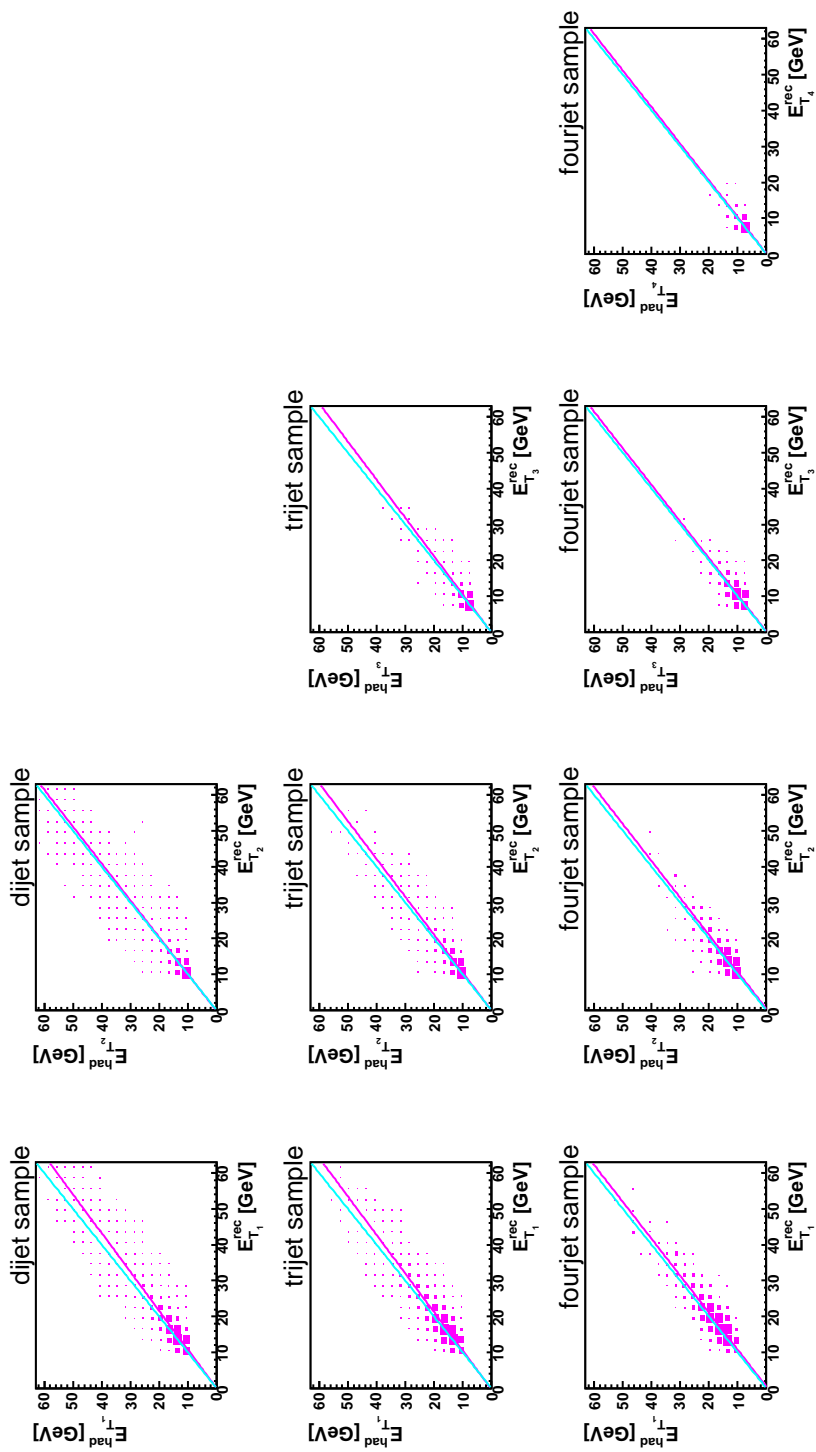
Figure 6.1: *The correlation between hadron and reconstructed level of the transverse energy of jets for the dijet, trijet and fourjet samples.*
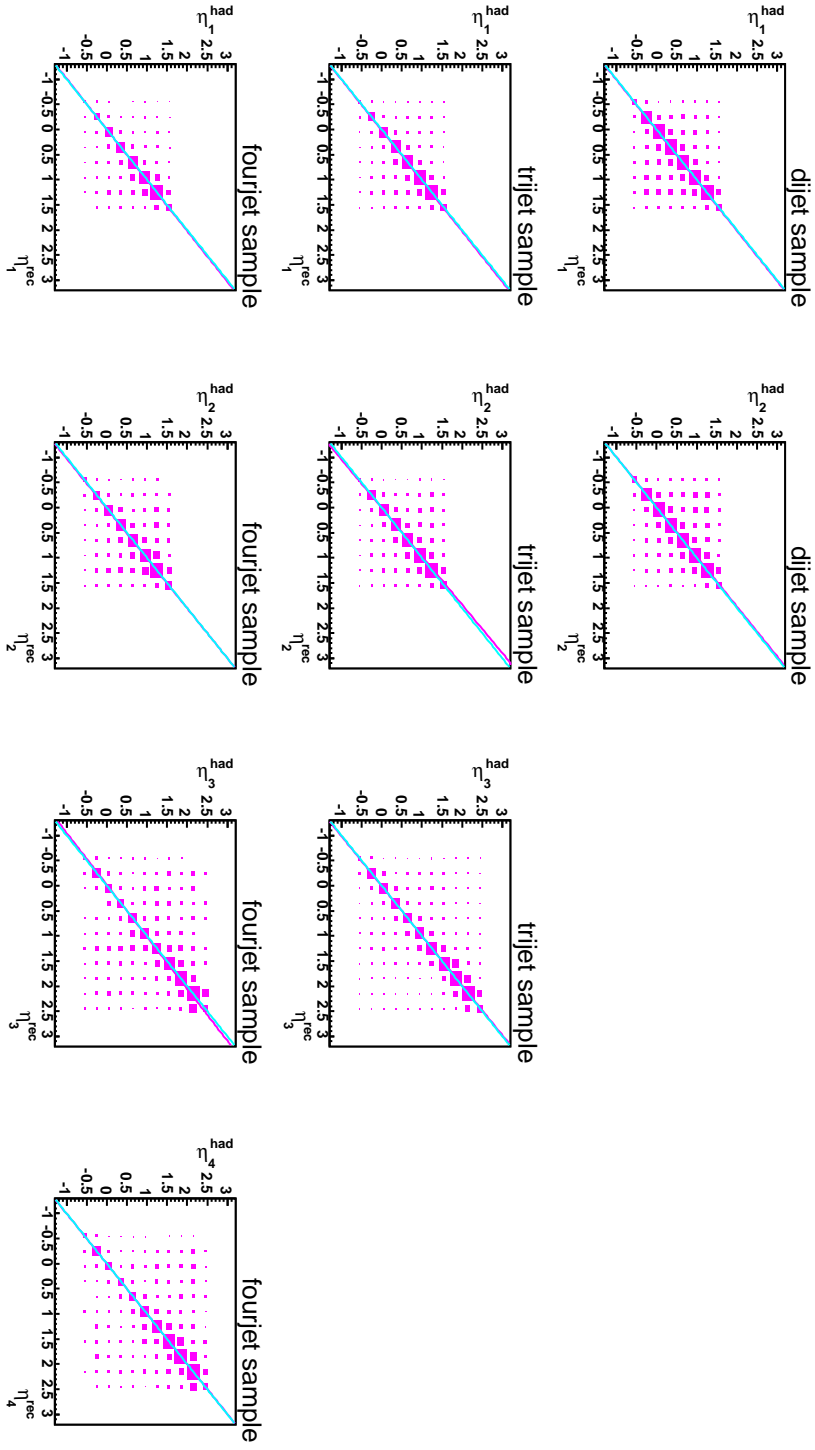
Figure 6.2: *The correlation between hadron and reconstructed level of the pseudorapidity of jets for the dijet, trijet and fourjet samples.*
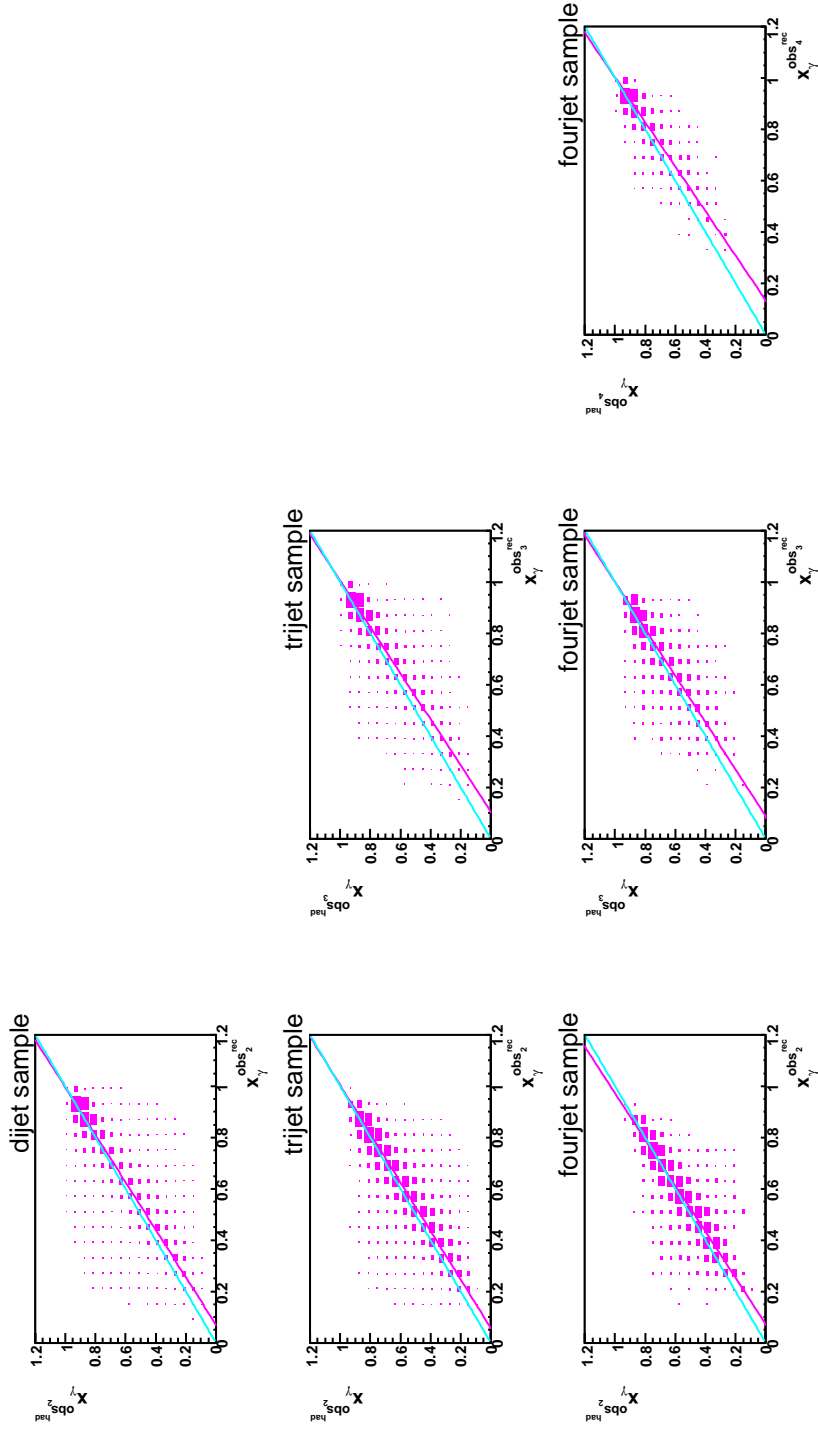
Figure 6.3: *The correlation between hadron and reconstructed level of* x_γ *as measured from the two hardest jets, from the three hardest jets and from all available jets for the dijet, trijet and fourjet scenario.*
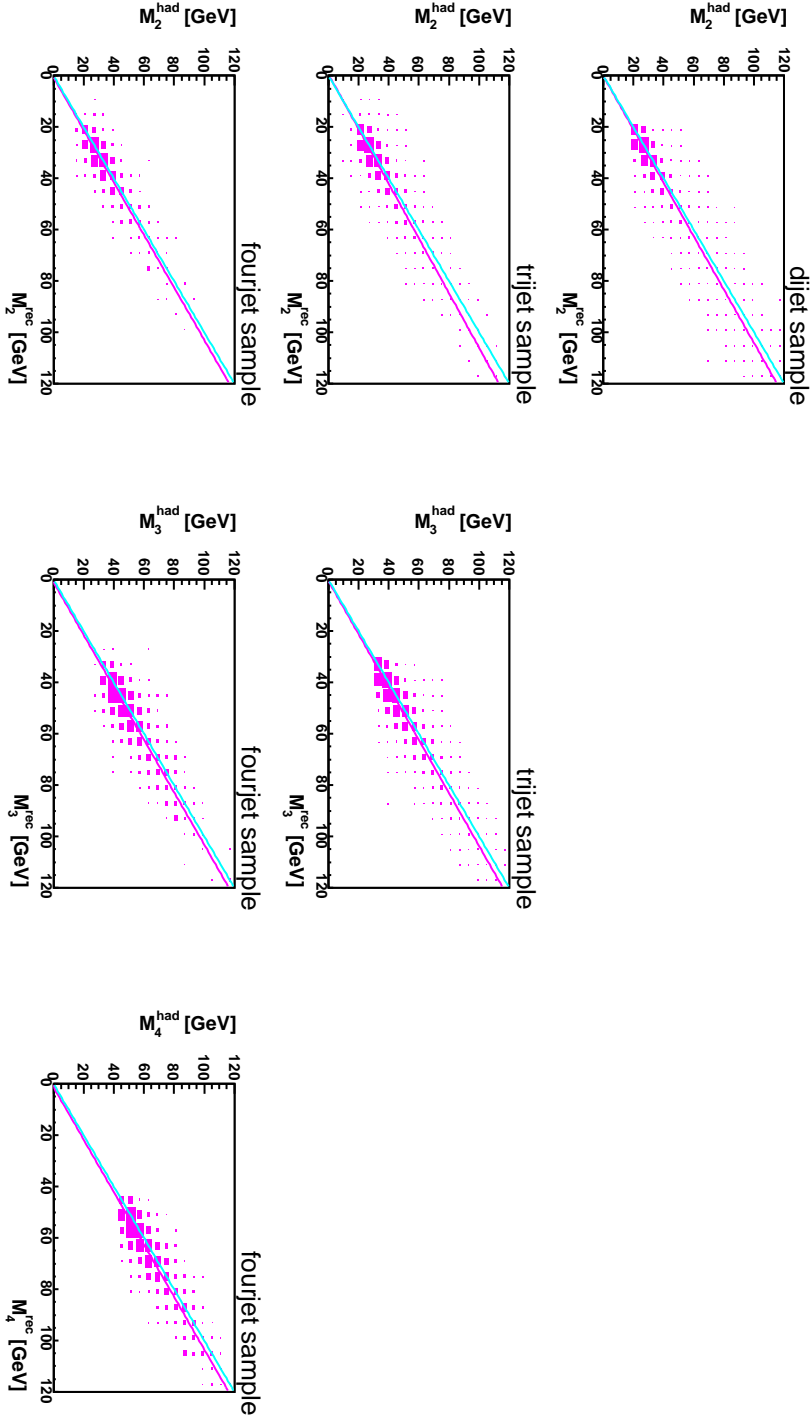
Figure 6.4: *The correlation between hadron and reconstructed level of the invariant mass of the jet system as measured from the two hardest jets, from the three hardest jets and from all available jets for the dijet, trijet and fourjet scenario.*
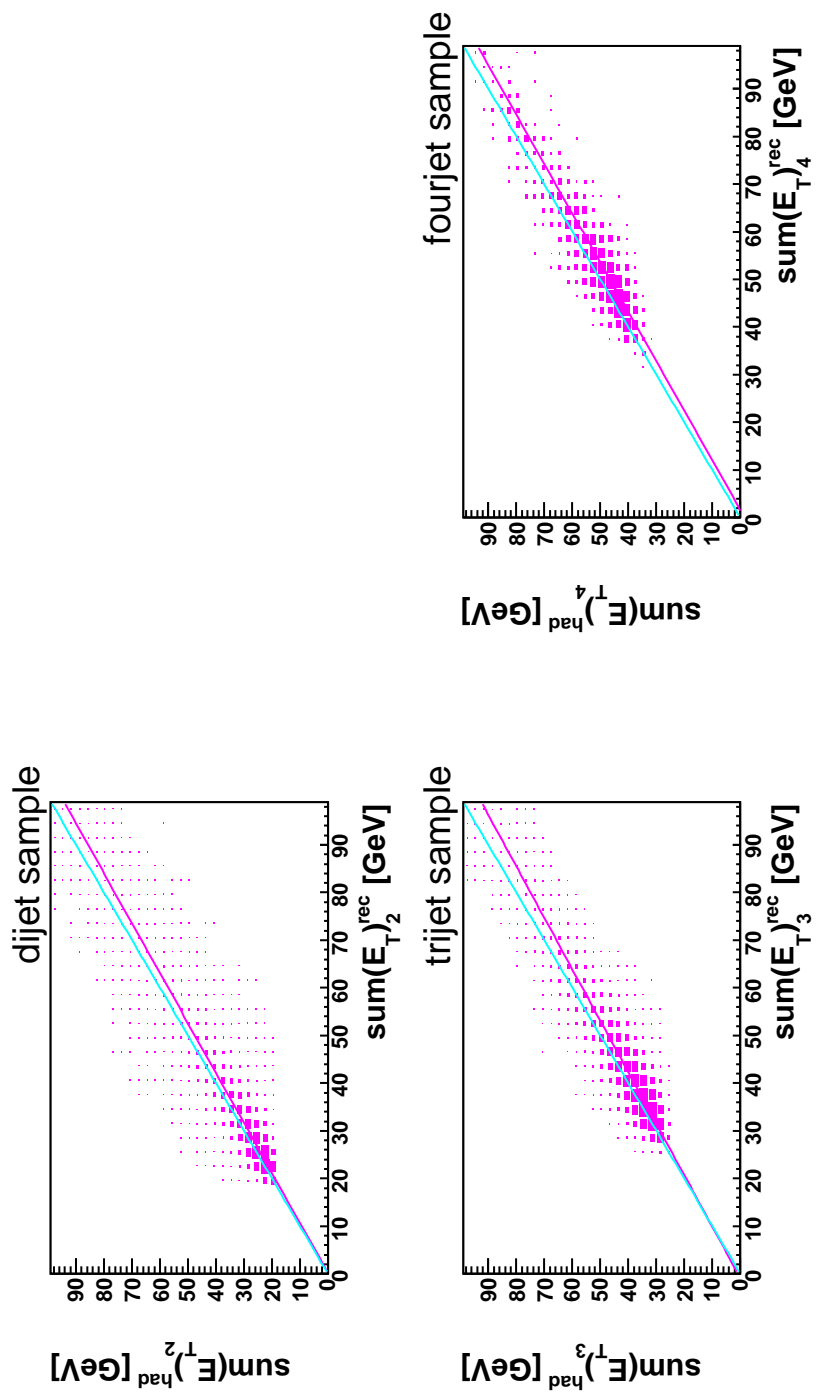
Figure 6.5: *The correlation between hadron and reconstructed level of the sum of the transverse energy of the jets as measured from the for the dijet, trijet and fourjet samples.*

Table 6.1: *Phase space of the measurement*

$0.3 < y_{JB} < 0.9$
$-0.5 < \eta_{jet1,2} < 1.5$
$-0.5 < \eta_{jet3,4} < 2.4$
$E_{T,jet1,2} > 9\,\mathrm{GeV}$
$E_{T,jet3,4} > 6\,\mathrm{GeV}$
$M_{2j} > 20\,\mathrm{GeV}$
$M_{3j} > 30\,\mathrm{GeV}$
$M_{4j} > 45\,\mathrm{GeV}$

purity and decreases with the jet multiplicity from 0.4-0.5 for the dijet sample to 0.3-0.4 in the fourjet scenario. The purity is lower than 0.3 only for the fourjet scenario. As long as the purity and stability of the analysis are not high, the reconstructed Monte Carlo sample used for determining the detector corrections must described the data for the bin-by-bin method to be valid. As shown in Chapter 5, all distributions on reconstructed level are well described except the pseudorapidity of the jets. To improve this, the Monte Carlo events are reweighted as a function of the difference and the sum of the pseudorapidity of the jets. The correction factors vary between 0.9 and 1.5, except for the fourjet sample where correction factors are not larger than 1.9.

6.2   Comparison to Dijets with High Transverse Momenta

The x_γ cross section as reconstructed from Equation 1.22 is measured in the phase space of the "Photoproduction of dijets with high transverse momenta at HERA" analysis[51]. This analysis was done with HERA I data and is the last published study of jets in photoproduction. Events are selected if E_T of the hardest jet is greater than 25 GeV and E_T of the second jet is greater than 15 GeV in pseudorapidity range of $-0.5 < \eta < 2.75$. The results, shown in Figure 6.11, confirm the previous measurement. The difference between published data and the presented cross check in the last bin of the low x_p cross section is explained by additional cuts on the jet mass and jet size, applied in the previous measurement but not considered in current analysis. The purpose of the cuts is to reduce the contamination from DIS events. This is the reason why differences appear in the high x_γ region.

6.3   Systematic Uncertainty

The sources of systematic uncertainty are summarized in Table 6.2. The uncertainty of the luminosity measurement for the 2006 e^- run period is 2.5 %. The energy scale uncertainty is extracted from PYTHIA Monte Carlo samples. It is calculated
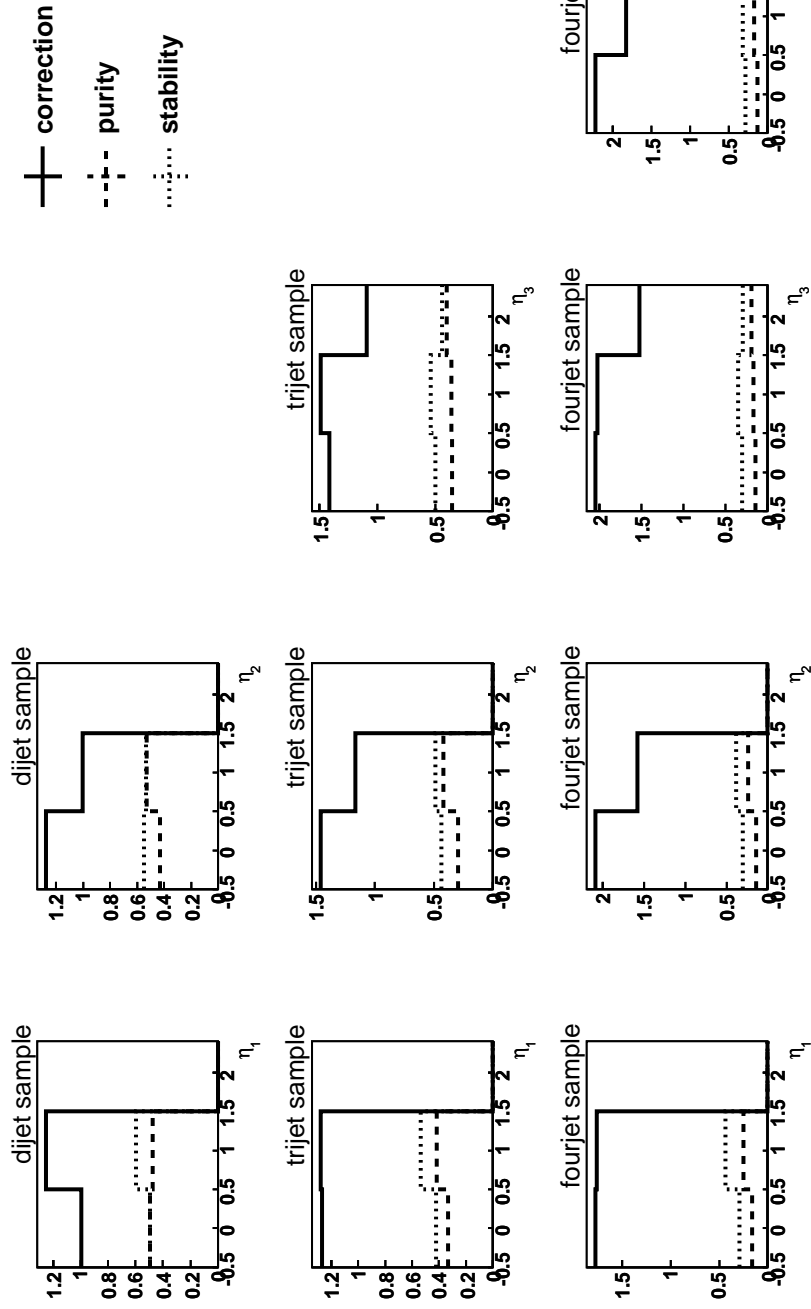
Figure 6.6: *Purity, stability and correction factors of the jet pseudorapidity measurement for the dijet, trijet and fourjet samples after the reweighting on $\eta_1 + \eta_2$, $\eta_1 - \eta_2$, $\eta_1 + \eta_3$, $\eta_1 - \eta_3$, $\eta_2 + \eta_4$ and $\eta_2 - \eta_4$, as described in Section 5.5.2.*
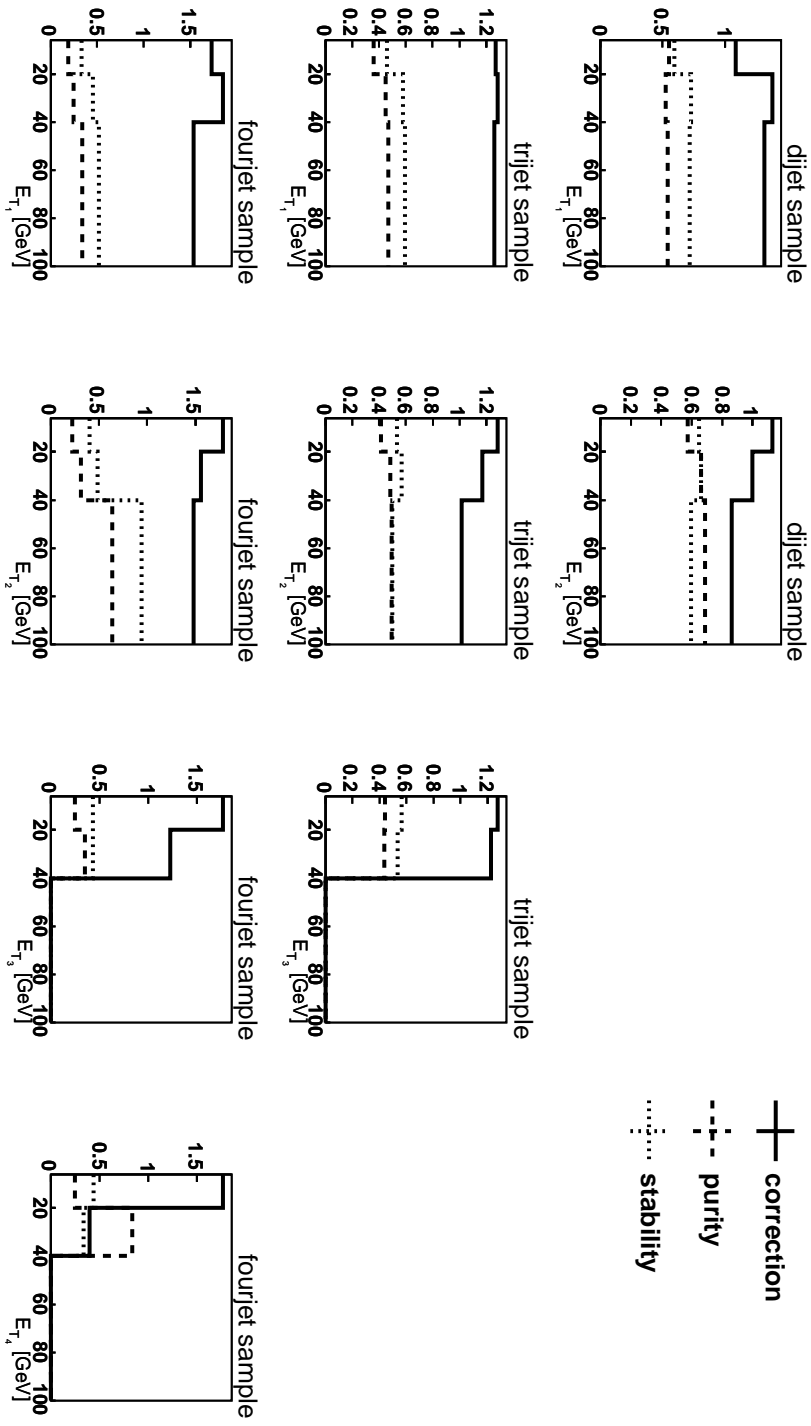
Figure 6.7: *Purity, stability and correction factors of the jet transverse energy measurement for the dijet, trijet and fourjet samples.*
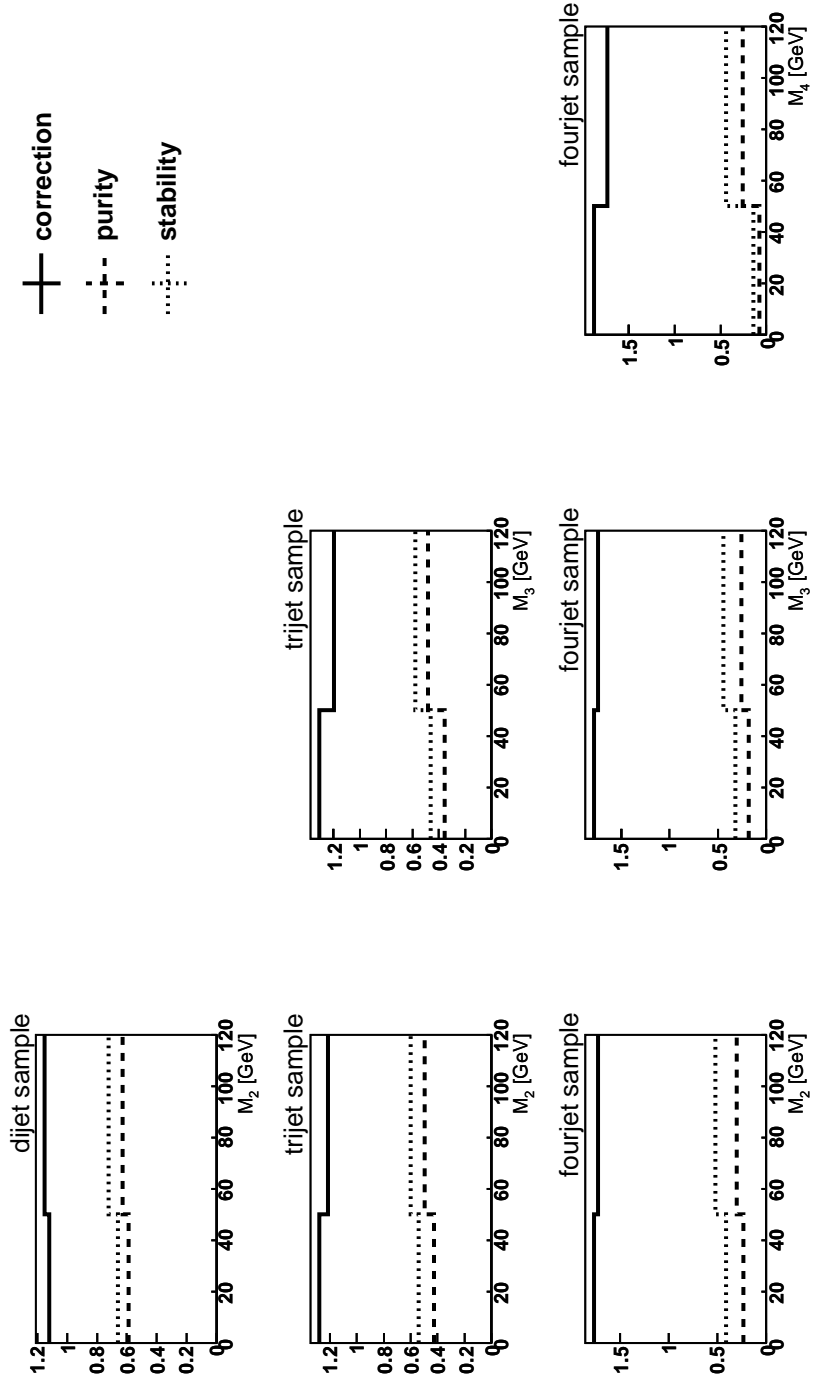
Figure 6.8: *Purity, stability and correction factors of the invariant mass measurement for the dijet, trijet and fourjet samples.*
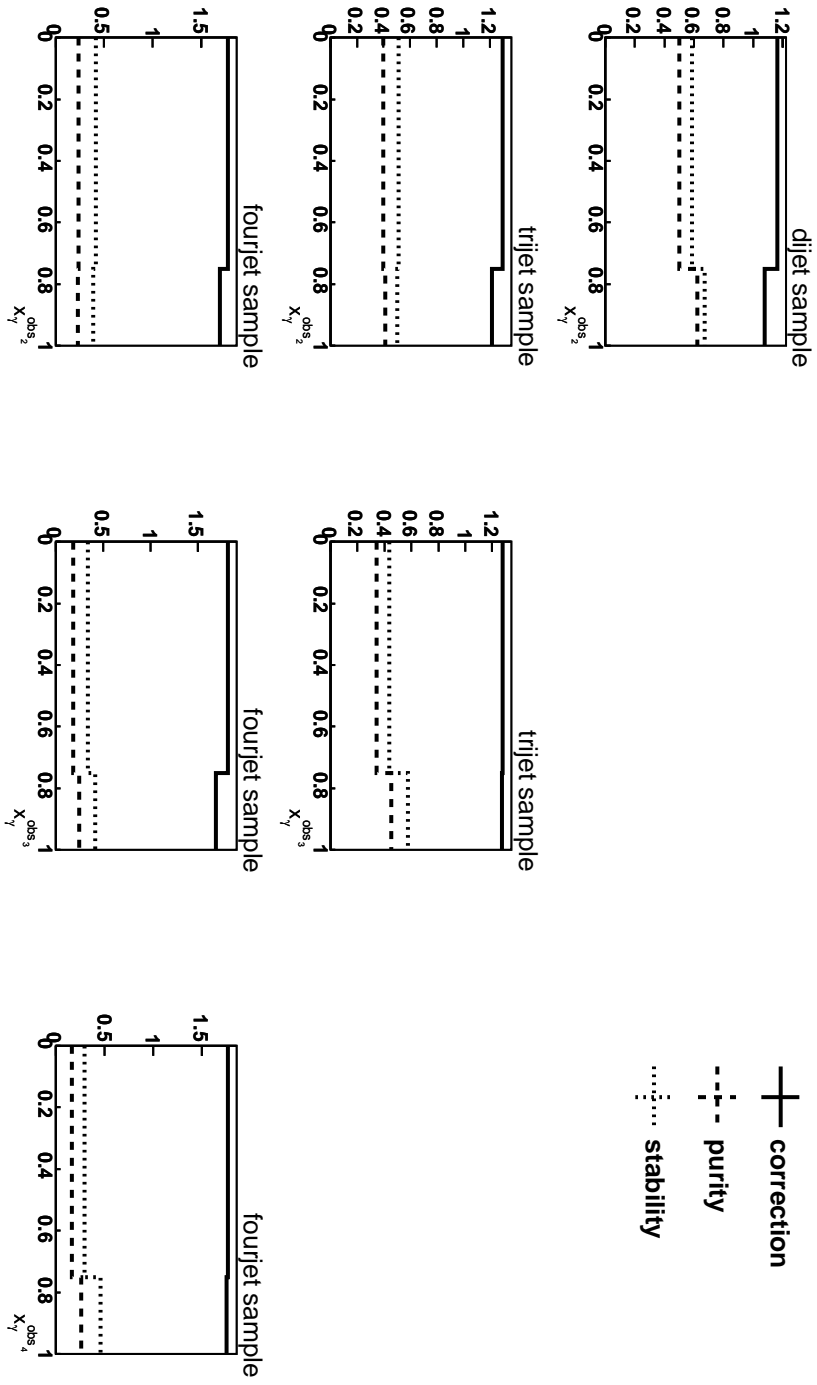
Figure 6.9: *Purity, stability and correction factors of the x_γ measurement for the dijet, trijet and fourjet samples.*
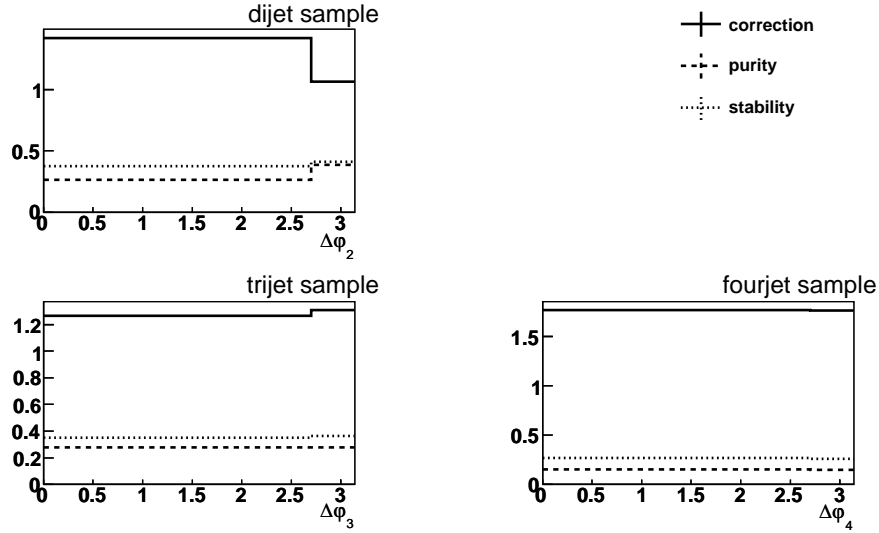
Figure 6.10: *Purity, stability and correction factors of the $\Delta\phi$ measurement for the dijet, trijet and fourjet samples.*

Table 6.2: *Systematic uncertainties*

source	dijet	trijet	fourjet
Luminosity	$\pm2.5\,\%$	$\pm2.5\,\%$	$\pm2.5\,\%$
Trigger efficiency	$\pm2.0\,\%$	$\pm2.0\,\%$	$\pm2.0\,\%$
Energy scale	+0.6/-0.5 %	+1.4/-1.2 %	+4.5/-3.7 %

Table 6.3: *The effect of the energy scale variation on the cross sections*

	dijet	trijet	fourjet
Minimum	+6.6/-6.6 %	+6.0/-6.3 %	+3.0/-5.1 %
Average	+7.5/-7.3 %	+7.7/-7.9 %	+8.3/-8.4 %
Maximum	+9.8/-9.1 %	+14.5/-15.4 %	+15.2/-16.2 %

by shifting the four vectors of the input particles for the jet finder by 2 %. In this way the uncertainty of the energy measurement in the calorimeter as well as the uncertainty of the track measurement are considered. The minimum, maximum and average values of the cross section systematic error due to the energy uncertainty for different scenarios are shown in Table 6.3. The uncertainty from the trigger efficiency calculation is always below 2 %.
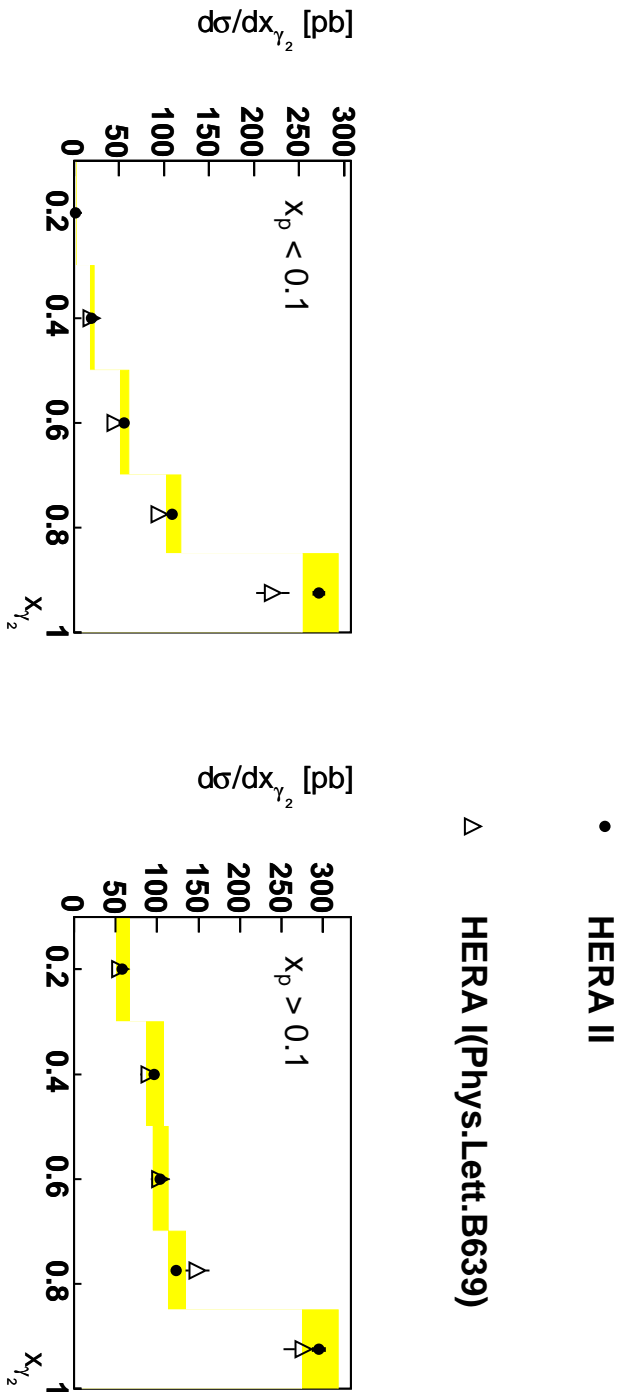
Figure 6.11: *Bin averaged cross section as a function of x_γ. Published data are shown with open triangles. Black circles denote The cross sections are shown separately for two regions in x_p, as defined in Equation 1.23.*

6.4   Monte Carlo Scaling Factors

In the cross section plots data are corrected for trigger efficiency and detector effects and compared to several Monte Carlo samples, namely, PYTHIA with and without multiple interactions, HERWIG with and without multiple interactions and CASCADE with two different sets of gluon densities, set A and set B. The Monte Carlo samples are scaled to the data for the jet multiplicity as explained in Section 5.5. The shape of the observable distributions is not changed by the scaling. There are scaling factors for each jet multiplicity and Monte Carlo generator. The values of the scaling factors are presented in Table 5.9. The effect of the scaling is illustrated in Figure 6.12. It shows the jet multiplicity as predicted from different Monte Carlo generators before and after the scaling.

6.5   Cross Sections

The measured visible cross sections for different scenarios are

$$\sigma_{dijet} = 1973.39 \pm 7.89 (\text{stat.})^{+142.08}_{-138.14} (\text{syst.}) \, \text{pb}, \tag{6.6}$$

$$\sigma_{trijet} = 312.52 \pm 2.81 (\text{stat.})^{+23.44}_{-23.13} (\text{syst.}) \, \text{pb}, \tag{6.7}$$

$$\sigma_{fourjet} = 24.46 \pm 0.83 (\text{stat.})^{+1.69}_{-1.69} (\text{syst.}) \, \text{pb}. \tag{6.8}$$

Differential cross sections are measured as a function of the transverse energy of the selected jets and their pseudorapidity. Also presented are the cross sections, differential in the invariant mass of the jet system defined in Equation 5.6 and x_γ, defined in Equation 1.22.

In addition, the azimuthal angle between the two hardest jets is measured. All cross sections are shown for the dijet, trijet and fourjet scenario. The statistical error is given as a vertical line for each bin of the measured observables. The energy scale uncertainty is represented by yellow bars in the plots.

The cross sections, differential in the jet transverse energy(Figure 6.13) and jet pseudorapidity(Figure 6.15) are measured for each of the jets. The jets are ordered in decreasing transverse energy such as the index 1 stands for the highest E_T jet. The ratio of model predictions to the measured data for the jet transverse energy is shown in Figure 6.14.

The invariant mass of the jet system is compared to PYTHIA with SAS-G and GRV-G photon PDFs in Figure 6.16. A comparison with more Monte Carlo generators is shown in Figure 6.17. The invariant mass is measured from the two leading jets for all data samples. In addition, for the trijet and fourjet samples they are measured from the three highest transverse energy jets and for the fourjet sample - from all four jets. The same consistency is followed on the x_γ cross sections shown in Figure 6.18.
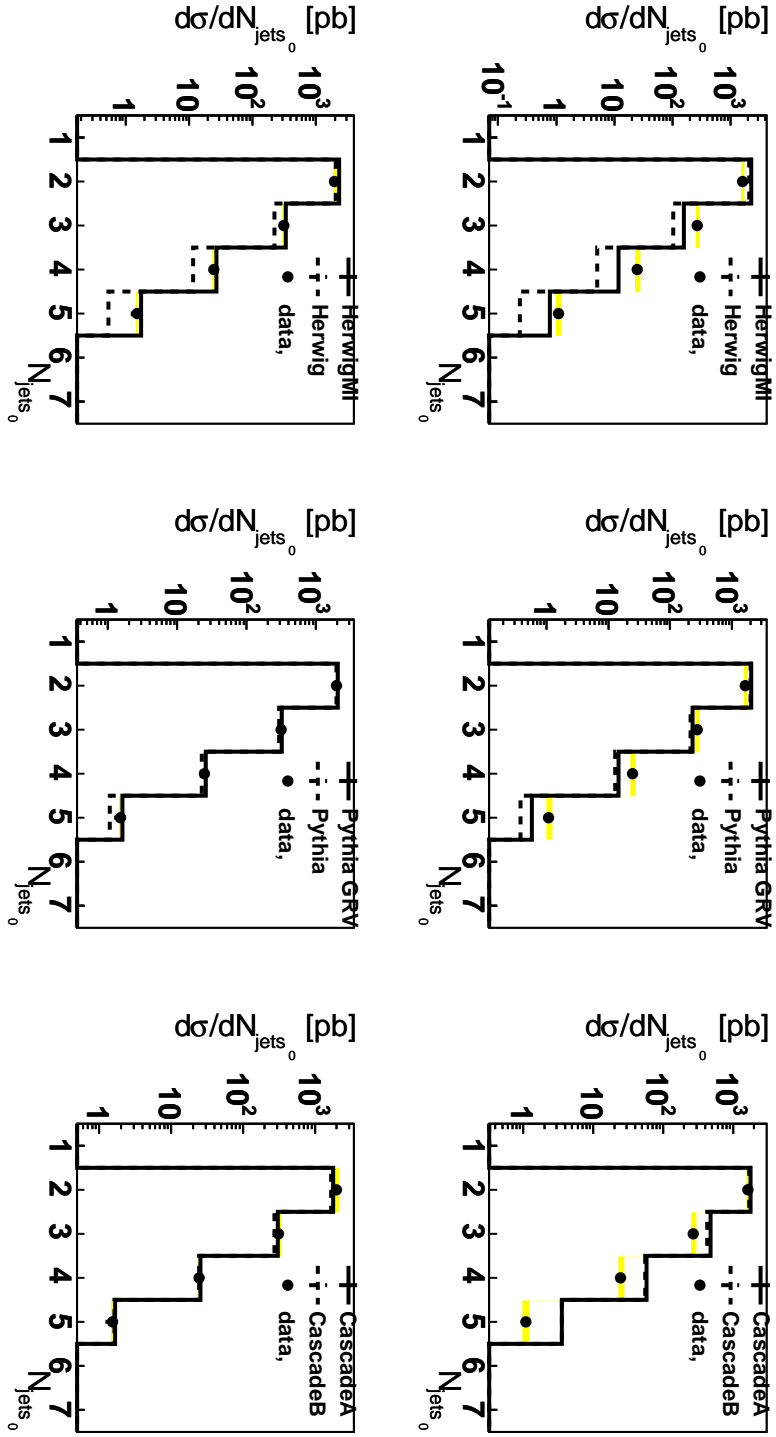
Figure 6.12: *Differential cross sections as a function of the jet multiplicity before (top) and after (bottom) Monte Carlo scaling. Corrected data are compared to HERWIG with and without multiple interactions, PYTHIA with and without multiple interactions and CASCADE with two different sets of gluon density, A and B.*
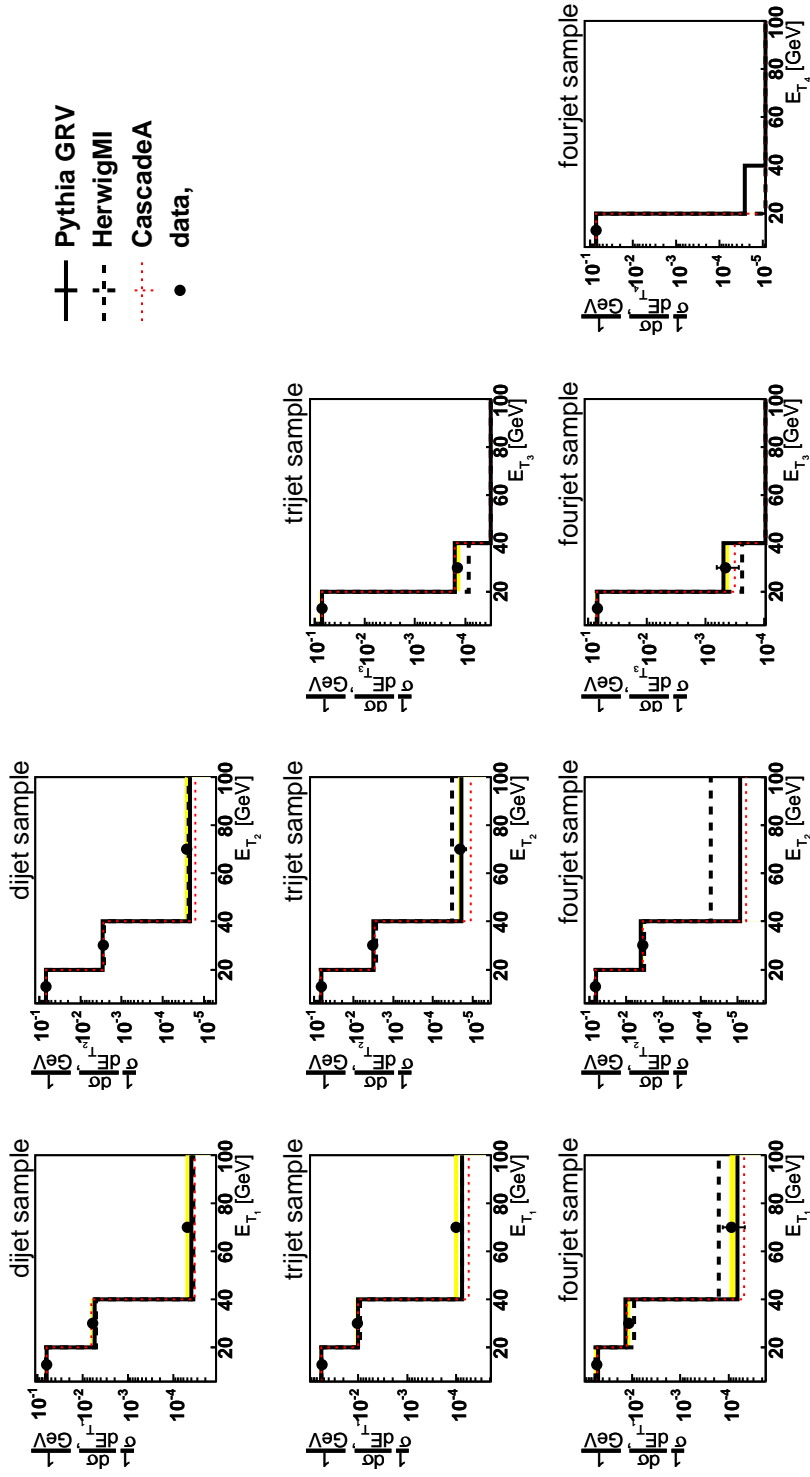
Figure 6.13: *Differential cross sections normalized to the visible cross section as a function of the jet transverse energy for the selected jets in the dijet, trijet and fourjet samples. Corrected data are compared to predictions from* HERWIG, PYTHIA *and* CASCADE.
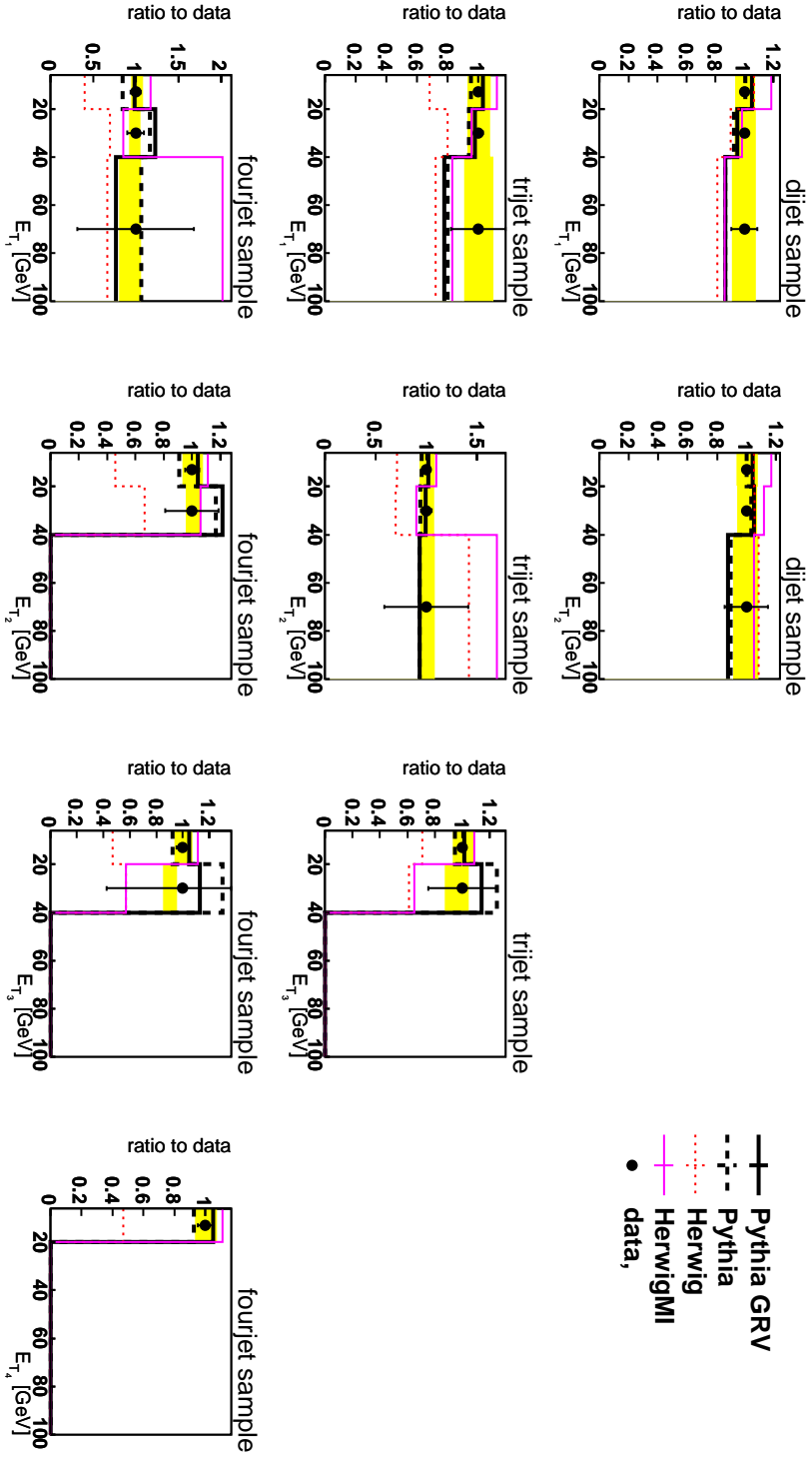
Figure 6.14: *The ratio of* HERWIG *and* PYTHIA *to the measured data of the differential cross sections as a function of the jet transverse energy for the dijet, trijet and fourjet samples. Models with multiple interactions are represented by solid lines while dashed lines correspond to models without multiple interactions.*
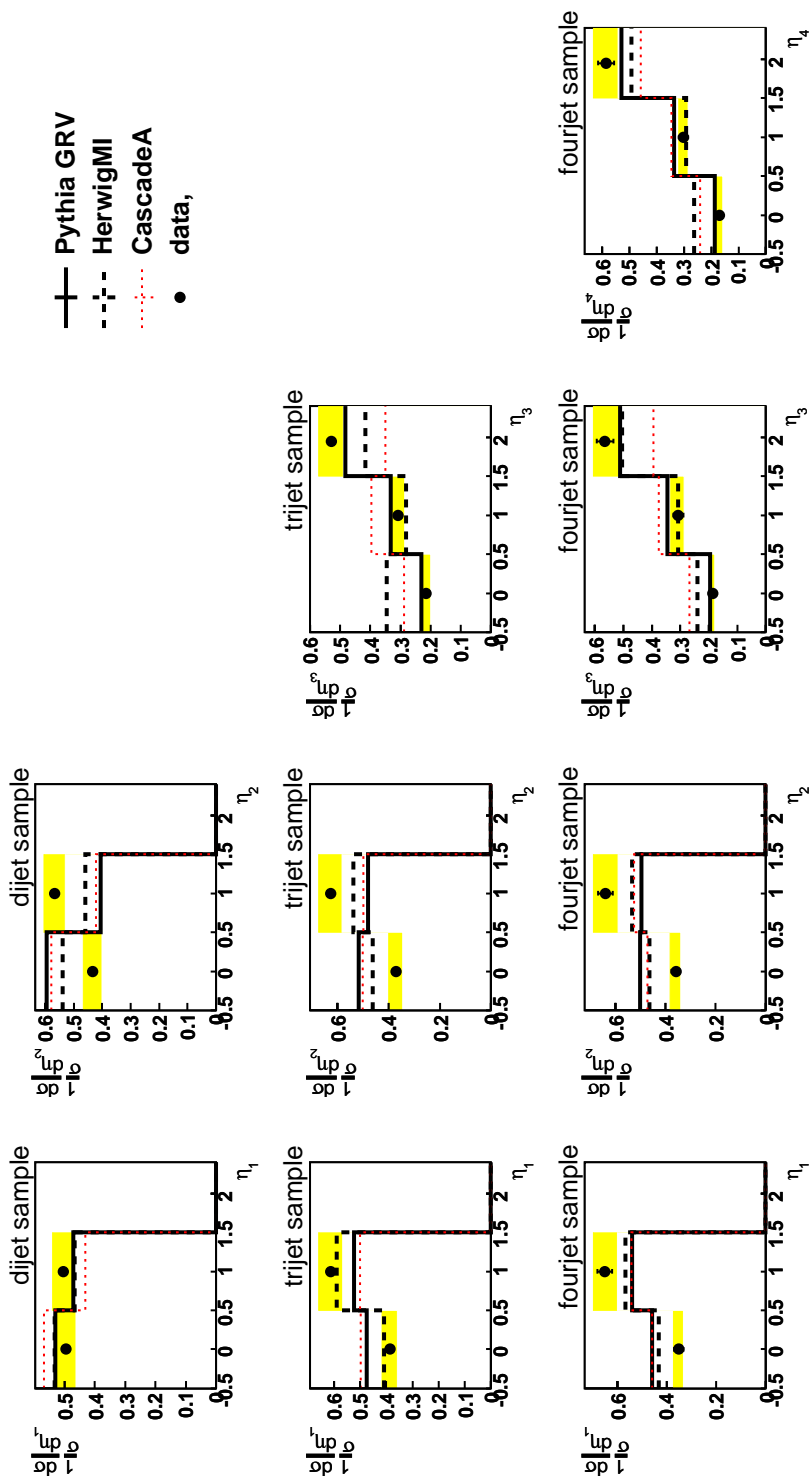
Figure 6.15: *Differential cross sections normalized to the measured cross section as a function of the jet pseudorapidity for the selected jets in the dijet, trijet and fourjet samples. Corrected data are compared to* HERWIG, PYTHIA *and* CASCADE *predictions.*
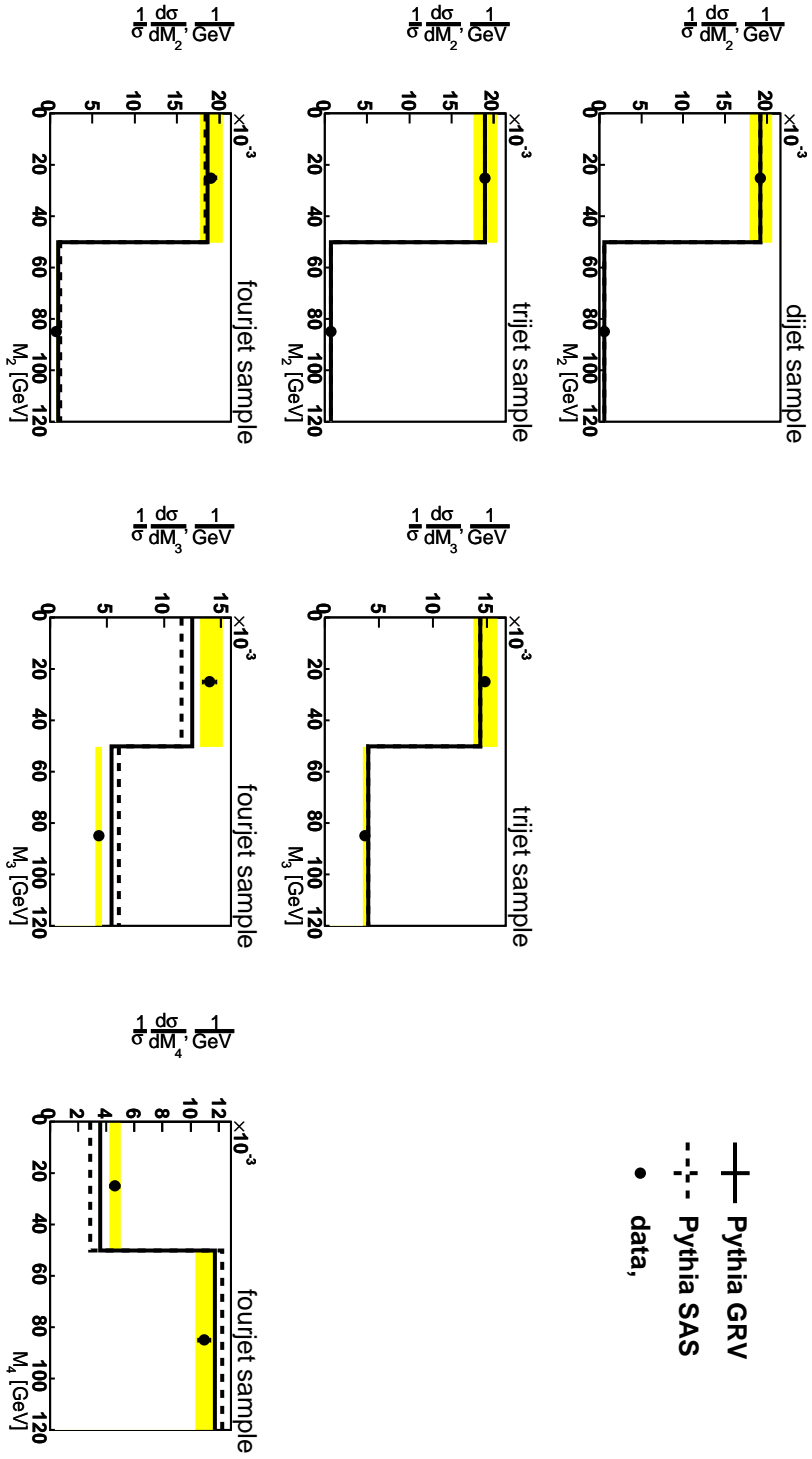
Figure 6.16: *Differential cross sections normalized to the visible cross section as a function of the invariant mass for the selected jets in the dijet, trijet and fourjet samples. Corrected data are compared to* PYTHIA *predictions with two different photon PDFs, SAS-G and GRV-G.*
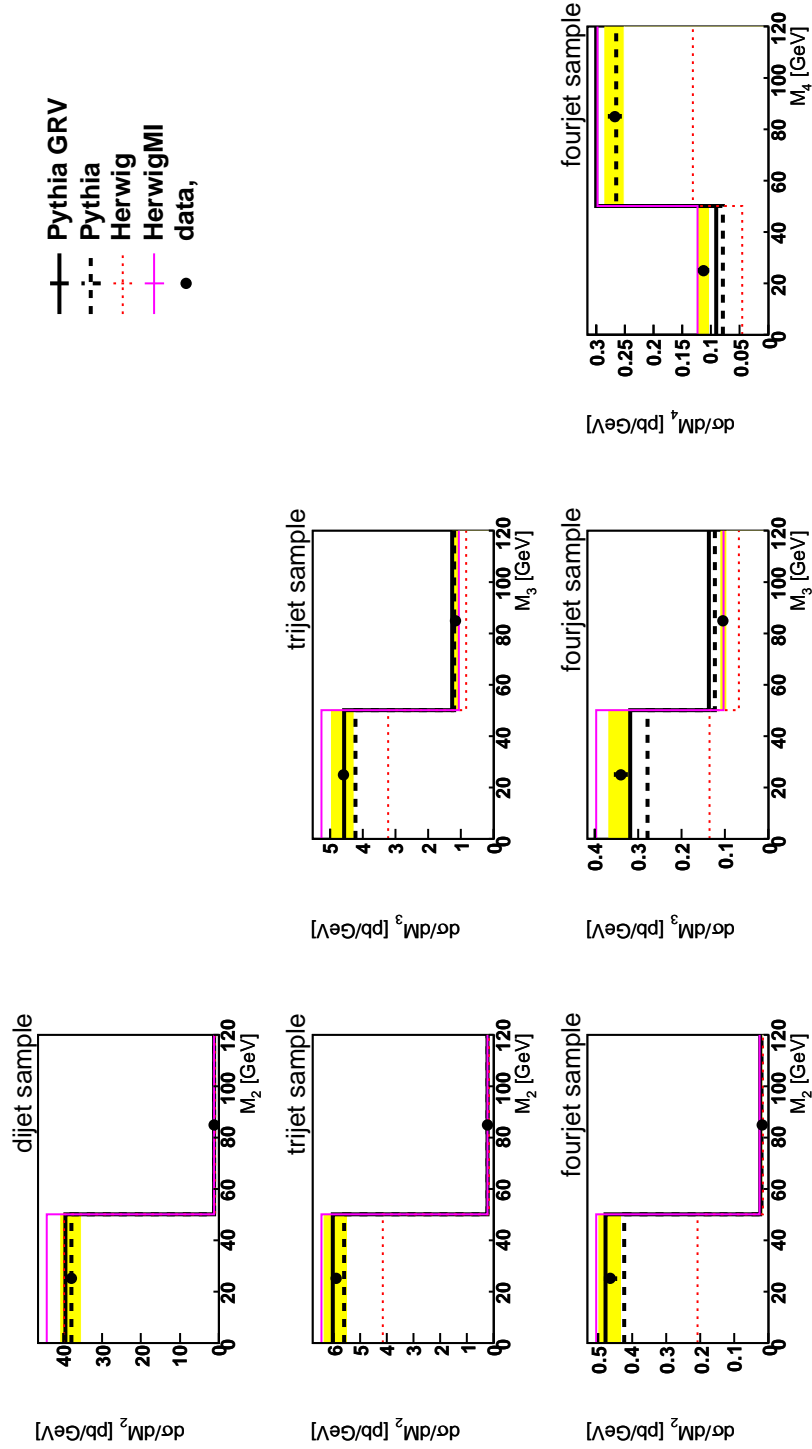
Figure 6.17: *Differential cross sections as a function of the invariant mass for the selected jets in the dijet, trijet and fourjet samples. Data are compared to* HERWIG *and* PYTHIA*. Models with multiple interactions are represented by solid lines while dashed lines correspond to models without multiple interactions.*
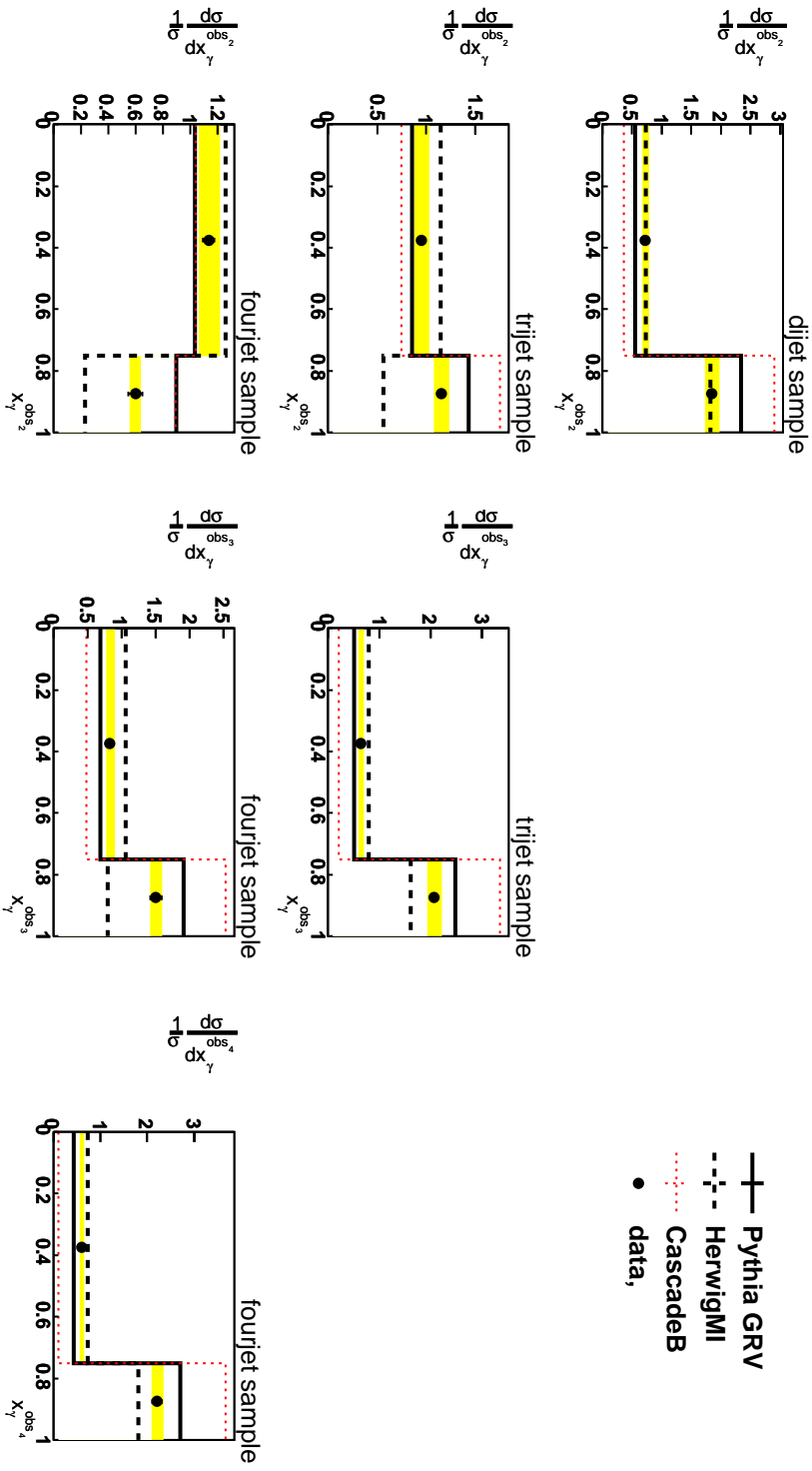
Figure 6.18: *Differential cross sections normalized to the visible cross as a function of the x_γ for the selected jets in the dijet, trijet and fourjet samples. Corrected data are compared to HERWIG, PYTHIA and CASCADE predictions.*

Figure 6.19: *Differential cross sections, normalized to the visible cross section, as a function of the azimuthal angle between the two hardest jets for the selected events in the dijet, trijet and fourjet scenario. Corrected data are compared to* HERWIG, PYTHIA *and* CASCADE *predictions.*

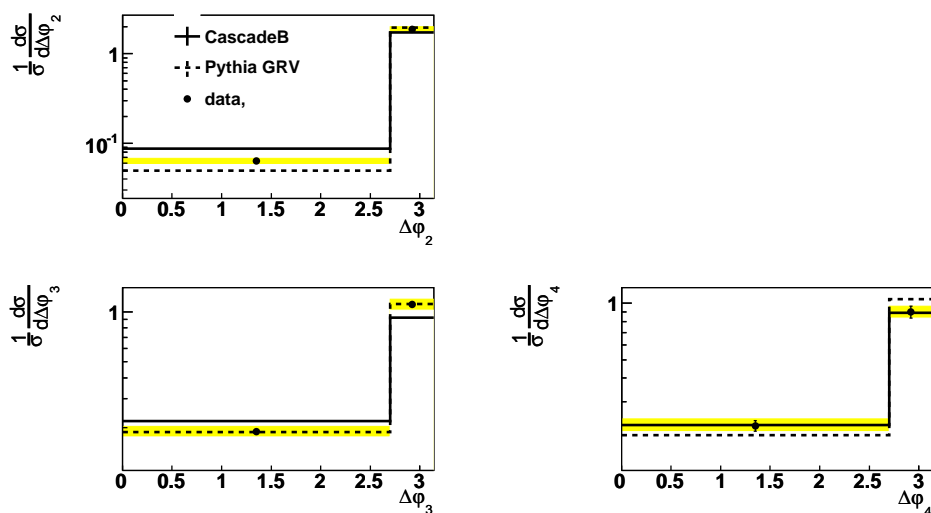The differential cross section as a function of the azimuthal angle between the two hardest jets for all data samples and the ratio of the cross sections to the data are shown in Figure 6.19.

Chapter 7

Conclusions

At **H1**, trijet and fourjet cross sections have been measured in DIS[52]. However, this is the first measurement of the multijet cross sections in photoproduction. In the analysis, jet cross sections are measured down to $E_{T,jet} > 9$ GeV. This is a big improvement in comparison to the last **H1** publication[51] where jets were measured down to 25 GeV. A cross check confirming the results from the analysis is presented in Section 6.2.

The energy scale uncertainty is identified as the main source of systematic error in the cross sections determination. The statistical errors of the measurement are smaller than the systematic uncertainty except for the fourjet scenario where the statistical and systematic errors become comparable. Therefore, more statistics are expected to improve the precision of the measurement in the fourjet scenario.

As visible in upper plots in Figure 6.12, the **jet multiplicity** is not described by the Monte Carlo models. PYTHIA underestimates the cross section for multijet events. The discrepancy increases as a function of the number of jets. Similarly, the discrepancy in the CASCADE prediction increases with jet multiplicity by over-estimating the cross sections. The predictions from HERWIG are similar to the predictions from PYTHIA. This disagreement between the data and theory is expected when taking into account that the used Monte Carlo generators calculate the cross section from the leading order matrix elements only. The multijet cross sections is expected to have higher order corrections which increase with the jet multiplicity. This corrections are taken into account in the lower plots in Figure 6.12. The DGLAP based models predict an increasing contribution from multiple interactions as a function of the jet multiplicity. In HERWIG, this contribution is much larger than in PYTHIA. The ratio of dijet to trijet and trijet to fourjet production corresponds to the expected $1/\alpha_s$ ratio taking in account the jet asymmetry.

The differential cross sections as a function of the **transverse energy** in Figure 6.13 and Figure 6.14 are well described by all models over more than three orders of magnitude. The cross sections are observed to fall off approximately exponentially

with the increasing of E_T. The multiple interactions are necessary for DGLAP based Monte Carlo generators in order to give correct predictions in the low $E_{T,jet}$ region. This effect is large in HERWIG but also significant in the PYTHIA predictions. CASCADE describes reasonably the low E_T region but tends to produce too little hard radiation compared to data.

The **pseudorapidity** of jets in Figure 6.15 is not described by the Monte Carlo models even for the dijet scenario. This shows that the jet production in the analysis phase space is not well understood. The pseudorapidity of the third and fourth jets is described better than η of the two hardest jets.

The **invariant mass** of the jet system is calculated according to Equation 5.6. The measured data is compared to PYTHIA with two different photon PDFs in Figure 6.16. GRV-G LO describes the measured data better than SAS-G 1D. For this reason PYTHIA with GRV-G LO photon PDF's is used for the other comparisons. As shown in Figure 6.17, DGLAP models predict that the multiple interactions are important at low values of the invariant mass. In this region, PYTHIA describes the data reasonably good when multiple interactions are included. Same conclusions apply to HERWIG for which the effect of including multiple interactions is even larger.

The cross sections, differential in $\mathbf{x}_\gamma$, as defined in Equation 1.22, are shown in Figure 6.18. All models fail to describe the shape of the data except HERWIG in the dijet scenario. PYTHIA and CASCADE give similar predictions. This may suggest that this observable is sensitive to the hadronization model.

In Figure 6.19, the bin averaged cross sections as a function of the **azimuthal angle**, $\Delta\varphi$, between the two leading jets are shown. Results are compared with predictions from PYTHIA and CASCADE. PYTHIA describes $\Delta\varphi$ distribution for the dijet and trijet scenario but fails for the fourjet where CASCADE describes measured data correctly.

In general, the description of the measured cross sections improves when multiple interactions are included in the DGLAP based models. This effect of multiple interactions is larger in HERWIG predictions in comparison to PYTHIA. Both generators predict that the effect of multiple interactions becomes important for low transverse energies of jets. The comparison of the measured cross sections to the models indicate that multiple interactions become significant for low values of the jet system invariant mass and high jet multiplicity. It is worth to notify that CASCADE also predicts higher cross sections and more jets without explicitly generating multiple interactions.

A direct comparison with results from similar measurements, done by the ZEUS collaboration, e.g.[53], are not possible because their phase space differs very much from the phase space of this analysis. However, the conclusions from the current measurement are in agreement with results published by ZEUS.

Appendix A

Variables

The transverse energy E_T and the rapidity y of a particle are defined by

$$E_T = E \sin \theta, \tag{A.1}$$

$$y = \frac{1}{2} \ln \frac{E + p_z}{E - p_z}, \tag{A.2}$$

where E is the energy, θ is the polar angle and p_z is the z-component of the momentum. The pseudorapidity η is defined when the mass of the particle could be neglected:

$$\eta = \lim_{m \to 0} y = -\ln \tan \frac{\theta}{2}, \tag{A.3}$$

Instead of E and θ, E_T and η are often preferred as being invariant over longitudinal Lorentz transformations.

Bibliography

[1] F. Halzen and A. D. Martin, "QUARKS AND LEPTONS: AN INTRODUCTORY COURSE IN MODERN PARTICLE PHYSICS,". New York, Usa: Wiley (1984) 396p.

[2] J. D. Bjorken and E. A. Paschos, "Inelastic Electron Proton and gamma Proton Scattering, and the Structure of the Nucleon," *Phys. Rev.* **185** (1969) 1975–1982.

[3] **H1 and ZEUS** Collaboration, K. Krastev, "Hadronic final state, jet production and alpha(s) measurements at HERA," *Nucl. Phys. Proc. Suppl.* **174** (2007) 71–74.

[4] G. Altarelli and G. Parisi, "Asymptotic Freedom in Parton Language," *Nucl. Phys.* **B126** (1977) 298.

[5] V. N. Gribov and L. N. Lipatov, "Deep inelastic e p scattering in perturbation theory," *Sov. J. Nucl. Phys.* **15** (1972) 438–450.

[6] Y. L. Dokshitzer, "Calculation of the Structure Functions for Deep Inelastic Scattering and e+ e- Annihilation by Perturbation Theory in Quantum Chromodynamics. (In Russian)," *Sov. Phys. JETP* **46** (1977) 641–653.

[7] V. S. Fadin, E. A. Kuraev, and L. N. Lipatov, "On the Pomeranchuk Singularity in Asymptotically Free Theories," *Phys. Lett.* **B60** (1975) 50–52.

[8] M. Ciafaloni, "Coherence Effects in Initial Jets at Small q**2 / s," *Nucl. Phys.* **B296** (1988) 49.

[9] S. Catani, F. Fiorani, and G. Marchesini, "QCD Coherence in Initial State Radiation," *Phys. Lett.* **B234** (1990) 339.

[10] S. Catani, F. Fiorani, and G. Marchesini, "Small x Behavior of Initial State Radiation in Perturbative QCD," *Nucl. Phys.* **B336** (1990) 18.

[11] C. F. von Weizsacker, "Radiation emitted in collisions of very fast electrons,"
Z. Phys. **88** (1934) 612–625.

[12] W. Heisenberg and H. Euler, "Consequences of Dirac's theory of positrons," *Z. Phys.* **98** (1936) 714–732, `physics/0605038`.

[13] J. J. Sakurai and D. Schildknecht, "Generalized vector dominance and inelastic electron - proton scattering," *Phys. Lett.* **B40** (1972) 121–126.

[14] **L3** Collaboration, P. Achard *et al.*, "Measurement of the photon structure function F2(gamma) with the L3 detector at LEP," *Phys. Lett.* **B622** (2005) 249–264, `hep-ex/0507042`.

[15] S. Catani, Y. L. Dokshitzer, M. H. Seymour, and B. R. Webber, "Longitudinally invariant K(t) clustering algorithms for hadron hadron collisions," *Nucl. Phys.* **B406** (1993) 187–224.

[16] J. M. Butterworth, J. P. Couchman, B. E. Cox, and B. M. Waugh, "KtJet: A C++ implementation of the K(T) clustering algorithm," *Comput. Phys. Commun.* **153** (2003) 85–96, `hep-ph/0210022`.

[17] T. Sjostrand and P. Z. Skands, "Multiple interactions and the structure of beam remnants," *JHEP* **03** (2004) 053, `hep-ph/0402078`.

[18] J. M. Butterworth, J. R. Forshaw, T. Sjostrand, and J. K. Storrow, "Multiple Hard Parton Interactions at HERA," *J. Phys.* **G22** (1996) 883–892, `hep-ph/9601322`.

[19] F. J. Willeke, "Hera performance and prospects,". Prepared for 12th International Workshop on Deep Inelastic Scattering (DIS 2004), Strbske Pleso, Slovakia, 14-18 Apr 2004.

[20] U. Schneekloth, "The hera luminosity upgrade,". DESY-HERA-98-05.

[21] **H1** Collaboration, I. Abt *et al.*, "The h1 detector at hera," *Nucl. Instrum. Meth.* **A386** (1997) 310–347.

[22] **H1** Collaboration, I. Abt *et al.*, "The tracking, calorimeter and muon detectors of the h1 experiment at hera," *Nucl. Instrum. Meth.* **A386** (1997) 348–396.

[23] **H1 Calorimeter Group** Collaboration, B. Andrieu *et al.*, "The h1 liquid argon calorimeter system," *Nucl. Instrum. Meth.* **A336** (1993) 460–498.

[24] **H1** Collaboration, B. List, "The silicon tracker of the H1 detector," *Nucl. Instrum. Meth.* **A566** (2006) 110–113.

[25] R. A. Eichler, "Triggering with short bunch distances: The h1 trigger at hera as an example,". Invited talk given at 5th Int. Conf. on Instrumentation for Colliding Beam Physics, Novosibirsk, USSR, Mar 15-21, 1990.

[26] F. Sefkow, E. Elsen, H. Krehbiel, U. Straumann, and J. Coughlan, "Experience with the first level trigger of h1," *IEEE Trans. Nucl. Sci.* **42** (1995) 900–904.

[27] T. Nicholls *et al.*, "Concept, design and performance of the second level trigger of the h1 detector," *IEEE Trans. Nucl. Sci.* **45** (1998) 810–816.

[28] J. K. Köhne *et al.*, "Realization of a second level neural network trigger for the h1 experiment at hera," *Nucl. Instrum. Meth.* **A389** (1997) 128–133.

[29] P. Uelkes, "A Topological trigger for the H1 detector. (In German),". Aachen Tech. Hochsch. - PITHA-93-21 (93/06,rec.Aug.) 101 p.

[30] **H1** Collaboration, A. Schöning, "The fast track trigger at the h1 experiment design concepts and algorithms," *Nucl. Instrum. Meth.* **A566** (2006) 130–132.

[31] S. Schmitt, "Trigger status,". Talk given at the Trigger Meeting.

[32] A. Dubak, "Jet trigger in the H1 experiment at HERA," *AIP Conf. Proc.* **899** (2007) 573.

[33] H. C. Schultz-Coulon, E. Elsen, T. Nicholls, J. Coughlan, and H. Rick, "A general scheme for optimization of trigger rates in an experiment with limited bandwidth," *IEEE Trans. Nucl. Sci.* **46** (1999) 915–919.

[34] T. Sjostrand, "Monte carlo generators," hep-ph/0611247.

[35] D. Amati and G. Veneziano, "Preconfinement as a Property of Perturbative QCD," *Phys. Lett.* **B83** (1979) 87.

[36] B. Andersson, G. Gustafson, G. Ingelman, and T. Sjostrand, "Parton Fragmentation and String Dynamics," *Phys. Rept.* **97** (1983) 31.

[37] T. Sjostrand *et al.*, "High-energy-physics event generation with pythia 6.1," *Comput. Phys. Commun.* **135** (2001) 238–259, hep-ph/0010017.

[38] G. Corcella *et al.*, "Herwig 6: An event generator for hadron emission reactions with interfering gluons (including supersymmetric processes)," *JHEP* **01** (2001) 010, hep-ph/0011363.

[39] J. M. Butterworth and J. R. Forshaw, "Photoproduction of multi - jet events at HERA: A Monte Carlo simulation," *J. Phys.* **G19** (1993) 1657–1663.

[40] J. M. Butterworth, J. R. Forshaw, and M. H. Seymour, "Multiparton interactions in photoproduction at HERA," *Z. Phys.* **C72** (1996) 637–646, hep-ph/9601371.

[41] H. Jung, "The CCFM Monte Carlo generator CASCADE," *Comput. Phys. Commun.* **143** (2002) 100–111, hep-ph/0109102.

[42] S. Kretzer, H. L. Lai, F. I. Olness, and W. K. Tung, "CTEQ6 parton distributions with heavy quark mass effects," *Phys. Rev.* **D69** (2004) 114005, `hep-ph/0307022`.

[43] G. A. Schuler and T. Sjostrand, "Parton Distributions of the Virtual Photon," *Phys. Lett.* **B376** (1996) 193–200, `hep-ph/9601282`.

[44] J. Pumplin *et al.*, "New generation of parton distributions with uncertainties from global QCD analysis," *JHEP* **07** (2002) 012, `hep-ph/0201195`.

[45] G. A. Schuler and T. Sjostrand, "Parton Distributions of the Virtual Photon," *Phys. Lett.* **B376** (1996) 193–200, `hep-ph/9601282`.

[46] M. Gluck, E. Reya, and A. Vogt, "Parton structure of the photon beyond the leading order," *Phys. Rev.* **D45** (1992) 3986–3994.

[47] H. background working group, "Technical Report on the Beam Induced Backgrounds in the H1 Detector," *H1 note H1-10/02-606* (2002).

[48] F. Jacquet and A. Blondel, "Proceedings of the Study of an ep facility for Europe," *DESY 79/48* (1979).

[49] M. Paterno, "Calculating efficiencies and their uncertainties,". FERMILAB-TM-2286-CD.

[50] G. Cowan, "Statistical data analysis,". Oxford, UK: Clarendon (1998) 197 p.

[51] **H1** Collaboration, A. Aktas *et al.*, "Photoproduction of dijets with high transverse momenta at HERA," *Phys. Lett.* **B639** (2006) 21–31, `hep-ex/0603014`.

[52] **H1** Collaboration, F. D. Aaron *et al.*, "Three- and Four-jet Production at Low x at HERA," *Eur. Phys. J.* **C54** (2008) 389–409, `0711.2606`.

[53] **ZEUS** Collaboration, S. Chekanov *et al.*, "Three- and four-jet final states in photoproduction at HERA," *Nucl. Phys.* **B792** (2008) 1–47, `0707.3749`.